Title

In Situ Nanoindentation in a Transmission Electron Microscope

Author

Minor, Andrew M

Publication Date

2002-12-01

LBNL-51869

ERNEST ORLANDO LAWRENCE
BERKELEY NATIONAL LABORATORY

In Situ Nanoindentation in a Transmission Electron Microscope

Andrew M. Minor

Materials Sciences Division

December 2002

Ph.D. Thesis

DISCLAIMER

LBNL-51869

In Situ Nanoindentation in a Transmission Electron Microscope

Andrew Murphy Minor
Ph.D. Thesis

Department of Materials Science and Engineering
University of California, Berkeley

and

Materials Sciences Division
Ernest Orlando Lawrence Berkeley National Laboratory
University of California
Berkeley, CA 94720

December 2002

This work was supported by the Director, Office of Science, Office of Basic Energy Sciences, Materials Sciences Division, of the U.S. Department of Energy under Contract No. DE-AC03-76SF00098.

In situ Nanoindentation in a Transmission Electron Microscope

by

Andrew Murphy Minor

B.A. (Yale University) 1997
M.S. (University of California, Berkeley) 1999

A dissertation submitted in partial satisfaction of the

requirements for the degree of

Doctor of Philosophy
in

Engineering - Materials Science and Engineering

in the

GRADUATE DIVISION

of the

UNIVERSITY OF CALIFORNIA, BERKELEY

Committee in charge:

Professor John W. Morris, Jr., Chair
Professor Daryl C. Chrzan
Professor Lisa A. Pruitt

Fall 2002

In situ Nanoindentation in a Transmission Electron Microscope

by

Andrew Murphy Minor

Abstract

In Situ Nanoindentation in a Transmission Electron Microscope

by

Andrew Murphy Minor

Doctor of Philosophy in Materials Science and Engineering

University of California, Berkeley

Professor John W. Morris, Jr., Chair

This dissertation presents the development of the novel mechanical testing technique of *in situ* nanoindentation in a transmission electron microscope (TEM). This technique makes it possible to simultaneously observe and quantify the mechanical behavior of nano-scale volumes of solids.

Chapter 2 details the unique specimen preparation techniques employed to meet the geometrical constraints of the *in situ* experiments. These techniques include bulk silicon micromachining and the use of a focused ion beam. In section 2.4 a method of voltage-controlled mechanical testing is derived theoretically and proven experimentally. This method enables the quantification of the mechanical behavior during *in situ* nanoindentation experiments.

Three classes of material systems were studied with this new technique: (1) bulk single crystal, (2) a soft thin film on a harder substrate and (3) a hard thin film on a softer substrate. Section 3.2 provides the first direct evidence of dislocation nucleation in single crystal silicon at room temperature. In contrast to the observation

of phase transformations during conventional indentation experiments, the unique geometry employed for the *in situ* experiments resulted in dislocation plasticity. In section 3.3 results from *in situ* nanoindentation of Al films on Si substrates are presented. These results include the correlation of the microstructural deformation behavior with load vs. displacement data. It is shown that a sharp change in the force-displacement response at the elastic-to-plastic transition signifies the nucleation of dislocations. Additionally, the softening of sub-micron grains with size is observed. Section 3.4 discussed the influence of the substrate on the indentation response of two thin film/substrate systems where the films were harder than the substrate. Amorphous diamond on Si and epitaxial TiN on MgO (001) systems were studied. It was found that the deformation in the harder films was controlled by the deformation in the softer substrates.

The direct observations of each material system during indentation provided unique insight into the interpretation of *ex situ* nanoindentation tests, as well as to the intrinsic mechanical behavior of nano-scale volumes of solids. These results represent the first real time observations of the discrete microstructural events that occur during nanoindentation

This dissertation is dedicated to my family-

Mom, Dad, Pat, Greg, Rosie and Butch

Table of Contents

List of Figures

List of Tables

Acknowledgements

Over the course of my graduate career at Berkeley I have been blessed with the guidance of three particularly important mentors. First, I would like to thank my research advisor Professor J.W. Morris, Jr., whose broad wisdom includes, but does not begin or end with material science. Over the last five years Professor Morris was always a source of unwaveringly encouragement and support. Without him I would undoubtedly be much less of a scientist and person than I am today. Secondly, Dr. Eric Stach has served as a friend, colleague and mentor to me since the beginning of my work at the National Center for Electron Microscopy. Over the last three years I have counted on Eric for advice and support, and he has never failed to provide me with either. At the beginning of my graduate career, Dr. Chris Krenn was an older graduate student in the Morris Group who took me under his wing. Chris always had time to answer the silly questions of a neophyte graduate student, and he served as an important example of how to succeed in life and in school.

In addition to Professor Morris, I am grateful to Professor Daryl Chrzan and Professor Lisa Pruitt for serving on my thesis committee. Professor Chrzan in particular has been an important source of encouragement, support, friendship and advice during my graduate career.

Dr. Erica Lilleodden was a friend first and a colleague second. Her spirited passion for scientific debate has led to a collaboration that is part friendship and part work. Over the last two years she has been a generous source of support and encouragement. My officemate, Dr. Ho Geon Song, has shared the ups and downs of the last five years with me as a unwavering friend and colleague. I am grateful for his friendship. I am also very grateful for the support and friendship from the many other members of the Morris Group over the years: Dr. David Mitlin, Dr. Zhen Guo, Dr.

Seung-Hyuk Kang, Dr. Koji Sato, Carlos Gonzalez, David Clatterbuck, Tae-Kyu Lee, Miao Jin, Brian Dracup and Rosemary Cole.

My research would not have been possible without the technical support at the Lawrence Berkeley National Laboratory. In particular, I am indebted to the staff members at the National Center for Electron Microscopy, including Tony Freeman, Doug Owen, and John Turner, and Jane Cavalina.

Most importantly, I am indebted to my friends and family who have supported and encouraged me over the years.

Lastly, I would like to thank Dr. Gary Povirk, who taught the first materials science course I ever took. His inspiration and guidance led me to graduate school, and his early confidence led me to believe I could finish.

This research was funded by the Director, Office of Science, Office of Basic Energy Science, Materials Science Division of the U.S. Department of Energy, under contract No. DE-AC03-76SF00098.

1 Introduction

1.1 Overview

This dissertation describes the first comprehensive studies of the deformation of materials conducted with the novel mechanical testing technique of *in situ* nanoindentation in a transmission electron microscope (TEM). This technique makes it possible to simultaneously observe and quantify the mechanical behavior of nano-scale volumes of solids. Conventional nanoindentation techniques have been developed over the past 20 years as a method to probe the mechanical properties of materials in the sub-micron size range[1,2], which is a typical dimension of the thin films used in integrated circuits and micro-electro-mechanical systems (MEMS). However, real-time observations of the mechanism of deformation in a material during nanoindentation have only become possible with the development of the *in situ* technique described herein.

In typical nanoindentation experiments, the sample surface is indented with a sharp diamond pyramid, which has a tip that can be characterized by a radius of curvature on the order of 100nm. Both elastic and plastic deformation results in the sample. The displacements imposed during nanoindentation are on the order of nanometers, and high-resolution load and displacement measurements are simultaneously recorded. Thus, it is possible to study atomistic-scale deformation processes, such as dislocation nucleation events[3,4] and pressure-induced phase transformations[5].

A multitude of behaviors has been observed with conventional indentation techniques[6], although direct observations of the associated mechanisms of deformation have been until now importantly lacking. For this dissertation, three classes of material systems have been studied: (1) bulk single crystal, (2) a soft thin film on a harder

substrate and (3) a hard thin film on a softer substrate. For each of these three classes of material systems, novel sample preparation techniques were employed so that the *in situ* nanoindentation experiments could be conducted inside a transmission electron microscope. The direct observations of each material system during indentation provided unique insight into the interpretation of *ex situ* nanoindentation tests, as well as to the intrinsic mechanical behavior of nano-scale volumes of solids.

The purpose of this dissertation is thus two-fold: (1) to detail a new experimental method for performing nanoindentation inside an electron microscope, and (2) to report the initial use of this technique to study the nanomechanical properties of three different material systems.

1.2 Background

Indentation testing has been used for many years as a convenient method to characterize the hardness of a material. Hardness is classically defined as a material's resistance to plastic deformation[7]. A microhardness indentation is typically used as a method to test the mechanical properties of a material because the deformed region of a microhardness indentation is extremely small (contact area~1mm^2) as compared to, for example, an ingot of metal. Thus, in industrial terms, a micro-hardness indentation can be considered essentially a non-destructive means of testing a finished product.

The advent of the microelectronics industry necessitated the development of characterization tools more appropriate for the size and scale of the thin films and small structures associated with microelectronic devices. By the 1980's significant advances in nano-scale science and instrumentation led to the first "instrumented" indentation techniques at sub-micron length scales. Pethica, Hutchings and Oliver[1] first demonstrated the technique of providing continuous measurement of load and displacement during indentation with resolutions in the sub-microNewton and the sub-nanometer regimes. Since then, the technique of nano-scale harness testing has become broadly referred to as nanoindentation.

When considering how to probe the mechanical behavior of thin films and small (sub-millimeter) structures, there exist several alternative methods to nanoindentation. For example, wafer curvature [e.g. 8,9], bulge testing [e.g.1011], micro-beam bending [e.g.12], micro-tensile testing [e.g.13], and MEMS-actuated tests [e.g.14] all measure the mechanical properties of thin films and small structure. However, there is an important distinction between nanoindentation and these other micro and nanoscale mechanical testing methods. Nanoindentation is the only method that probes a small enough volume of material to

observe discrete and localized deformation phenomena in a material. All other mechanical testing methods probe relatively large volumes and measure properties of materials in a continuum manner, where the mechanical properties are typically dominated by defects. During a nanoindentation experiment, however, the peak stresses occurs below the surface, in volumes that are small enough to be closely assumed defect-free, perfect crystal.[15] Clearly, indentation into defect-free volumes cannot be accommodated by conventional plastic flow - nucleation of defects must occur first.

For example, Figure 1.2.1 shows two examples of the most commonly observed discrete phenomena from a nanoindentation measurement. Figure 1.2.1a is a conventional nanoindentation curve from a 1 micron-thick Au film on a silicon substrate. During the loading of the film, the curve shows discrete displacement bursts, which are typically observed during the nanoindentation of metals and are commonly referred to as either staircase-yielding[16] or "pop-ins"[4,17,18]. Figure 1.2.1b is a conventional nanoindentation curve of single crystal <100> silicon, which shows a different kind of discrete behavior. While the loading of the sample is smooth, upon unloading a displacement burst is seen in the unloading direction. This discrete behavior is typically associated with the nanoindentation of semiconductors and is commonly referred to as a "pop-out"[21].

The pop-in phenomenon observed during the loading of a material at shallow depths is one of the most debated issues in the nanoindentation community. Although it seems reasonable that pop-in behavior is due to the nucleation of dislocations, only post-mortem TEM analysis has been used to correlate dislocations and load vs. displacement data. Page and coworkers[49] used TEM to investigate the post-indent microstructure around indentations where pop-ins had or had not occurred during the nanoindentation of sapphire. Post-indent TEM samples showed dislocation structures around indentations associated with discrete displacement bursts in the loading behavior, and no dislocations

surrounding indents that exhibited superimposed loading and unloading (i.e. no pop-ins). Gerberich and coworkers[17] used Atomic Force Microscopy (AFM) to show that no observable surface deformation results from indentations of Fe-3wt%Si single crystals when there is no pop-in, and considerable surface deformation from indentations that displayed pop-in. Other studies have shown that the stress at which initial displacement bursts occur are on the same order of the critical stress needed to nucleate dislocations in previously defect-free material[19,3]. These measurements strongly support the idea that pop-ins are related to the nucleation of dislocations.

However, in many studies of pop-in behavior it is argued whether or not displacement discontinuities are truly related to nucleation events. Oxide fracture or activation of pre-existing dislocations are other proposed rationales for such behavior.[20] Even though the peak stresses applied to a material during indentation occur below the surface[15], the in-plane stresses imposed at the surface are not zero. It is argued that the presence of a native oxide layer can provide a defect source for the initiation of plasticity[20], or can act as a barrier to dislocations generated within the bulk. Typically, however, the presence of oxide layers is often ignored in analyses of load-displacement behavior measured during indentation.

The pop-out phenomenon observed during nanoindentation in semiconductors is thought to be associated with phase transformations. Numerous nanoindentation studies of semiconductors such as Si[5,42,21], Ge[22] and GaAs[22,23] have shown pop-out behavior followed by indirect evidence of a phase transformation at the time of the pop-out phenomenon. Although the evidence is both indirect and often unclear, the most common explanation for pop-outs is that the material undergoes a high pressure phase transformation upon loading (thus densifying), followed by a transformation back to a low pressure phase upon unloading. The transformation to a low-pressure phase results in

a large volume increase and therefore causes a sudden displacement burst in the direction of unloading (a pop-out). For example, it is believed that silicon transforms to high pressure metallic phases (e.g. β-Sn) during loading, as is inferred by *in situ* Raman spectroscopy[5] and resistivity measurements[42]. Upon unloading, the high pressure metallic phases are thought to transform to either a low pressure metallic phase or undergo amorphization. Post mortem TEM analysis has provided evidence of both bcc-R8 and amorphous silicon phases[42], where the resultant phase is controlled by the unloading rate as well as the depth of indentation.

Conventional nanoindentation experiments have not been able to completely describe the discrete microstructural phenomena associated with pop-ins and pop-outs, and to probe the discrete mechanisms of nano-scale plasticity that only nanoindentation can achieve. In a typical nanoindentation experiment, the contact areas are typically on the order of ~100 nm^2, when combined with applied forces on the order of milliNewtons results in stresses on the order of GigaPascals [3,4,24]. These stresses inside the small volume of perfect crystal during a nanoindentation experiment approach the ideal strength of a material, a phenomenon not seen in any other mechanical test. Thus, nanoindentation makes it possible to directly probe the mechanical behavior of a material at its point of elastic instability. This behavior includes dislocation nucleation[3,5] and pressure induced phase transformations[5].

The ideal strength of a material is defined as the stress required to plastically deform an infinite, perfect crystal.[25] In reality, however, crystals are neither infinite nor perfect. As a result, most materials deform at stress levels well below their ideal strengths, (e.g. for most metals $\tau_{yield} \approx 0.01\tau_{ideal}$). This is because a typical solid will relieve an imposed stress through mechanisms of deformation that are activated at stresses much lower than its ideal strength. As stated by Morris, et al.[26], "If a solid is

crystalline, the transformation to a stress-free state is accomplished by one of three basic mechanisms: (1) The solid deforms into a sheared replica of itself by moving dislocations, twinning, or diffusion. (2) The solid breaks into stress-free fragments. (3) The solid changes its shape by changing its crystal structure, a process that is sometimes called 'transformation-induced plasticity'. . . . The strength of the solid is the stress that triggers the easiest of these transformations."

While conventional nanoindentation tests are able to quantitatively measure the mechanical behavior of materials, direct observations of the deformation mechanisms during nanoindentation have been until now importantly lacking. Typically, the mode of deformation during a nanoindentation test is only studied *ex situ,* and *ex post facto.* To date, *in situ* observations of a material's deformation behavior has only come through indirect techniques such as *in situ* Raman spectroscopy[5] and *in situ* electrical resistivity measurements[42]. However, to truly observe the microstructural response of a material during indentation the deformation must be imaged at a resolution on the same order as the size of the defects created. Only a transmission electron microscope can provide the sub-nanometer resolution and the ability to image sub-surface phenomena such as the creation of dislocations and nucleation of phase transformations. The phenomenological interpretation of nanoindentation tests, and indeed the mechanical behavior of solids at their elastic limit, is a fundamental area of materials science which has lacked direct experimental observations. This thesis describes a novel method for exploring this nano-scaled regime of mechanical behavior and therefore the ideal strength behavior of solids.

2 Experimental Procedure

2.1 Overview

The *in situ* nanoindentation experiments described in this dissertation were made possible through the development of a novel sample stage for a transmission electron microscope (TEM). Designed initially by Mark Wall and Uli Dahmen at the National Center for Electron Microscopy in Berkeley, CA in 1997[27], the initial experiments were performed by Wall and Dahmen on Si with a stage designed for use in a Kratos High Voltage Microscope. The experiments described in this thesis were performed on subsequent stages designed for a Jeol 200kV TEM and a Jeol 300kV TEM. A picture of the indentation stage used in the Jeol 200kV TEM is shown in Figure 2.1.1. The stage consists of a diamond indenter attached to a metal rod which is actuated by two mechanisms. For coarse positioning, the indenter can be moved in 3 dimensions by turning screws attached to a pivot at the end of the rod. For fine positioning, including the actual indentation, the indenter is moved in 3 dimensions with a piezoelectric ceramic crystal, which expands in response to an applied voltage.

All of the experiments were run under voltage-control, where the actual loading mechanism was the expansion of the piezoelectric crystal under an applied voltage. Through the use of an graphics computer[28], the voltage applied to the piezoelectric element could be recorded directly onto the video in real time. Thus, the video recording for each experiment contained all of the raw experimental data- the voltage applied to the piezoelectric crystal, the displacement of the indenter, and the images of the resulting deformation in the sample in real time. A schematic of the experimental setup is shown in Figure 2.1.2.

In order to be electrically conductive in the TEM, the diamond at the end of the rod must be doped with boron and attached with electrically conductive epoxy. The first diamond used in this study was purchased from the supplier pre-doped with boron to a concentration high enough to be electrically conducting. This diamond was a 3-sided pyramid indenter with a radius of curvature of approximately 75nm*, and is shown in Figure 2.1.3. Diamonds used subsequently were purchased undoped, and then diffused with boron in the UC Berkeley Microfabrication laboratory. A boron concentration of approximately 10^{20} ppm was achieved by annealing these diamonds in close proximity to boron-hydride coated wafers at 1000°C for 1 hour. The boron concentration was estimated based on thermal diffusion studies of single crystal diamond[29],[30]. These diamonds had a 3-sided Berkovich geometry, as is used in conventional nanoindentation experiments[2], with a radius of curvature of approximately 75-100 nm, and are pictured in cross-section in Figure 2.1.4. The diamond is mounted on the end of an Al rod that is in turn connected directly to the piezo-ceramic actuator, which both controls its position in 3 dimensions and forces it into the edge of the sample.

The *in situ* nanoindentation experiments posed three significant constraints on the required geometry of the samples. The first constraint, common to all TEM investigations, is that the region of the sample to be imaged must be thin enough to be electron transparent. The critical thickness is typically ~300 nm, but this is dependent on the material and the accelerating voltage of the microscope. The second constraint, which is unique to the *in situ* nanoindentation experiments, is that the electron transparent part of the sample must be accessible to the diamond indenter in a direction normal to the

---

* Radius of curvature measurements typically varied with each experiment and cross-sectional image in the TEM (variation of approximately +/- 33%)

electron beam. The third constraint is that the sample must be mechanically stable such that indentation, and not bending, results from the indenter pressing upon the thin region of the sample. Figure 2.1.5 is a schematic showing the additional geometric constraints of accessibility and mechanical stability. Figure 2.1.6 shows the actual sample holder with a sample loaded across from the diamond.

In order to fabricate samples that were electron transparent, accessible to the diamond indenter and mechanically stable, it was necessary to design a unique sample geometry for the *in situ* nanoindentation experiments. Two different methods were used to meet these sample design constraints, and each will be described in detail in the following two sections. Following these two sections, the final experimental section describes a procedure developed to extract quantitative data from a voltage-controlled mechanical test.

2.2 Wedge substrate design

In order to meet the sample criteria defined earlier for the *in situ* nanoindentation samples, a lithographically-prepared substrate was designed and fabricated in the UC Berkeley Microfabrication Laboratory. Using proven bulk micromachining and thin film deposition techniques, the silicon substrates could be produced in large volumes (~ 800 per wafer) and of repeatable quality. The final substrate design resulted in an electron-transparent area approximately 1.5mm in length which was of a robust geometry for indentation. Theoretically, the microfabricated structures could then serve as a substrate for any material that can be deposited onto single crystal silicon in a thin film form.

The microfabrication process for the Si wedge substrates can be divided into seven essential steps, which will be summarized here. Figure 2.2.1 is a schematic diagram showing these seven steps.

The first step consists of growing a ~1 micron thick oxide layer onto a <100> Si wafer. The oxide layer will serve as the masking layer for the wet etch that defines the structure. After growing an oxide layer, the wafer is coated with a thin layer of negative photoresist and the photoresist is "soft baked". Then the mask with the wedge substrate design is aligned over the wafer and the photoresist is exposed to ultraviolet light, everywhere except for the lines defined by the shadow of the mask. After being exposed to the ultraviolet light, the photoresist is developed leaving behind a pattern of the photoresist identical to the mask pattern. The next step is to immerse the wafer in hydrofluoric acid (HF) so that the SiO_2 dissolves off everywhere except for under the photoresist lines. At this point you have a masking layer of SiO_2 over the Si substrate, with a minimum dimension of 3 microns over where the final ridge will be located.

The next step is a timed wet etch of the Si, and constitutes the most critical step in the microfabrication process. The wafer is immersed in a heated bath of potassium hydroxide (KOH) for a precise amount of time. This is the step which creates the basic geometry of the bulk micromachined wedge structure. KOH has been shown to be an extremely anisotropic etchant for Si[31,32], such that the {100} and {110} planes are etched much faster than the {111} planes. This is a result of the fact that the {111} planes in the diamond-cubic structure are the closest-packed planes. Thus the {111} planes have the lowest surface energy, which serves to limit reactions on all {111} surfaces. Bulk micromachining with KOH therefore allows for structures to be made out of single-crystal silicon which have walls defined by {111} planes. For instance, if one was to etch a masked line that was in a <011> direction on a <100> oriented-wafer with KOH, the result would be a ridge structure where the sidewalls are the {111} planes oriented 54.7° from the original <100> surface (see Figure 2.2.2).

For the *in situ* nanoindentation substrates, the KOH anisotropic etch was used to create the exact structure as shown in cross section in Figure 2.2.2. Essentially, an oxide line 3 microns in width was patterned on a wafer and immersed in KOH at 80°C for about 20 minutes. The resulting ridge structure was approximately 30 microns tall and peaked with a plateau of approximately 1 micron in width. Figure 2.2.3 is an electron image of a ridge structure just after being taken from the KOH bath without the SiO_2 mask removed, where the underetching of the mask can be seen as the SiO_2 extends partly beyond the Si below.

In order to be electron transparent in a TEM, the width of the sample to be imaged must in general be much less than the 1 micron plateau at the top of the ridge following the KOH etch step. The maximum thickness of a sample that is still electron-transparent depends on the atomic number of the material, the microstructure, and the accelerating

voltage of the microscope. In the case of polycrystalline Al thin films to be imaged with a 200kV Jeol TEM, the maximum electron-transparent thickness is generally about 300 nm. Because the wet etch step cannot achieve a plateau width less than ~1 micron without risk of underetching the mask layer, the timed wet etch is not precise enough to use as a final sharpening step.

The final sharpening of the ridge from a plateau of ~ 1 micron down to ~ 150 nm was accomplished with a high-stress oxide growth. Essentially, if you grow an oxide on the ridge structure at a relatively low temperature (900°C) the compressive stress caused by the volume expansion of the Si -> SiO_2 causes the growth of the oxide to be suppressed near any corners.[33] This processing step (usually not a step but an unwanted artifact) is termed "birdsbeak" in Si processing. In the case of the ridge structure, growing a low temperature oxide intended to be 1 micron in thickness on a planar surface results in a much thinner oxide at the top of the ridge. If the oxide was grown at a higher temperature the compressive stresses retarding the oxide growth would be relieved and the ridge would blunt instead of sharpen[34]. Successive oxide growths and removal of the oxide in HF can lead to sharpening of the ridge to electron-transparency within one or two cycles. Scanning electron micrographs of the final structures are shown in figures 2.2.4a and 2.2.4b. As can be seen in figure 2.2.4a, the structures were designed in the shape of an "H", where the middle crossbar of the "H" is the sharp wedge used for indentation. The larger sidebars were useful for dicing the wafer and for the final positioning in the *in situ* indentation holder. Figure 2.2.4b shows the intersection of the middle crossbar and the thicker sidebar.

The final silicon wedge structure can then be used as a substrate upon which a thin film can be deposited for *in situ* nanoindentation. The plateau thickness can be tailored by successive oxide sharpening steps to provide the proper thickness for electron

transparency of whatever material is deposited on top. In the case of Al, a plateau 150 nm in width with a 250 nm Al film deposited on top proved to be electron transparent, while also thick enough to be indented. However, when indenting only the silicon wedge structures as described in chapter 3.2, the thickness of the plateau at the top of the wedge was varied from ~30 nm to ~150 nm. Figure 2.2.5a is a cross-section of the sharpest wedge that was fabricated, which has a plateau of ~30 nm. Figure 2.2.5b is an example of a wedge left with a thicker plateau of ~150 nm.

2.3 Focused Ion Beam (FIB) sample preparation

A second sample preparation method was employed in order to perform *in situ* nanoindentation experiments on materials which could not be easily deposited on the lithographically-prepared silicon wedge substrates. This second method relied on a FEI dual-beam Focused Ion Beam (FIB) at the National Center for Electron Microscopy in Berkeley, CA, which used a precisely-controlled 30kV Ga ion beam to mill away material from a sample of the desired material. The material system prepared with the FIB of interest to this thesis was epitaxial TiN/MgO <100>. Since it is not possible to grow TiN thin films epitaxially on the Si wedge substrates, the FIB sample preparation method proved to expand the types of material systems which could be investigated through *in situ* nanoindentation.

Figure 2.3.1 is a schematic of the general sample geometry that the FIB sample preparation method is designed to achieve. The basic method for FIB sample preparation is to mill out a two opposing trenches on a flat piece of material which leaves behind a thin window that is electron transparent (< ~ 250 nm in thickness). As is shown in Figure 2.3.1, the electrons then travel along the trench and through the window, which is accessible by the diamond indenter in the direction normal to the surface. In this manner the two sample criteria for *in situ* nanoindentation which were described in section 2.1 are met.

The most important aspect of the FIB sample preparation process is the protection of the sample from damage due to the 30kV Ga ion beam. Three techniques were employed during the preparation of the epitaxial TiN/MgO <100> which decreased the amount of damage inflicted by the Ga beam. The first technique was to take advantage of the electron imaging capabilities of the dual beam FIB to decrease the total amount of

time the sample was exposed to the Ga beam. The dual-beam FIB is equipped with a field emission scanning electron microscope (FESEM), which allows the user to image the sample with electrons, while blanking the sample from the Ga. The second technique employed to limit ion beam damage was to slowly decrease the ion beam cross section as the milling approached the area of the sample that would eventually be the final electron-transparent window. The FIB had the capability of decreasing the ion beam current from 20,000 pA to as little as 1 pA, which decreased milling rate but substantially limited the ion beam footprint. An ion beam current of 3000-20,000 pA was typically used for large area milling of the beginning of the trenches. As the milling approached the area of the final window the current was steadily decreased to approximately 10-30pA.

The third, and most effective technique for limited the damage to the sample caused by the ion beam during thinning was to deposit a protective material on the surface of the sample which could later be removed. In typical FIB sample preparation, a thin layer of Pt, Pd, or W is deposited in the FIB for this purpose, but is not removed afterwards. For the *in situ* nanoindentation experiments, the protective layer had to be removed after the sample was thinned, since the surface of the sample that the protective layer was attached to would eventually be the surface indented in the TEM. Thus, the material used as a protective coating was limited to materials which could be easily removed after thinning, where the removal method did not damage the underlying sample.

The protective layer used for the TiN/MgO <100> samples was an evaporated Al thin film approximately 500 nm thick. The Al film was deposited at room temperature and at relatively low vacuum. Since the Al film was to be used purely as a sacrificial layer to adsorb incident Ga ions during FIB sample preparation, a film of poor quality was advantageous for removal after FIB processing. Deposition in a low vacuum and at

room temperature presumably resulted in a film with high impurity content and poor adhesion. A FESEM image of the trilayer structure (Al/TiN/MgO) is shown in Figure 2.3.2, which was prepared by cross-sectioning in the FIB.

Following deposition of the protective Al layer, trenches were milled out to electon transparency, which was approximately 200 nm in thickness. A number of Al/TiN/MgO samples were prepared with the FIB, and one such sample is documented in the next several figures. Figure 2.3.3 shows a very low magnification image of the entire sample, taken normal to the surface of the sample (in a <100> direction). From this image the overall sample geometry can be seen, where 4 electron transparent windows remain in the center of the sample. Figure 2.3.4 is a closer look at the 4 windows, taken this time at an angle of 52° from the surface normal. Figure 3.4.5 is a higher magnification of one of the individual electron transparent windows, again taken 52° from the surface normal. Figure 2.3.6 is an even higher magnification FESEM image of one corner of a window. From this image, the trilayer structure can be discerned, where the outermost layer of the window is the Al protective film, followed by the layer of TiN and then the MgO substrate. Figure 2.3.7 shows a series of images of one such window taken with a TEM before removing the protective Al layer. As can be seen, the trilayer structure is still intact, implying that the top of the TiN was left undamaged by the Ga beam. The same cannot be said, however, for the sides of the window, since the Ga beam necessarily had to come in contact with the sides at the end of the milling process.

After the electron-transparent window is milled out with the Ga beam, the Al protective layer must be removed. The most effective way to do so without damaging the underlying TiN/MgO sample was to dissolve the Al in dilute HCl for approximately 5 minutes. A final TiN/MgO window is shown in Figure 2.3.8 with the Al removed, where

the TiN layer (approximately 350 nm thick) can be seen on top of the MgO, with very little residual Al. As can be seen from this image, the windows are accessible to the diamond indenter normal to the surface that had been protected with Al. The *in situ* experiments performed on the TiN/MgO samples are discussed in chapter 3.4.

2.4 Calibration of the nanoindentation stage

In contrast to conventional indentation techniques, which provide high resolution load and displacement measurements, the load applied to the sample during *in situ* indentation is not measured directly. This is because indentation of the tip into the sample is controlled through the voltage applied to the piezo-ceramic element, which leads to a load which is dependent on both the voltage applied to the piezoceramic crystal and the resulting displacement during indentation. The voltage is the imposed (independent) variable, while the displacement is measured directly from the real time imaging of the indentation process.

The relationship between the voltage applied to the piezo-ceramic element, the displacement of the indenter and the force applied to the sample can be derived using a simple spring-dashpot model of the indentation system. This model is shown schematically in Figure 2.4.1. The stiffness of the piezo-ceramic crystal is represented by k_{PZ}, the stiffness of the indenter is described by $k_{indenter}$, and the stiffness of the gripping system, which is dominated by a Teflon ring, is given by k_{teflon}. The piezoelectric coefficient is described by d_{PZ}, and k_s is the contact stiffness. In order to calibrate our load frame for the constants described above, and hence establish a general relationship for the load-displacement behavior during indentation, a series of experiments were conducted on Si cantilevers where the bending stiffnesses were known. The derivation of the general relationship for quantitative voltage-controlled mechanical testing will now be described in below.

Let us first consider the displacement of the indenter assembly with an applied voltage, V, under the condition of no constraint (e.g. no sample contact), as shown in

Figure 2..4.1(a). This is equivalent to zero applied force, and the displacement is proportional to the applied voltage:

$$\Delta x_{PZ}^{0} = d_{PZ} V \qquad (1)$$

Next, when the indenter is in contact with the sample, shown in Figure 2.4.1(b), the indenter assembly no longer acts as a rigid solid that applies no force. Rather, a force, F, is applied to the sample, and the loading assembly can be described as a set of springs, as shown schematically in Figure 2.4.1(b). Since the rear of the indenter assembly, the piezoceramic crystal and the Teflon grip are in series, the effective spring constant associated with the load-frame is given by:

$$k_{LF} = \left\{ \frac{1}{k_{teflon}} + \frac{1}{k_{PZ}} + \frac{1}{k_{indenter}} \right\}^{-1} . \qquad (2)$$

In the loaded configuration, the total displacement of the indenter assembly is less than the unconstrained displacement, Δx_{PZ}^{0}, due to the resistance of the sample to the applied force, and is given by:

$$\Delta x_{PZ} = \Delta x_{PZ}^{0} - \Delta x_{LF}^{-}, \qquad (3)$$

where Δx_{LF}^{-} is the backward displacement of the load-frame, related to the force on the load-frame, F_{LF}, and the load-frame stiffness:

$$\Delta x_{LF}^{-} = \frac{F_{LF}}{k_{LF}} \qquad (4)$$

The total displacement of the indenter tip is necessarily equal to the displacement of the sample, Δx_s, which is in turn equal to the sum of the bending displacement, $\Delta x_{Si,bend}$, and indentation displacements of the sample, $\Delta x_{Si,ind}$:

$$\Delta x_{PZ} = \Delta x_{Si,bend} + \Delta x_{Si,ind} . \qquad (5)$$

Assuming that the stiffness of the contact is much greater than the stiffness of the cantilever, this simplifies to:

$$\Delta x_{PZ} \approx \Delta x_{Si,bend} = \Delta x_{Si} . \qquad (6)$$

This assumption is truly valid if the voltage-displacement data is taken from the unloading portion of the experiment, where there is no indentation at all. This was the method used in the calibration experiments described here. For a rectangular cross-section cantilever of constant width and thickness, the force applied to the cantilever, F_{Si}, is related to the bending displacement by:

$$F_{Si} = k_{Si} \Delta x_{Si} . \qquad (7)$$

The bending stiffness of the cantilever, k_{Si}, is defined as:

$$k_{Si} = E \frac{t^3 w}{4l^3}, \qquad (8)$$

where E is Young's modulus of Si in the bending direction, and t, w and l are the thickness, width and lever-arm length of the cantilever, respectively. Invoking the condition of equilibrium, the force applied to the cantilever must be equal to the force applied to the load-frame:

$$F_{LF} = F_{Si} = F. \qquad (9)$$

It is of interest to find a single relation between the force, displacement and voltage, in terms of the known constant k_{Si}, and the measured variables V and Δx_{Si}. By combining equations (3) and (6), we find:

$$\Delta x_{Si} = \Delta x_{PZ}^{0} - \Delta x_{LF}^{-}. \qquad (10a)$$

Substituting in (1) and (4) leads to:

$$\Delta x_{Si} = d_{PZ}V - \frac{F_{LF}}{k_{LF}}. \qquad (10b)$$

Then using (7) and (9) we find:

$$\Delta x_{Si} = d_{PZ}V - \frac{k_{Si}\Delta x_{Si}}{k_{LF}}. \qquad (10c)$$

Rearranging terms, we find:

$$\Delta x_{Si} = \frac{k_{LF}}{k_{Si} + k_{LF}} d_{PZ}V, \qquad (11)$$

which relates the measurable bending displacement of the Si cantilever to the applied voltage, the known stiffness of the cantilever, and the unknown load-frame stiffness and unknown piezoelectric coefficient.

Two separate experiments can be conducted on a single Si cantilever in order to determine the two unknowns k_{LF} and d_{PZ}. By concentrating the applied force at different positions along the length of the cantilever lever-arm, one achieves different values of the bending stiffness, k_{Si}. Using results from two such experiments, the constants were determined to be: k_{LF} = 320 N/m and d_{PZ} = 1.96 _m/V. Thus, the load-displacement-voltage relation describing an indentation experiment is given by inserting these constants into the following equation:

$$F_{sample} = k_{LF}\left(d_{PZ}V - \Delta x_{sample}\right) \qquad (12)$$

Figure 2.4.2 shows an *in situ* TEM image of the experiment in which the indenter bends a Si cantilever typically used for atomic force microscopy (AFM). The AFM imaging probe can be seen in the figure, but does not affect the experimental results. The displacement of the cantilever is directly measured from real-time images, as shown in Figure 2.4.3, and is correlated to the voltage applied to the piezo-ceramic element along with the applied force, which is calculated from the known bending stiffness. The coupled force-displacement behavior of the piezoceramic loading mechanism is demonstrated in the calibration curves shown in Figure 2.4.4. As this diagram demonstrates, the force applied by the indenter can be determined by knowing the voltage applied to the piezo and the displacement of the indenter.

3 Results and Discussion

3.1 Overview

Nanoindentation techniques are particularly useful for studying the mechanical behavior of thin films and, in general, small volume deformation mechanisms. To fully explore the promise of *in situ* nanoindentation in a TEM, a wide range of materials were studied for this dissertation. The materials studied can be grouped into three general classes of material systems: (1) bulk single crystal, (2) a soft thin film on a harder substrate and (3) a hard thin film on a softer substrate.

The deformation behavior of bulk silicon will be discussed in section 3.2, in which direct evidence of dislocation nucleation and motion in single crystal silicon at room temperature was observed. Previous studies of the indentation response in silicon have reported phase transformations and/or fracture as the primary modes of deformation. Section 3.2 presents real-time observations of nanoindentation in silicon, which show extensive dislocation-based plasticity during loading. Upon unloading, the plastically deformed volume leads to a residual stress that can induce non-crystallographic fracture. These results can be explained in part by the unique wedge geometry of the samples used, which yields a high ratio of shear stress to hydrostatic pressure. These observations indicate that high stresses confined to nanoscale volumes, as are realized in semiconductor devices, can lead to fundamental new mechanisms of deformation in silicon.

Section 3.3 documents results from *in situ* nanoindentation experiments performed on polycrystalline Al thin films deposited onto the silicon wedge substrates described in section 2.2. *In situ* nanoindentation has the unique advantage of being able

to explore the mechanisms of deformation in sub-micron grain sizes, where theories of bulk mechanical behavior do not always apply. Thus, events such as dislocation nucleation in initially defect-free material can be observed in real time. Additionally, effects of microstructure can be investigated in a unique way. For instance, the effects of grain size and orientation can be investigated directly through *in situ* positioning of the indenter at a grain of specific orientation and size. Or, choosing to indent directly on a grain boundary can provide insight into the role of grain boundaries in the deformation behavior of polycrystalline thin films. Section 3.3 will discuss the microstructural details of indentation, as well as present quantitative results using the voltage-controlled mechanical testing method discussed earlier in section 2.4.

Whereas section 3.3 describes indentations of a soft film (Al) on a relatively hard substrate (Si), section 3.4 describes indentations of hard films on relatively softer substrates. Experiments from two different thin film/substrate systems are described in section 3.4, both amorphous diamond on silicon and epitaxial TiN on MgO. When indenting a soft film on a harder substrate, the deformation of the film is not significantly influenced by the inherent properties of the substrate, and the substrate plays almost no role in the indentation behavior (at shallow indentation depths). However, when indenting hard film/soft substrate systems the indentation behavior of the system together plays a larger role. This was found to be true in both cases described in section 3.4, where the deformation of the hard films were found to be controlled in part by the deformation of the softer substrates.

3.2 Bulk Material (silicon)

Dislocations are not generally considered to be a relevant mechanism of deformation in brittle materials at room temperature. Over fifty years of research on dislocation behavior in silicon has demonstrated that dislocations do not move during conventional mechanical testing below a temperature of 450 °C[35,36]. A recent report by Kato, et al[37], described the generation of dislocations during room temperature fatigue around the active region of an advanced silicon-based device. While it was not certain from their study if the dislocations were generated during the fabrication of the device at higher temperatures or were created at room temperature, their report described the catastrophic electrical failure of the silicon transistor due to the presence of dislocations. Dislocation structures that have been observed around room temperature indentations in silicon have been explained to result from either block slip[38,39] or phase transformations[40,41,42], but the creation of these defects has never been observed. Although dislocation plasticity during indentation has been suggested in the literature[43,44], it is generally ignored or dismissed altogether[45,46]. Initially, indentation-induced fracture was considered to be the relevant deformation mechanism during loading[44] as well as unloading[43]. More recently, it has been proposed that a series of phase transformations occur during indentation. It is believed that silicon transforms to high pressure metallic phases (e.g. β-Sn) during loading, as is inferred by *in situ* Raman spectroscopy[5] and resistivity measurements[42]. Upon unloading, the high pressure metallic phases are thought to transform to either a low pressure metallic phase or undergo amorphization. Post mortem TEM analysis has provided evidence of both bcc-R8 and amorphous silicon phases[42], where the resultant phase is controlled by the unloading rate as well as the depth of indentation.

Direct nanoscale observations of the mechanisms of deformation during the earliest stages of indentation have only recently been possible through the technique of *in situ* nanoindentation in a transmission electron microscope (TEM)[47,48]. The *in situ* experiments described in this chapter were performed on <100> n-type single crystal silicon samples that fabricated lithographically as described in chapter 2.2. The wedge geometry allows the microfabricated silicon samples to provide for electron transparency as well as mechanical stability. Indentations were performed on two different wedge geometries, where the wedge was either terminated by a flat plateau ~150 nm in width, or sharpened to a plateau width of approximately ~20 nm. Scanning electron micrographs of cross sections from the *in situ* samples are shown in Figure 3.2.1, where the direction of indentation is indicated.

In situ nanoindentation experiments were performed on the silicon wedge samples to peak depths ranging between 50 and 200 nm. Indentations to depths greater than 200 nm were not performed *in situ* due to the inherent limitations in electron transparency of the wedge geometry. During *in situ* indentation the deformation is observed and recorded in real time, and diffraction patterns are taken directly after unloading. It was found that plastic deformation proceeds through dislocation nucleation and propagation in the diamond cubic lattice. Figure 3.2.2 shows a series of images taken during an indentation into the "blunt" geometry, which had a plateau of ~150 nm at the top of the wedge. Figure 3.2.2a shows the defect-free sample prior to indentation. Figures 3.2.2b and 3.2.2c show the evolution of elastic strain contours as the indenter presses into the sample – no evidence of permanent deformation is seen at this point. The elastic strain contours reveal the shape of the stress distribution in the sample (these are essentially the contours of principal stress). Figures 3.2.2d and 3.2.2e clearly show the nucleation and propagation

of dislocations from the surface as deformation proceeds. This particular indentation was taken to a peak depth of 54 nm, resulting in the plastic zone shown in Figure 3.2.2f.

Post-indentation TEM micrographs of the same indentation documented in Figure 3.2.2 are shown in Figure 3.2.3, and include the corresponding selected area diffraction patterns of the indented region. Due to the high density of dislocations after indentation a slight broadening of the diffraction spots is observed. However, no additional diffraction spots or rings are present after indentation as compared to diffraction patterns taken prior to indentation. This indicates that no additional phases (crystalline or amorphous) have formed. Figure 3.2.3a shows a bright-field TEM micrograph of the indented region in the zone axis condition. Figure 3.2.3b is a dark-field condition using the $(0\bar{2}2)$ diffracted beam, showing that at least one edge of the plateau is still continuous across the indented region.

In the case of the "sharp" wedge geometry the deformation behavior during indentation was identical to the case described above, showing dislocation plasticity during loading. Upon unloading, however, fracture occurred in several of the indentations. Figure 3.2.4 shows post-indentation TEM micrographs of one such indentation into the sharp wedge geometry. As can be seen in Figure 3.2.4a, the fracture surface is smooth and non-crystallographic (within the resolution limit of the bright field TEM image). During unloading two cracks were observed to nucleate at the surface and propagate along a strain contour to the center, forming the semicircular fracture profile shown in Figure 3.2.4a. Figure 3.2.4b shows the dramatic contrast between the crystallographic nature of the dislocations nucleated during indentation and the non-crystallographic nature of the fracture surface.

It has been shown that stresses near the ideal shear strength are reached during indentation into defect-free *metal* systems, resulting in the nucleation of

dislocations[48,49,4]. However, the critical shear stress for dislocation nucleation in metallic materials is far less than that for silicon, owing to the high Peierls barrier of the latter (which is directly related to the strong covalent bonding in silicon). During conventional indentation experiments in silicon, it is generally believed that deformation is accommodated by phase transformation and/or fracture, rather than dislocation plasticity. The phase transformations that occur during indentation have also been observed during diamond anvil cell experiments, where high hydrostatic pressures are applied[50,51,52,53]. It follows that during conventional indentation experiments in silicon, the critical pressure for phase transformation is reached before the shear stress reaches the critical value for dislocation nucleation.

With the *in situ* experiments, however, the unique sample geometry employed leads to fundamental differences in the stress state imposed by the indenter, which in turn influences the resultant mode of deformation. Conventional indentation experiments are conducted on samples well described as a flat half-space (e.g. a silicon wafer). In the case of the silicon wedge sample geometry, the sides of the wedge are of <111> orientation, making an angle of 70.5° to each other, and are separated by a flat plateau of <100> orientation. The plateau width, w, the wedge height, h, and the length of the wedge, L, have the relationship: L>>h>>w, such that the geometry is better described as a plane stress configuration than the plane strain configuration characterizing conventional indentation experiments. A plane stress configuration is defined by a lower hydrostatic component than a plane strain configuration. Thus, the observations of dislocation plasticity rather than phase transformation can be explained by the difference in stress state in these samples, as compared to conventional experiments. In the case of the *in situ* experiments, an increase in the ratio of maximum shear stress to hydrostatic pressure

allows the shear stress to reach the critical value for dislocation nucleation before the hydrostatic stress reaches the critical value for phase transformation.

Fracture in silicon is widely observed, not only in indentation experiments, but in most mechanical tests. However, ductility is generally not considered to play a role in the fracture of brittle solids. However, in the case of the *in situ* experiments, fracture appears to be a direct result of the presence of dislocations. The plastic zone, characterized by the newly created dislocations, leads to a residual stress field upon unloading. As described by Lawn[38] a residual tensile field arises during unloading due to the accommodation of the plastically deformed volume and the surrounding elastic volume. This field is comprised of high tensile stresses which drive fracture. Surprisingly, the path of crack propagation is non-crystallographic. Rather than cleaving along the lowest energy planes, the crack follows a strain contour associated with the residual stress field. This is energetically favorable if the stress along the strain contour is on the order of the theoretical cohesive strength of silicon.

Figure 3.2.5 is a schematic representation of the fracture event described above. While the stresses under the indenter are inherently inhomogeneous, the stress state directly under the indenter along the indentation direction axis can be reasonably described as compressive during indentation. In figure 3.2.5a the schematic describes the stress state in this way. Upon the nucleation of dislocations underneath the indenter, the compressive stresses are at least partially relieved by the plastically deformed volume as noted in figure 3.2.5b. Upon unloading, therefore, the plastically deformed volume leads to a residual tensile field as shown in figure 3.2.5c. Since the material deformed plastically to accommodate the imposed pressure of the indenter, it is reasonable to expect the reversal of the stress field to a tensile character upon unloading, and relaxation of the pressure induced by the indenter. Thus, the stresses due to this residual tensile field

can be relieved by a fracture event, as shown in figure 3.2.5d. Notably, fracture was not observed in the blunt wedge geometry. This can be explained by the smaller surface area associated with fracture of the sharp wedge geometry.

3.3 Soft thin film on hard substrate (Al on Si)

The mechanical behavior of Al thin films has important relevance to the microelectronics industry, where Al metallization is used throughout a typical microchip. Since the grain size of a metallic thin film typically scales with the thickness of the film, a variety of grain sizes can be studied by controlling the thickness of the film. Thus, the mechanical behavior of sub-micron sized films and the mechanisms of deformation in sub-micron sized metallic grains can be studied directly.

In the case of the polycrystalline Al films studied here, the films were deposited on the silicon wedge substrates by evaporating 99.99% pure Al at 300° C. A film thickness of approximately 250 nm gave the maximum thickness while still maintaining electron transparency at 200kV. When performing *in situ* nanoindentation, a the maximum possible thickness that is still electron transparent is most ideal, since the thinner a sample the more likely the indenter would simply bend the sample versus actually indent. During *in situ* nanoindentation of the Al films, the 3-sided diamond pyramid indenter approaches the sample in a direction normal to the electron beam (Figure 3.3.1). The diamond indenter is boron-doped in order to be electrically conductive in the microscope. The sample is a thin film deposited onto a silicon substrate that includes a narrow wedge. The indentation is made in the cap of film on the flat top of the wedge, which can be seen in figure 3.3.1

The interpretation of conventional nanoindentation data is not always clear. For example, since most metals form native oxides yielding under the nanoindenter may be governed by fracture of the oxide film rather than the onset of plastic deformation in the material itself.[20] It is difficult to resolve such since the mechanisms associated with yielding are only indirectly elucidated from quantitative load vs. displacement behavior.

Thus, the most significant advantage from performing *in situ* nanoindentation inside a transmission electron microscope (TEM) is the ability to record the deformation mechanisms in real time, avoiding the possibility of artifacts from post-indentation sample preparation. However, since the Peierl's barrier in Al is extremely low and consequently the dislocation velocity is very fast, our video sampling rate of 30 frames per second is too slow to capture the movement of the individual dislocations. Hence, each video image captured during the *in situ* experiments presented here is essentially a quasi-static image of the equilibrium configuration of defects. Figure 3.3.2 illustrates this point by showing a series of six images taken from a video during an *in situ* nanoindentation experiment. In Figure 3.3.2a, the diamond is approaching an Al grain that is approximately 400 nm in diameter. Figures 3.3.2b and 3.3.2c show images of the evolution of the induced stress contours during the initial stage of indentation, and correspond to purely elastic deformation in the absence of any pre-existing dislocations that could cause plasticity. Figure 3.3.2d shows the first indication of plastic deformation, in which dislocations are nucleated; a set of prismatic loops is observed. Figures 3.3.2c and 3.3.2d are consecutive frames of the video, and are ($1/30^{th}$) of a second apart. As can be seen, the exact location of the nucleation event is not discernable, since the evolution of the dislocation configuration has already proceeded beyond the point at which that might be possible. Figures 3.3.2e and 3.3.2f show the large increase in dislocation density achieved as deformation proceeds, and dislocations tangle and multiply.

In order to study the crystallographic mechanisms of nanoindentation in detail it is more useful to use dark-field TEM. In a dark field condition, the image is formed by using a strongly diffracted beam of electrons from one grain only. Unfortunately, it is not

possible to image the indenter simultaneously with a dark-field image of the grain, so the depth of indentation cannot be monitored.

Figs. 3.3.3 and 3.3.4 show examples of the information that can be obtained from dark-field TEM images. Fig. 3.3.3 includes a series of micrographs from the video record of an *in situ* nanoindentation of an Al grain that was oriented in approximately the [-1-11] direction. Figs. 3.3.3(a) and 3.3.3(b) are micrographs taken prior to indentation in bright field, and dark field respectively. Figs. 3.3.3(c) and 3.3.3(d) show the evolution of nanoindentation damage. As expected, dislocations glide along close-packed {111} planes, and multiply and tangle as the deformation proceeds.

Fig. 3.3.4 is a more detailed examination of the development of dislocations near the yield point of the sample shown in Fig. 3.3.3. The top picture shows the entire Al grain at +0.6 seconds, followed by a series of pictures taken 0.1 seconds apart and cropped from the region outlined by the white box in the top picture. The most striking feature is the sequential appearance of prismatic dislocation loops on an axis approximately 45° from the direction of indentation, a mechanism of nanoindentation-induced deformation that has been suggested by several researchers.[5,54,55] Typically, in order to determine the Burger's vector of a dislocation in a TEM it is typically necessary to tilt the sample to multiple diffracting conditions in multiple zone axes. In the case of *in situ* experiments, it is only possible to image an evolving defect in one diffracting condition at a time, and thus not usually possible to determine the exact character of a defect during an *in situ* experiment. However, a study by Bell and Thomas[56] in 1965 showed that the character of prismatic loops in Al could be determined through geometrical analysis alone without necessitating g.b=0 tilting experiments. Bell and Thomas discovered that in fcc crystals such as Al, perfect prismatic dislocation loops lying on {111} planes projected not a loop, but a double arc image onto the surface of the

foil in diffraction contrast. This double arc image was shown to correspond to the Burger's vector such that a line connecting the missing segments of the loop image lies along a <110> direction parallel to the Burger's vector of the perfect loop. As can be seen in Figure 3.3.4, the dislocation image is in fact a double arc where the line of no-contrast can be seen to lie in a <110> direction. Thus, even without being able to tilt the sample to multiple diffraction conditions *in situ*, it can be determined that the dislocation image in Figure 3.3.4 corresponds to a prismatic dislocation loop with a a/2 <110> Burger's vector. Since the loops are prismatic rather than shear in nature, they are presumably formed at the surface rather than nucleated in the bulk. However, the actual nucleation and migration of the loops to the site at which they appear is too rapid to capture, as is their motion to new equilibrium positions as additional prismatic loops are punched into the grain.

The peak stresses applied to a material during indentation occur below the surface[15]. Thus, elastic contact theory suggests that nucleation should occur from the bulk, below the indenter/sample interface. However, the in-plane stresses imposed at the surface are not zero. During a nanoindentation test into an initially defect-free solid volume the initiation of the defects necessary to accommodate the induced deformation can occur at a number of locations, including the surface, the interface of the native oxide layer with the bulk material, or the interior of the grain.[20] This competition for the location of the initial defect nucleation will depend on numerous material and indentation parameters, including the surface properties of the material and the resulting defects.

Although the precise nucleation site may be difficult, if not impossible, to establish from such experiments, *in situ* indentation experiments provide unique advantages over *ex situ* TEM analysis of post-indent dislocation configurations. In addition to the difficulty in preparing TEM samples after indentations have been

conducted, the strong image forces exerted on the dislocations by the free surface can lead to very different structures after the sample has been unloaded. Indeed, in our studies it has been observed that the configuration of defects changes dramatically after the dislocations have had time to rearrange themselves and, possibly, anneal out of the sample. During the *in situ* experiments on the Al thin films, it is observed that the configuration of dislocations that result during loading is usually lost within minutes of unloading the sample. Specifically, the image effects of the sample surface almost always lead to a dramatic decrease in the number of dislocations left in the sample after the indentation.

As compared with an instrumented nanoindentation of a typical thin film (which is essentially infinite in two dimensions), our *in situ* sample design substantially increases the amount of surface interacting with a resulting defect configuration. Since the elastic fields of a dislocation are typically on the same order as the thickness of a thin film, it would be expected that the surface of a typical thin film under instrumented nanoindentation would also exhibit the ability to absorb dislocations. This observation suggests that *post mortem* TEM studies of indentation damage and microstructures taken after nanoindentation experiments should be viewed with some caution.

In order to demonstrate the effect of the surface on the resulting dislocation configuration, Figure 3.3.5 shows three post-indent images of the same experiment documented in Figure 3.3.1. In this case, Figure 3.3.5a is a bright field image taken approximately 2-3 minutes after the indentation. Figure 3.3.5b is a dark field image using the same exact diffraction condition, and taken approximately 2-3 minutes after the bright field image (3.3.5a). Figure 3.3.5c is the same two images overlaid on top of each other, in which we can directly compare the dislocation configuration shown in the bright field condition (where the dislocations look black) and that shown in the dark field condition

(where the dislocations look white). A bright field and a dark field image are not necessarily exact negatives of each other. However, in an isotropic material such as Al any defect seen in a dark field configuration would certainly have to show up in a bright field image using the same diffraction condition. In this case, it can be seen that the dislocation configurations do not match, and that the dark field condition shows dislocations that are not seen in the bright field condition (for example, the dislocation at the end of the [-1-11] arrow). Thus, what was inadvertently documented with the two images 3.3.5a and 3.3.5b is the rearrangement of the post-indent dislocation configuration that must have occurred sometime during the 2-3 minutes between the time that the bright field and dark field images were captured.

Using the methodology described in section 2.4 to correlate the microstructural response of a material with quantitative information demonstrates the full potential of the *in situ* nanoindentation technique. Fig. 3.3.6 shows an example force-displacement curve from an *in situ* nanoindentation test. The film was vapor-deposited Al, with a grain size of 250-400 nm. An Al grain at the cap was indented in a <113> direction, and monitored continuously in bright field TEM. The test was filmed, and example TEM micrographs were copied from the film to illustrate characteristic stages of the indentation process.

Fig. 3.3.6 a shows the indenter and the defect-free Al grain just before contact. In Fig. 3.3.6 b (point B on the curve) the indenter imposes an elastic strain, indicated by the dark strain contour in the micrograph. The indentation remains elastic until the film yields, at point C. At yield (Fig. 3.3.6 c) a dislocation forms at the surface and propagates into the film. After yielding the indenter penetrates at nearly constant load (region D), while dislocations form and flow into the grain to preserve an essentially constant dislocation density (Fig. 3.3.6d). The test was stopped after about 30 nm indentation since the diameter of the contact area (> 100 nm) had become significant with

respect to the radius of curvature of the sample tip. While the native oxide at the film surface is not clearly imaged, oxide rupture does not appear to play an important role; there is no yield point, and dislocations appear at the onset of plastic deformation.

The force-displacement relation in Fig. 3.3.6 is superimposed on nanoindentation curves of single crystal Al of various orientations taken from two different sources. The data published by Gouldstone, *et al.*,[3] is from indentations of epitaxial Al films in the (110), (133) and (111) orientations. The data from Lilleodden[57] is from nanoindentation of bulk single crystal Al in the (111) orientation. All three sets of data (*in situ*, Gouldstone, Lilleodden) are taken from tests using similar tip geometries (radius ~50 nm). Both the Gouldstone and Lilleodden data exhibit the "staircase" shape that is typical of nanoindentation of ductile metals.[58] The steps in the staircase are, presumably, due to the fact that hardening or defect exhaustion requires successively higher stresses to continue plastic deformation. In the *in situ* nanoindentation tests done to date on Al, plastic flow is not exhausted at displacements up to 30 nm, and the second step of the staircase is not seen. Presumably, this is due to the geometry of the *in situ* specimen, which provides a much larger free surface to absorb dislocations and minimize hardening.

A previous study by Lilleodden and Nix showed that the indentation behavior of thin gold films showed characteristic differences in the loading behavior that was related to the grain size of the samples[57,59]. For a 1 micron thick Au film, with an average grain size of 3 microns, it was found that the load-displacement response is similar to that found in bulk single crystals. The load-displacement behavior of this coarse-grained sample is presented in Figure 3.3.7, showing Hertzian elastic response followed by discrete bursts of plasticity. This behavior has been termed "staircase" yielding[60], and is often observed in single-crystalline samples. Also shown in Figure 3.3.7 is the load-

displacement behavior associated with indentation into a 160nm Au film characterized by an average grain size of 100nm. In contrast, the finer-grained sample resulted in continuous elastic-plastic loading from the onset of contact. A likely reason for this behavior is that dislocations can be easily emitted from the nearby grain boundaries in fine-grained samples, but must be found or formed in the interiors of grains in coarse-grained samples.

Figure 3.3.8 shows a similar result achieved in this study through *in situ* nanoindentation tests into Al grains of two different sizes. *In situ* nanoindentation has the advantage that the grain size is readily observable, and can be determined uniquely for each indentation. In this case, two indentations were made, into grains of different diameters. The "large" grain had a grain diameter of 670 nm, which is significantly larger than the indenter radius. The "small" grain had a grain diameter of approximately 100 nm, which is about the same size as the indenter radius. Both grains were approximately 250nm in thickness. The qualitative indentation responses for the two grains showed the same characteristic difference observed by Lilleodden and Nix for indentations into Au films. The large grain Hertzian elastic contact followed by discrete plasticity, while the small grain showed elastic-plastic response from the onset of contact. Included in Figure 3.3.8a is the raw voltage vs. displacement responses associated with the indentations into Al. Irrespective of our calibration, the characteristic difference in indentation response between the large and small grain is still observed.

In polycrystalline metals with relatively large grain sizes (e.g. > 1 micron), grain boundaries are thought to behave primarily as barriers to dislocation motion. Consequently, a typical method for increasing the hardness of a metal is to change the composition or processing of the material in order to decrease the average grain size, thus increasing the total area of grain boundaries and increasing the barriers to dislocation

motion. This basic premise of microstructure-property relations in metallurgy is known as Hall-Petch behavior, since the first studies to relate grain size with the strength of a material were performed by Hall[61] and Petch[62] in the early 1950s.

There are other known mechanisms by which grain boundaries can influence the mechanical behavior of a polycrystalline metal. Li[63] described an alternate role for grain boundaries in 1963, when he first proposed that grain boundaries be thought of as sources for dislocations rather than only barriers to their motion. Indeed, recent reports using computational studies of nanoindentation have shown that relatively easier dislocation nucleation at grain boundaries can serve to lower the load at which plasticity is initiated[64].

As grain size decreases, the volume of the material associated with grain boundaries increases dramatically. For instance, the amount of material associated with a grain boundary changes from 0.01 % for 3 micron grains, to 0.1 % for 300 nm grains and to 1 % for 30 nm grains[65]. For a given indenter size, the interaction of an indenter grain boundaries increases as the grain size decreases. Thus, it should not be surprising that the deformation behavior associated with increased grain boundary interaction might involve mechanistic changes. These mechanistic changes might include grain boundary sliding[6667], dislocation nucleation from the grain boundary[64], or even grain boundary movement. This final mechanism, grain boundary movement, has been observed in more macroscopic experiments, but is not typically mentioned as relevant behavior for small scale deformation. Winning, *et al.*[68] described the motion of Al tilt boundaries under imposed external stresses, and suggested the movement of the grain boundaries was achieved through the movement of dislocations that comprised the structure of the boundaries. Merkle and Thompson[69] ascribed the motion of grain boundaries in Au to a more localized phenomenon- the rearrangement of groups of atoms near a grain boundary

to be incorporated into a growing grain. Whether the grain boundary motion is accomplished through dislocation motion or atomic rearrangement, there exists a driving force for a grain to grow or shrink under an inhomogeneous external stress. The stresses imposed by a nanoindenter are inhomogeneous[15], and can be expected to provide a significant driving force for the movement of grain boundaries. In fact, the movement of grain boundaries during *in situ* nanoindentation was observed to be considerable in Al grains under ~`400 nm in width, and these initial observations will be described below.

When the contact area of the indenter is small compared to the grain size, the grain boundaries in the Al films were seen to act as barriers for dislocation motion. Figure 3.3.9 shows one such case. The al grain is shown before indentation in figure 3.3.9a to be clear of any defects. Deformation occurs during *in situ* nanoindentation through the creation and propagation of dislocations within the grain, as the post-indentation TEM micrograph in figure 3.3.9b shows. The dislocations can be seen to extend to the film/substrate interface as well as the boundaries with the grains to each side. In this case, the indentation contact area (which can be seen in figure 3.3.9b as the area on the surface with removed material) was relatively small in comparison to the lateral size of the grain. The width of the contact area is roughly 40% of the lateral width of the grain. Figure 3.3.10 shows a similar case where the before (figure 3.3.10a) and after (figure 3.3.10b) figures show the dislocations interacting even less with the grain boundary than the previous example. In both cases, the observed post-indentation microstructure is characteristic of typical large-grained Hall-Petch type behavior, where the grain boundaries are stationary and act as barriers to the motion of dislocations.

Figure 3.3.11 shows a different situation, where the size of the indentation contact area is very large compared to the size of the grain, and in fact the indenter imposes directly onto the grain boundary during indentation. Figure 3.3.11a is a TEM image of

two Al grains taken before indentation. Figure 3.3.11b is a TEM image of the same two grains after indentation, where the deformation of the grain boundary which had been within the contact region of the indenter is extensive. Figure 3.3.11c is the same two images, 3.3.11(a) and (b) overlaid on each other, showing that the grain boundary had moved extensively during the indentation. Undoubtedly, the change in equilibrium position of the grain boundary with respect to the two grains shows that the grain boundary must have participated in the deformation of the film in a substantial way. Figure 3.3.12 shows a time series taken from an indentation directly onto a ~ 6° tilt boundary between two Al grains. Here, the surprisingly large *in situ* movement of the grain boundary during the indentation can be seen directly.

Figure 3.3.12a shows the indenter approaching the grain boundary from the bottom of the frame. Figures 3.3.12 (b)-(d) are three images only 0.6 seconds apart, taken 18.2 seconds from the start of the indentation. The grain boundary can be seen to change positions dramatically even over this short time frame (1.8 seconds for the three images). Dislocations can also be seen extending from/to the grain boundaries in each grain. Figure 3.3.12e is the final position of the grain boundary after the indenter has been removed, which is similar in location to the grain boundary's original position. This is more evidence that *ex situ* characterization of nanoindentation experiments would miss important microstructural phenomena. Although the before (figure 3.3.12a) and after (figure 3.3.12e) positions of the tilt boundary are very similar, the boundary had actually moved considerably during the indentation. Figure 3.3.12f is a diffraction pattern of both grains, showing two strongly-diffracting planes, one from each grain. These initial observations suggest that grain boundary motion is a significant mechanism of deformation during nanoindentation, and in fact might play a large role in the softening of materials with sub-micron grain sizes.

3.4 Hard thin films on softer substrates

As described in section 3.3, when a thin film is considerably softer and more compliant than its substrate, plastic deformation is confined to the film. In thin film/substrate systems where the substrate is either softer or more compliant, however, the mechanical properties of the substrate will influence the indentation behavior at even shallow indentation depths. In the analysis of nanoindentation data, an elastically inhomogeneous thin film/substrate system gives rise to a so-called "substrate-effect", where the mechanical properties of the substrate influence the mechanical properties of the film extracted from a nanoindentation experiment[70]. At significant indentation depths, the substrate effect is not only caused by differences in the elastic properties between the film and substrate but can be influenced by plastic deformation in the substrate. With *in situ* nanoindentation, the onset of plastic deformation in both a thin film and its substrate can be observed directly. In contrast to the case of Al on Si, this section details two thin film/substrate systems where the films were considerably harder and stiffer than their respective substrates. First, the *in situ* nanoindentation of amorphous diamond films on the silicon wedge substrates will be discussed in section 3.4.1. The second hard film/soft substrate system studied is epitaxial TiN on MgO of (100) orientation, which is discussed in section 3.4.2. The elastic moduli and hardness values of the film and substrate materials are listed below in Table 3.4.1:

Table 3.4.1- Mechanical Property Data

Material	Young's modulus (GPa)	Hardness (GPa)
Amorphous Diamond[74]	550	80
Silicon[76]	160	12
TiN[76]	480	20
MgO[76]	310	4.2

3.4.1 Amorphous diamond thin films on silicon

Amorphous diamond (a-D) thin films have great potential to be used as surface coatings for MEMS devices due to their excellent conformality, superior mechanical properties and biocompatibility. The a-D films grown for this study were deposited at Sandia National Laboratories in Albuquerque, NM, under the direction of Dr. Thomas Friedmann. The details of the a-D film deposition have been reported elsewhere[71,72]. The a-D thin films were deposited by pulsed laser deposition from a graphite target which resulted in highly sp3-bonded, but amorphous, carbon films. The a-D films are typically deposited with extremely high intrinsic film stresses, which are in fact thought to be part of the growth mechanism[73]. Amorphous diamond films grown in the same chamber as the films used here have been measured with wafer curvature methods to have intrinsic compressive stresses between 6 and 8 GPa. However, stress relief can be achieved by annealing the films at elevated temperatures. By annealing the a-D films at 600° C for only two minutes, the residual stresses fall below 0.1 GPa. Even after being annealed the films retain their diamond-like, sp3 bonded character and result in amorphous films with hardness values approximately 80-90% that of crystalline diamond[74].

Similar to the Al samples described in the previous chapter, the a-D films were deposited directly onto the micromachined silicon wedges. The films were deposited to a thickness of 120 nm, and then annealed at 600° C for five minutes to relieve the growth stresses. Indentations were performed on the cap of film at the peak of the silicon wedge, which was terminated by a plateau approximately ~20 nm in width. A scanning electron micrograph of a cross section from an a-D coated *in situ* sample is shown in Figure 3.4.1, where the direction of indentation is indicated.

Since the a-D thin film was considerably harder than the silicon substrate underneath it should be expected that the deformation of the film would be controlled by the deformation of the underlying substrate. Indeed, it was found during *in situ* nanoindentation that the deformation of the a-D thin films was either minimal or nonexistent. As the indenter penetrated the a-D on Si sample the underlying silicon deformed before any noticeable damage to the a-D thin film. Although it is not possible to observe the mechanisms of plasticity in an amorphous film using diffraction contrast, no spalling or cracking of the a-D film was observed. Figures 3.4.2 and 3.4.3 show bright field, and dark field TEM micrographs of a post-indentation microstructure, respectively. As can be seen, the silicon sample deformed through dislocation nucleation and propagation, while the a-D thin film showed minimal decrease in thickness even at the point of indentation. The decrease in film thickness was less than the total indentation depth. Diffraction patterns taken after indentation are shown in Figures 3.4.4 and 3.4.5, and are identical to the diffraction patterns of the samples prior to indentation, except for the slight broadening of the spots due to the presence of a high density of dislocations post-indentation. The deformation in the underlying silicon was highly localized, and resulted in dimpling of the a-D film with no occurrence of spalling. In fact, the deformation in the underlying substrate what characteristically the same as when the silicon wedges are left uncoated, as discussed in chapter 3.2.

Mechanical deformation does not typically yield exactly repeatable microstructures. The inherently statistical nature of dislocation interactions and other small-scale defects within a material can lead to a differences in the chain of events during indentation, yielding unique deformation microstructures from indentation to indentation. However, an amorphous film on top of a single crystal substrate is an ideal sample for observing nearly repeatable microstructures after indentation. This turned out

to be the case as the deformation microstructure of the a-D on Si samples was characteristically similar from indentation to indentation (for a given indenter and indentation depth). Figures 3.4.6-3.4.9 demonstrate this point by comparing the resulting microstructure from two different indentations in two different imaging conditions. Figures 3.4.6 and 3.4.7 are two different indentations both imaged in a bright field (g=-400) condition, corresponding to the diffraction pattern in Figure 3.4.4. Figures 3.4.8 and 3.4.9 are the same two indentations imaged in identical dark field (g=13-1) conditions, corresponding to the diffraction pattern shown in Figure 3.4.5.

The purpose of a hard surface coating is to protect the underlying material from mechanical and chemical damage. In the case of sharp silicon wedges, it has been demonstrated first-hand that the a-D thin films do not de-cohere from the silicon substrate during nanoindentation. A significant advantage of the a-D thin films is the high degree of conformality when deposited on intricate substrates- as is demonstrated in the even deposition over the ultra-sharp silicon wedges shown in Figure 3.4.1. Even during nanoindentation, where the stresses underneath the indenter can reach the theoretical strength of the material[24], the a-D thin films are shown to retain their adherence to the substrate.

3.4.2 Epitaxial TiN on MgO (100)

The transition metal carbonitrides are a technologically important class of materials whose mechanical properties are still poorly understood.[75] For example, it has been shown that within a given class of materials hardness values typically scale with the shear modulus.[76] Within the transition metal carbonitrides their exists some striking discrepancies to this trend. In particular, while TiC and TiN have very similar shear moduli, the hardness of TiC is approximately %150 the value of TiN. The underlying explanation for this relationship is not well understood. It is believed that the slip of dislocations does not occur at room temperature in these materials, and their precise deformation mechanisms are not well known.[77] Recently, theoretical work has suggested that the transition metal carbonitrides are materials whose mechanical behavior might be related to their ideal strength behavior[26,78].

The deformation mechanisms of the transition-metal carbonitrides are particularly difficult to study due to their characteristically high melting temperatures[79]. TiN, for instance, has a melting temperature of 3000°C. The growth of TiN in thin film form is thus always at a temperature of less than half the homologous temperature, since high vacuum growth chambers cannot be operated at temperatures greater than ~1000°C[80]. Because of their necessarily low homologous growth temperatures, transition-metal carbonitride thin films are typically grown with a relatively high amount of intrinsic defects and very small grain sizes[81]. High defect densities and small grain sizes make the imaging of these materials difficult when using diffraction contrast in a TEM. Because of the high defect densities in as-deposited films, microstructural changes related to any induced deformation is easily obscured by the intrinsic defects. However, it is possible to grow heteroepitaxial thin films of TiN on relatively large pieces of single crystal MgO.

Since the epitaxial films are free of grain boundaries, they are more ideal for studying the fundamental deformation mechanisms in these materials.

In order to study the fundamental deformation mechanisms in TiN using *in situ* nanoindentation, TiN was deposited epitaxially on single crystal MgO with (100) orientation. The ~350 nm thick films were deposited by ultrahigh vacuum reactive magnetron sputtering on MgO (001) at 850 °C in pure N 2 discharges maintained at a pressure of 5 mTorr (~0.67 Pa). The films were deposited at the Frederick Seitz Materials Research Laboratory at the University of Illinois, Urbana-Champlain, under the direction of Dr. Ivan Petrov. The details of the film deposition have been reported elsewhere[82,83,84,85]. In order to prepare the samples for the *in situ* nanoindentation experiments, a Focused Ion Beam was used to mill the samples to the proper geometry. This method, and the manner in which the sample was protected from the incident ion beam was discussed in chapter 2.3.

Figure 3.4.10 shows the epitaxial TiN/MgO (100) sample prior to indentation. As can be seen by both the bright field (Figure 3.4.10a) and dark field (3.4.10b) micrographs, there exists a very high density of defects in the TiN pre-indentation microstructure. It is not known whether these defects were created during the growth of the film or ion beam milling. Both processes are known to create defects. The exact character of these defects is also not known, since their size is too small to be individually resolved with the TEM (at the sample thickness required for an *in situ* nanoindentation). Damage layers have been reported in numerous materials as a result of ion beam thinning[86]. The implantation of the energetic Ga+ ions (typically 30 keV) is known to cause amorphization in a layer 30 nm thick in Si[87]. No studies have been found on Ga+ ion damage to TiN specifically.

While the origin and character of the defects seen in the TiN films in Figure 3.4.10 are not known with exact certainty, there is reason to believe they are growth defects such as voids and dislocations and not damage from the focused ion beam preparation. There are two reasons to suspect this: (1) The MgO substrate was exposed to the same dose of Ga ions and does not show any damage. (2) An amorphous layer would not give rise to the diffraction contrast seen in Figure 3.4.10. The dark spots in the bright field picture, and the bright spots in the dark field picture signify crystallographic defects. However, it should be noted that MgO and TiN most certainly have a different susceptibility to Ga beam damage, and that ion implantation has been also shown to cause crystallographic defects that could give rise to strong diffraction contrast in a TEM [88, 89,90].

As was the case in the *in situ* nanoindentation experiments of the amorphous diamond on silicon, the TiN on MgO is a system where the film is considerably harder than the substrate. In the case of the deformation in the silicon substrate, the limited motion of the dislocations in the silicon during indentation resulted in highly localized deformation, and a dimpling of the amorphous diamond film. During the indentation of the TiN/MgO, plastic flow in the MgO was extensive, and the TiN deformed by more limited dislocation motion. Figures 3.4.11a and 3.4.11b show bright field and dark field micrographs of the post-indentation microstructure from an indentation taken to a peak depth of approximately 100 nm. Dislocations have arranged themselves in what closely resembles a hemispherical plastic zone surrounding the point of indentation in the TiN. The post-indentation surface of the TiN at the contact interface was so heavily damaged that it simply appears black in both bright field and any attainable dark field conditions. This indicates that the black region at the point of indentation in TiN has such a high

defect density that the electrons entering this region are almost completely absorbed or scattered.

During the *in situ* indentation a large amount of dislocations were generated in the MgO substrate at the film/substrate interface. As can be seen in Figure 3.4.12, indentation-induced dislocations propagated approximately twice as far in the MgO substrate as in the TiN film. During this relatively large indentation (the indentation depth was approximately 1/3 of the film thickness), the TiN film did not de-adhere from the MgO substrate. Rather, the TiN film was forced to accommodate the plastic deformation of the MgO substrate by bending. The extensive nature of the plastic deformation in the MgO led to a bending of the TiN film, as observed figure 3.4.12. A hemispherical distribution of dislocations led to a 8° rotation of the crystal around the <001> axis underneath the indenter. The crystal was bent 4° on each side of the indentation, as evidenced by comparing pre-indent and post-indent diffraction patterns.

Figure 3.4.13 shows the post-indent hemispherical plastic zone in the TiN along with selected area diffraction patterns of the TiN film taken before and after the indentation. The circle drawn on the TEM micrograph in Figure 3.4.13a shows the region of the TiN from which the diffraction information was taken. Figure 3.4.12c shows the splitting of the (-220) diffraction spot into approximately two spots, with 8° of rotation between them (around the <001> zone axis). These two spots now represent each side of the TiN underneath the indenter, where the TiN film has formed what is effectively a diffuse grain boundary. Essentially, as the splitting of the (-220) spots show, one could now describe the TiN film as having a diffuse, 8° tilt boundary formed directly underneath the axis of the indentation direction. This boundary is comprised of a dislocation array formed during the indentation.

4 Conclusion

This dissertation presented the novel mechanical testing technique of *in situ* nanoindentation in a TEM. In order to perform the experiments, unique specimen preparation techniques were employed. Silicon substrates were lithographically-prepared through the development of a new microfabrication procedure. Additionally, a method of sample preparation utilizing a focused ion beam was developed for bulk or thin film materials which could not be deposited onto the microfabricated silicon substrates. In order to correlate results from in situ and conventional indentation experiments, a method of voltage-controlled mechanical testing was derived theoretically and proven experimentally. This method of voltage-controlled mechanical testing enabled the quantification of the mechanical behavior during the *in situ* nanoindentation experiments without the use of an independent force or displacement measuring mechanism.

Three classes of material systems were studied with this new technique: (1) bulk single crystal, (2) a soft thin film on a harder substrate and (3) a hard thin film on a softer substrate. The direct observations of each material system during indentation provided unique insight into the interpretation of *ex situ* nanoindentation tests, as well as to the intrinsic mechanical behavior of nano-scale volumes of solids.

The *in situ* nanoindentation results presented in section 3.2 provided the first direct evidence of dislocation nucleation in single crystal silicon at room temperature. In contrast to the observation of phase transformations during conventional indentation experiments, the unique geometry employed for the *in situ* experiments resulted in

dislocation plasticity. The wedge geometry leads to a higher ratio of shear stress to hydrostatic pressure than that which is associated with conventional nanoindentation experiments, and therefore leads to a change in the mode of plastic deformation. Furthermore, it was shown that a residual tensile field, which results from the plastically deformed volume, can lead to non-crystallographic fracture upon unloading. These observations provide a crucial new insight into the failure of silicon-based microelectronic devices. If silicon is subjected to high stresses where the ratio of shear stress to hydrostatic pressure is large, room temperature nucleation and motion of dislocations is indeed possible. This observation indicates a fundamental new mode of deformation in this important material, as well as one that is practically realizable as the dimensions in advanced silicon devices continue to shrink.

Using this *in situ* indentation technique, indentations into Al thin films were presented in section 3.3. These results included the first real time observation of dislocation nucleation during nanoindentation of an initially defect-free Al grain. Using the voltage-controlled mechanical testing technique, for the first time a force vs. displacement curve was directly correlated to the microstructural response of a material during nanoindentation. A sharp change in the force-displacement response at the elastic-to-plastic transition was shown to signify the nucleation of dislocations, as has been implied by conventional nanoindentation investigations. The measured loading behavior was shown to be consistent with high-resolution force-displacement data obtained with instrumented indentation techniques. Plastic deformation in the Al proceeded through the formation and propagation of prismatic loops punched into the material, and half-loops that emanated from the sample surface. Furthermore, contrasting behaviors in fine and coarse-grained samples during *in situ* nanoindentation showed the same trend observed for indentations into large and small grains in conventional

nanoindentation data. Significant grain boundary movement during indentations near grain boundaries was observed. This suggests that grain boundary movement could be a significant deformation mechanism in nanoscale metallic thin films.

Section 3.3 discussed the influence of the substrate on the indentation response of thin film/substrate systems where the films were harder than the substrate. In the case of the amorphous diamond on silicon, a localized plastic zone resulted in the silicon substrate and a dimple resulted in the a-D film. Importantly, the a-D film did not fracture or spall off from the substrate. With the intention of using the a-D film as a protective coating for MEMS devices, the *in situ* nanoindentation experiments provided direct evidence of the superior strength and adhesion of these films. A micromachined device coated with an a-D film can be expected to retain its superior mechanical and chemical properties even after the application of a large and highly localized stress.

During the deformation of the epitaxial TiN on MgO (001), both the film and substrate deformed through dislocation plasticity. In the MgO substrate, dislocations nucleated at the film/substrate interface and flowed laterally. This lateral deformation in the MgO substrate was accommodated by the bending of the TiN film, as evidenced by the diffuse tilt boundary. Even in the case of hard films on softer substrates, there exist significant differences in the microstructural response of the indented materials. When the deformation in the substrate is localized, as was observed in the a-D on Si samples, the film dimples. When the deformation of the substrate is diffuse, as was observed in the epitaxial TiN/MgO samples, the film bends. While substrate effects are inferred from load vs. displacement data obtained with conventional indentation techniques, the underlying mechanisms are often unknown. *In situ* nanoindentation in a TEM can provide the direct observations of the evolution of plasticity needed to resolve the mechanisms associated with the substrate effect.

In conclusion, the new experimental technique of *in situ* nanoindentation technique in a TEM has been shown to provide a unique capability for investigating the nanomechanical behavior of small solid volumes. This capability is essential to fully understanding the mechanisms associated with indentation phenomena and the fundamental deformation behavior of materials.

[1] J.B. Pethica, R. Hutchings and W.C. Oliver," Hardness measurement at penetration depths as small as 20 nm", *Phil. Mag. A*, **48** 593 (1983).

[2] W.C. Oliver and G.M. Pharr, "An improved technique for determining hardness and elastic modulus using load and displacement sensing indentation experiments", *J. Mater. Res.* **7**, 1564 (1992).

[5] A. Gouldstone, H.-J. Koh, K.-Y. Zeng, A.E. Giannakopoulos, and S. Suresh," Discrete and continuous deformation during nanoindentation of thin films", *Acta Mater.*, **48** p2277 (2000).

[4] Gerberich, W. W., Nelson, J. C., Lilleodden, E. T., Anderson, P., and Wyrobek, J. T., "Indentation induced dislocation nucleation: the initial yield point", *Acta Mater.*, **44** 3585 (1996).

[5] V. Domnich, Y. Gogotsi, and S. Dub, "Effect of Phase Transformations on the Shape of the Unloading Curve in the Nanoindentation of Silicon," *Appl. Phys. Lett.* **76** 2214-2216 (2000)

[6] e.g., *Nanoindenter XP*, MTS Corp., Minneapolis, MN.

[7] D. Tabor, Hardness of Metals, Clarendon Press, Oxford, United Kingdom, 1951

[8] P.A. Flinn, D.S. Gardner, and W.D. Nix, "Measurement and interpretation of stress in aluminum-based metallization as a function of thermal history", *IEEE Trans. Electr. Dev.*, **34** (1987), p.689

[9] R. Keller, S.P. Baker, and E. Artz, "Quantitative analysis of strengthening mechanisms in thin Cu films: effects of film thickness, grain size, and passivation", *J. Mater. Res.*, 13 (1998) p. 1307

[10] Javaraman, S.; Edwards, R.L.; Hemker, K.J.(Edited by: Cammarata, R.C.; Nastasi, M.; Busso, E.P.; Oliver, W.C.) "Determination of the mechanical properties of polysilicon thin films using bulge testing" (Thin-Films -Stresses and Mechanical Properties VII. Symposium, MRS Fall Meeting, Boston, MA, USA, 1-5 Dec. 1997.) Warrendale, PA, USA: Mater. Res. Soc, 1998. p.623-8

[11] Paviot, V.M.; Vlassak, J.J.; Nix, W.D.(Edited by: Baker, S.P.; Ross, C.A.; Townsend, P.H.; Volkert, C.A.; Borgesen, P.) Measuring the mechanical properties of thin metal films by means of bulge testing of micromachined windows (Thin Films: Stresses and Mechanical Properties V. Symposium, MRS Fall Meeting, Boston, MA, USA, 28 Nov.-2 Dec. 1994.) Pittsburgh, PA, USA: Mater. Res. Soc, 1995. p.579-84.

[12] T.P. Weihs, S. Hong, J.C. Bravman, and W.D. Nix, "Mechanical deflection of cantilever microbeams: a new technique for testing the mechanical properties of thin films", *J. Mater. Res.*, **3** (1988) p. 931

[13] Hemker, K.J.; Last, H. Microsample tensile testing of LIGA nickel for MEMS applications. Materials Science & Engineering A (Structural Materials: Properties, Microstructure and Processing), vol.A319-321, (12th International Conference on the Strength of Materials. ICSMA - 12, Asilomar, CA, USA, 27 Aug.-1 Sept. 2000.) Elsevier, Dec. 2001. p.882-6

[14] Muhlstein, C.L.; Stach, E.A.; Ritchie, R.O. "Mechanism of fatigue in micron-scale films of polycrystalline silicon for microelectromechanical systems" *Appl. Phys Lett.*.**80**, p.1532-4 (2002)

[15] K.L. Johnson, *Contact Mechanics*, 2nd edn, Cambridge Univ. Press, Cambridge (1987)

[16] Corcoran, S.G.; Colton, R.J.; Lilleodden, E.T.; Gerberich, W.W.(Edited by: Gerberich, W.W.; Gao, H.; Sundgren, J.-E.; Baker, S.P.) Nanoindentation studies of yield point phenomena on gold single crystals (Thin Films: Stresses and Mechanical Properties VI. Symposium, MRS Spring Meeting, San Francisco, CA, USA, 8-12 April 1996.) Pittsburgh, PA, USA: Mater. Res. Soc, (1997) p.159-64

[17] W.W. Gerberich, J.C. Nelson, E.T. Lilleodden, P.Anderson and J.T. Wyrobek, "Indentation induced dislocation nucleation: the initial yield point", *Acta Mater.* **44** (1996), p. 3585

[18] P. Tangyunyong, R.C. Thomas, J.E. Houston, T.A. Michalske, R.M. Crooks, and A.J. Howard, "Nanometer-scale mechanics of gold films", *Phys. Rev. Lett.*,**71** (1993) p. 3319

[19] J.B. Pethica and W.C. Oliver, "Mechanical properties of nanometer volumes of material:use of the elastic response of small area indentations", in the Proceedings from the Materials Research Society: Thin Films: Stresses and Mechanical Properties, vol 130 (1989) p. 13

[20] W.W. Gerberich, D.E. Kramer, N. I. Tymiak, A. A. Volinsky, D. F. Bahr and M. D. Kriese, "Nanoindentation-induced defect-interface interactions: phenomena, methods and limitations" *Acta Mater.* **47** , 4115 (1999).

[21] V. Domnich and Y. Gogotsi ,"Phase Transformations in silicon under contact loading" *Rev.Adv.Mater.Sci.* **3** (2002) p.1-36

[22] Gogotsi, Y.G.; Domnich, V.; Dub, S.N.; Kailer, A.; Nickel, K.G. "Cyclic nanoindentation and Raman microspectroscopy study of phase transformations in semiconductors", *J. Mat. Res.*, **15**, (2000) p.871-9

[23] Z.C. Li, L. Liu, X. Wu, L.L. He, Y.B. Xu, "Indentation induced amorphization in gallium arsenide" *Mat Sci and Eng A*, 337 (2002) p. 21-24

[24] Krenn, C.R.; Roundy, D.; Cohen, M.L.; Chrzan, D.C.; Morris, J.W. "Connecting atomistic and experimental estimates of ideal strength". *Physical Review B* **65**, p.134111/1-4 (2002)

[25] J.P. Hirth, and J. Lothe, *Theory of Dislocations*, McGraw-Hill, New York, NY (1968)

[26] J.W. Morris, Jr., C.R. Krenn, D. Roundy, and M.L. Cohen, "Elastic Stability and the Limit of Strength," (Proceedings of Symposium, Phase Transformations and Evolution in Materials. Proceedings of Symposium,TMS Annual Meeting, Nashville, TN, USA, 12-16 March 2000.) Warrendale, PA, USA: (2000). p.187-207

[27] M. Wall, and U. Dahmen, *Microscopy and Microanalysis* 3, 593 (1997).

[28]Amiga™ graphics computer, AMIGA, Inc., 34935 SE Douglas Street, Suite 210, Snoqualmie, WA 98065 (USA)

[29] T. Sung, G. Popovici, M.A. Prelas, R.G.Wilson and S.K. Loyalka, "Boron diffusion into diamond under electric bias", *J. Mater. Res.*, **12** (1997) p. 1169-1171

[30] G. Popovici, R.G. Wilson, T. Sung, M.A. Prelas and S. Khasawinah, "Diffusion of boron, lithium, oxygen, hydrogen and nitrogen in type IIa natural diamond", *J. Appl. Phys.* **77**, (1995) pp. 5103-5106

[31] H. Seidel, L. Csepregi, A. Heuberger and H. Baumgartel, "Anisotropic Etching of Crystalline Silicon in Alkaline Solutions", *J. Electrochemical Soc.* **137** (1990) pp 3612-3632

[32] J. Fruhauf and B. Hannemann, "Wet etching of undercut sidewalls in {001} –silicon" *Sensors and Actuators* **79** (2000) 55-63

[33] G. Badenes, R. Rooyackers, S.K. Jones, D. Bazley, R. Beanland, I. De Wolf, I.an d L.Deferm, "Optimization of polysilicon encapsulated local oxidation of silicon. Cavity dimension effects on mechanical stress and gate oxide integrity". *Journal of the Electrochemical Society*,**145**, (1998). p.1653-9.

[34] C. Keller, private communication, 2000

[35] Alexander, H. and Haasen, P., "Dislocations and plastic flow in the diamond structure". *Solid State Phys.* **22** (1968) p. 27-158.

[36] Sumino, K., Mechanical Properties of Semiconductors. in *HANDBOOK ON SEMICONDUCTORS*. Elsevier, Scientific Press. New York. (1994) p.73-181.

[37] N.I. Kato, A. Nishikawa, H. Saka, "Dislocations in Si generated by fatigue at room temperature" *Mat. Sci. Semicond. Proc.* **4** (2001) p. 113-115.

[38] Lawn, B.R., *FRACTURE OF BRITTLE SOLIDS, SECOND EDITION.* Cambridge University Press. New York (1993).

[39] M.J. Hill, and D.J. Rowcliffe, "Deformation of silicon at low temperature". *J. Mater. Sci.* 9 (1974) p. 1569-76.

[40] G.M. Pharr, W.C. Oliver, and D.S. Harding, "New evidence for a pressure-induced phase transformation during the indentation of silicon". *J. Mater. Res.* **6** (1991) p. 1129-30.

[41] Weppelmann, E.R., Field, J.S. and Swain, M.V., "Observation, analysis, and simulation of the hysteresis of silicon using ultra-micro-indentation with spherical indenters." *J. Mater. Res.,* **8** (1993) p. 830-40.

[42] Mann, A.B., van Heerden, D., Pethica, J.B. and Weihs, T.P.," Size-dependent phase transformations during point loading of silicon". *J.Mater. Res.* **15** (2000) p. 1754-58.

[43] Li, X. Diao, D. and Bhushan, B., "Fracure mechanisms of thin amorphous carbon films in nanoindentation", *Acta Mater.* **45** (1997) p. 4453-61.

[44] Armstrong, R.W., Ruff, A.W. and Shin, H., Elastic, plastic and cracking indentation behavior of silicon crystals. *Mat. Sci. and Eng. A* **209** (1996) p. 91-96.

[45] Callahan, D.C. and Morris, J.C., The extent of phase transformation in silicon hardness indentations. *J. Mater. Res.* **7** (1992) p. 1614-17.

[46] Leipner, H.S., Lorenz, D., Zeckzer, A., Lei, H. and Grau, P., "Nanoindentation pop-in effect in semiconductors", *Physica B* **308** (2001) p. 446-9.

[47] Stach, E.A, et.al., "Development of a nanoindenter for in situ transmission electron microscopy". *Micr. and Microanal.* **7** (2001) p.507-17.

[48] Minor, A.M., Morris, J.W. and Stach, E.A., "Quantitative in situ nanoindentation in an electron microscope". *Appl. Phys. Let.* **79** (2001) p. 1625-7.

[49] Page, T.F., Oliver, W.C., and McHargue, C.J., "The deformation behavior of ceramic crystals subjected to very low load (nano)indentations". *J. Mater. Res.*, **7** (1992) p. 450-73.

[50] Wentorf, R.H. and Kasper, J.S., "Two new forms of silicon", *Science* **139** (1963) p. 338-9.

[51] Jamieson, J.C., "Crystal structures at high pressures of metallic modifications of silicon and germanium", *Science* **139** (1963) p. 762-4.

[52] Pilz, R.O., Maclean, J.R., Clark, S.J., Ackland, G.J., Hatton, P.D. and Crain, J., "Structure and properties of silicon XII: A complex tetrahedrally bonded phase" *Phys. Rev. B* **52** (1995) p.4072-85.

[53] Pfrommer, B.G., Cote, M., Louie, S.G. and Cohen, M.L., "Ab initio study of silicon in the R8 phase" *Phys. Rev. B* **56** (1997) p. 6662-68.

[54] C.L. Kelchner, S.J. Plimpton and J.C. Hamilton," Dislocation nucleation and defect structure during surface indentation", *Phys. Rev. B* **58**, 11085 (1998).

[55] M.C. Fivel, C.F. Robertson, G.R. Canova and L. Boulanger, "Three-dimensional modeling of indent-induced plastic zone at a mesoscale" *Acta Mater.* **46**, 6183 (1998).

[56] W.L. Bell and G. Thomas, "Contrast from Large Prismatic Dislocation Loops", *Phil. Mag.*, **13**, p.395 (1966)

[57] E.T. Lilleodden, Ph.D. thesis, Stanford University (2001)

[58] D.F. Bahr, D.E. Kramer and W.W. Gerberich, "Non-linear deformation mechanisms during nanoindentation", *Acta Mater.* **46**, 3605 (1998).

[59] E.T. Lilleodden and W.D. Nix, submitted to *Phys. Rev. B* (2002).

[60] S. G. Cocoran, R.J. Colton, E.T. Lilleodden and W.W. Gerberich, "Anomalous plastic deformation at surfaces: nanoindentation of gold single crystals" *Phys Rev B.*, **55** R16057 (1997)

[61] E.O. Hall, "The deformation and aging of mild steel: discussion and results", *Proc. Phys, Soc. London,* **B64** (1951) p.747

[62] N.J. Petch, "The cleavage strength of polycrystals", *J. Iron Steel Inst.*, **174** (1953) p. 25

[63] J.C.M. Li, "Petch relation and grain boundary sources", *Trans. Metall. Soc. AIME,* **227** (1963) p. 239

[64] E.T. Lilleodden, J.A. Zimmerman, S.M. Foiles and W.D. Nix "Atomistic Simulations of Elastic Deformation and Dislocation Nucleation During Nanoindentation", *J. Mech. Phys. Solids*, in press (2002)

[65] D. Gruen, "Nanocrystalline Diamond Films", *Annu. Rev. Mater. Sci.*, **29** (1999) p. 211-259

[66] T. Langdon, "The physics of superplastic deformation", *Mat. Sci.Eng. A* **137** (1992) 1-11

[67] T. Langdon, "The mechanical properties of superplastic materials", *Met. Trans. A* **B13A** (1982) pp.689-700

[68] M. Winning, G. Gottstein, and L.S. Shvindlerman, "Stress Induced Grain Boundary Motion" *Acta mater.* **49** (2001) 211–219

[69] K.L Merkle, L.J. Thompson, "Atomic Scale observation of grain boundary motion", *Materials Letters* **48** (2001) 188–193

[70] R. Saha and W.D. Nix, "Effets of the substrate on the determination of thin film mechanical properties by nanoindentation", *Acta Mat* **50** (2002) 23-38

[71] T. A. Friedmann, M. P. Siegal, D. R. Tallant, R. L. Simpson, and F. Dominguez, (Edited by: Renschler, C.L.; Cox, D.M.; Pouch, J.J.; Achiba, Y.) "Residual stress and Raman spectra of laser deposited highly tetrahedral-coordinated amorphous carbon films "(Novel Forms of Carbon II Symposium, MRS Spring Meeting, San Francisco, CA, USA, 4-8 April 1994.) Pittsburgh, PA, USA: Mater. Res. Soc, 1994. p. 501.

[72] Siegal, M.P.; Friedmann, T.A.; Kurtz, S.R.; Tallant, D.R.; Simpson, R.L.; Dominguez, F.; McCarty, F.F. (Edited by: Renschler, C.L.; Cox, D.M.; Pouch, J.J.; Achiba, Y.) "Structural and electrical characterization of highly tetrahedral-coordinated diamond-like carbon films grown by pulsed-laser deposition" (Novel Forms of Carbon II Symposium, MRS Spring Meeting, San Francisco, CA, USA, 4-8 April 1994.) Pittsburgh, PA, USA: Mater. Res. Soc, 1994. p.507-12

[73] Y. Lifshitz, S. R. Kasi, and J. W. Rabalais, "Subplantation model for film growth from hyperthermal species: application to diamond." *Phys. Rev. Lett.* **62**, 1290 (1989)

[74] T. A. Friedmann, J. P. Sullivan, J. A. Knapp, D. R. Tallant, D. M. Follstaedt, D. L. Medlin and P. B. Mirkarimi "Thick stress-free amorphous-tetrahedral carbon films with hardness near that of diamond" *Appl Phys Lett*, 71 (26), 1997 p. 3820

[75] J.E. Sundgren, A. Rockett, and J.E. Greene, "Microstructural and Microchemical Characterization of Hard Coatings," *J. Vac. Sci. Technol. A.,* 6 2770-2783 (1986)

[76] Krenn, C.R.; Morris, J.W., Jr.; Seung-Hoon Jhi; Jisoon Ihm (Edited by: Kumar, A.; Chung, Y.-W.; Chia, R.W.J.) "Relationships between atomistic bonding and intrinsic macroscopic hardness". Hard Coatings. Based on Borides, Carbides and Nitrides: Synthesis, Characterization and Applications. Proceedings of the International

Symposium held at the 1998 TMS Annual Meeting, San Antonio, TX, USA, 16-19 Feb. 1998.) Warrendale, PA, USA: TMS, 1998. p.379-88.

[77] W.S. Williams, "Influence of Temperature, Strain Rate, Surface Condition, and Composition on the Plasticity of Transition-Metal Carbide Crystals," *J. Appl. Phys.*, **35**, 1329-1338 (1964)

[78] Jhi, S.H., Louie, S.G., Cohen, M.L., and Morris, Jr., J.W., "Mechanical instability and ideal shear strength of transition metal carbides and nitrides", *Phys. Rev. Lett.*, **87**, (2001) p.075503/1-4

[79] H. Holleck, "Material selection for hard coatings", *J. Vac. Sci. Technol. A* **4** (1986) p 2661

[80] D. Smith, Thin Film Deposition- Principles and Practice (McGraw-Hill, Inc., New York, NY) 1995

[81] J.S. Chun, I.Petrov and J.E. Greene, "Dense fully 111-textured TiN diffusion barriers: Enhanced lifetime through microstructure control during layer growth", *J. Appl. Phys* **86** (1999) pp. 3633-3641

[82] Y.-W. Kim, I. Petrov, H. Ito, and J. E. Greene, "Low-energy (5<E/sub i/<100 eV), high-brightness, ultrahigh vacuum ion source for primary ion beam deposition: Applications for Al and Ge" *J. Vac. Sci. Technol.* **A 13**, p. 2836 (1995)

[83] B.W. Karr, I. Petrov, P. Desjardins, D.G. Cahill, and J.E. Greene, *Surf. Coat. Technol.* 94-95, **403** (1997)

[84] Karr, B.W.; Petrov, I.; Cahill, D.G.; Greene, J.E. "Morphology of epitaxial TiN(001) grown by magnetron sputtering", *Appl. Phys. Lett.***70** (1997) p.1703-5.

[85] Karr, B.W.; Cahill, D.G.; Petrov, I.; Greene, J.E. "Effects of high-flux low-energy ion bombardment on the low-temperature growth morphology of TiN(001) epitaxial layers" *Phys. Rev. B* .**61** (2000). p.16137-43.

[86] Menzel, R.; Gartner, K.; Wesch, W.; Hobert, H. "Damage production in semiconductor materials by a focused Ga/sup +/ ion beam". *J.Appl.Phys.*, **88**, (2000). p.5658-61.

[87] Rubanov, S.; Munroe, P.R. "Investigation of the structure of damage layers in TEM samples prepared using a focused ion beam". *Journal of Materials Science Letters*, **20**, (2001). p.1181-3.

[88] Stanishevsky, A.; Nagaraj, B.; Melngailis, J.; Ramesh, R.;Khriachtchev, L.; McDaniel, E., "Radiation damage and its recovery in focused ion beam fabricated ferroelectric capacitors". *Journal of Applied Physics*, **92** (2002) p.3275-8.

[89] Rubanov, S.; Munroe, P.R. "Investigation of the structure ofdamage layers in TEM samples prepared using a focused ion beam".*Journal of Materials Science Letters*, **20**, (2001) p.1181-3.

[90] Hausmann, S.; Bischoff, L.; Teichert, J.Voelskow, M.; Moller, W. "Radiation damage in focused ion beam implantation" (Digest of Papers. Microprocesses and Nanotechnology '99. 1999 International Microprocesses and Nanotechnology Conference, Yokohama, Japan, 6-8 July 1999.) Tokyo, Japan: Japan Society of Applied Physics, 1999. p.146-7.

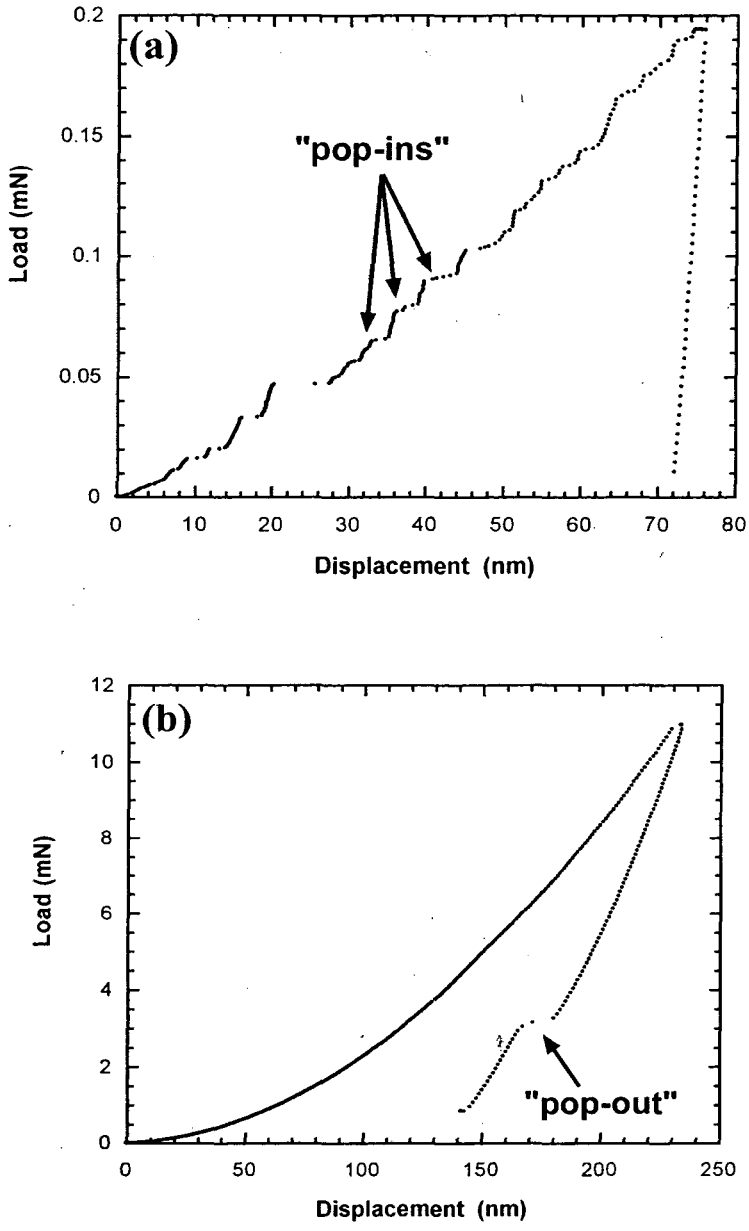

Figure 1.2.1 **(a)** Load vs. displacement nanoindentation curve from a 1 micron-thick Au film deposited onto a Si substrate. Note the discrete displacement bursts during the loading portion of the curve. **(b)** Load vs. displacement nanoindentation curve from a single crystal n-type <100> Si wafer. Note the discrete displacement burst on the unloading portion of the curve. Both data sets are courtesy of Dr. Erica Lilleodden, Lawrence Berkeley National Laboratory, Berkeley, CA (2002).

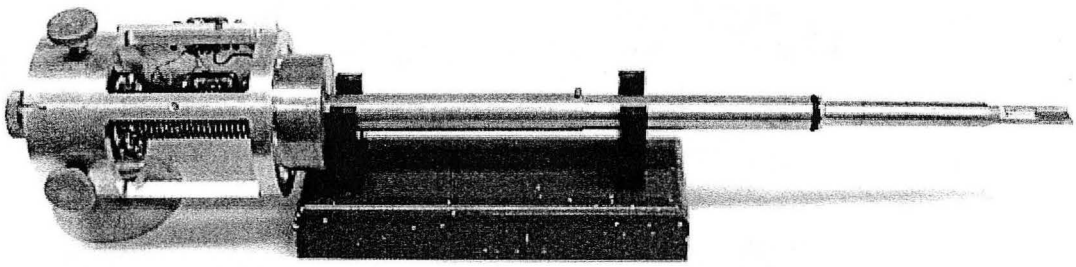

Figure 2.1.1 *In situ* nanoindentation stage for the Jeol 200 CX transmission electron microscope. The course positioning screws can be seen on the base at left, the diamond tip and sample holder are on the far right end.

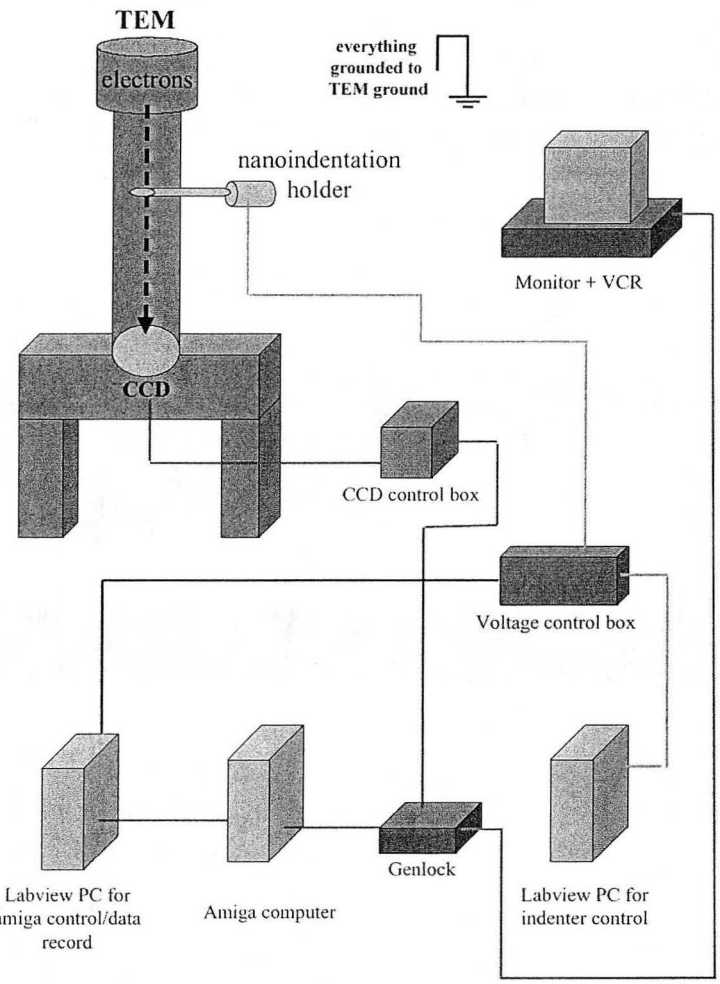

Figure 2.1.2 Schematic of *in situ* nanoindentation experimental setup.

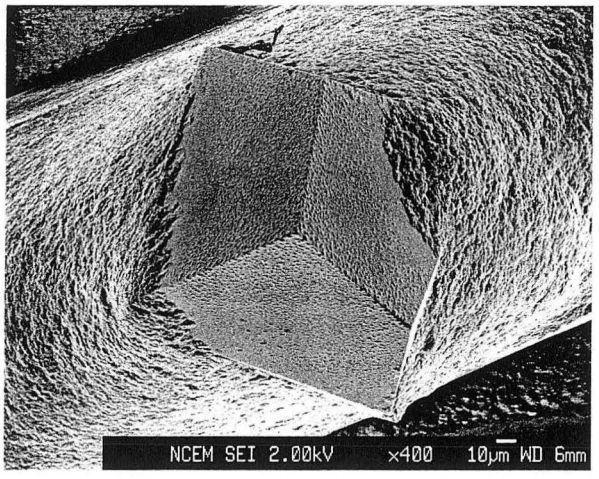

Figure 2.1.3 SEM image of original 3-sided diamond pyramid indenter. The diamond is boron-doped for conductivity and is mounted to the end of an Al rod with conductive epoxy.

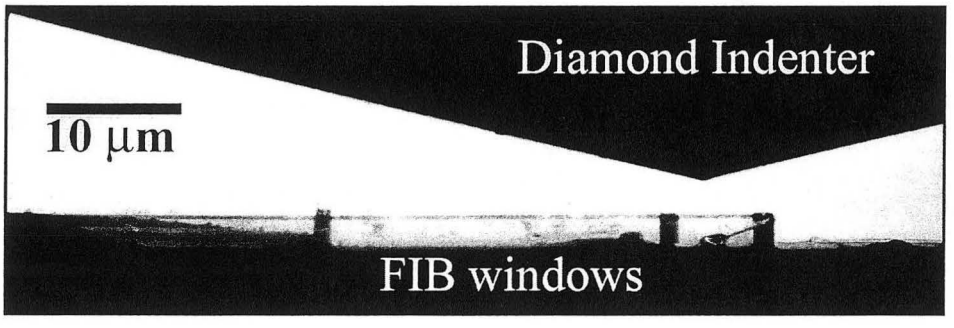

Figure 2.1.4 TEM image of the second 3 sided diamond pyramid indenter. This diamond has the Berkovich-type geometry, characterized by the large included-angle seen here.

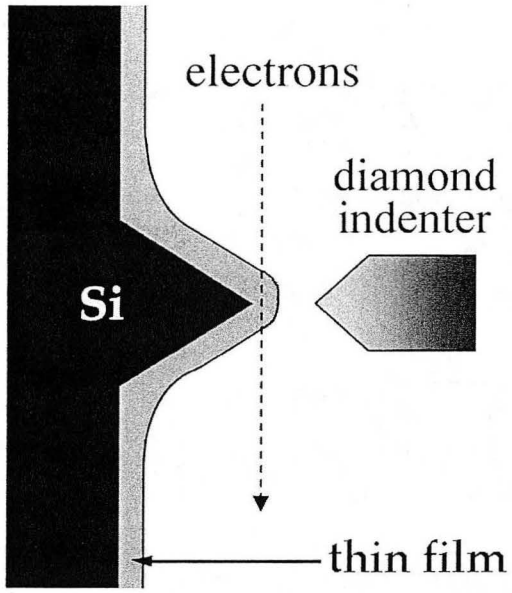

Figure 2.1.5 Schematic showing the geometric requirements for an *in situ* nanoindentation sample. The sample must have the electron transparent portion of the sample accessible to the diamond indenter in a direction normal to the electron beam.

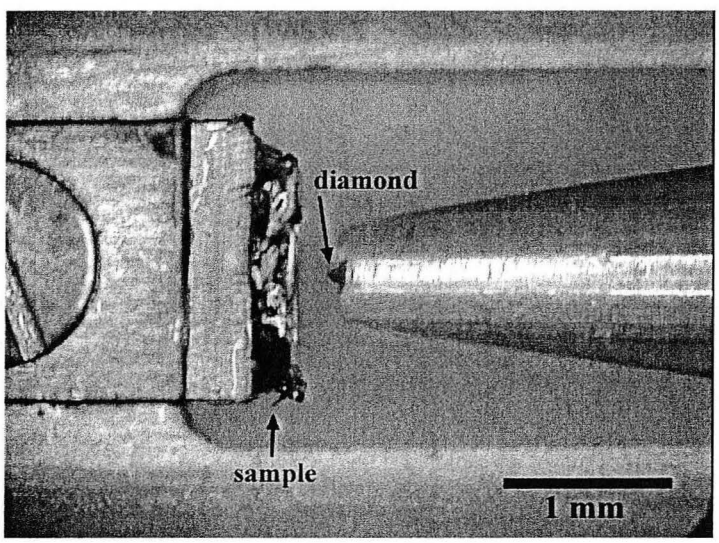

Figure 2.1.6 Image of sample loaded into the *in situ* nanoindentation stage. The diamond indenter can be seen mounted on the end of an Al rod. The details of the sample cannot be seen at this low magnification.

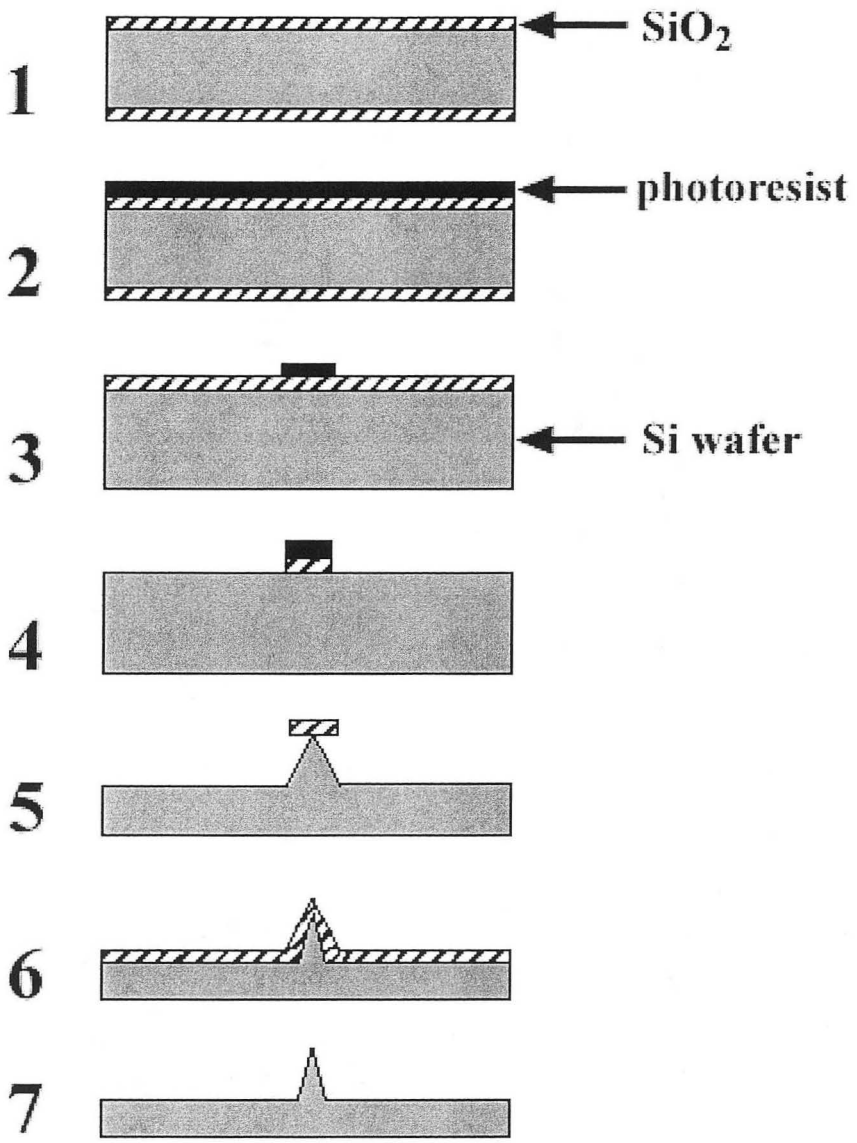

Figure 2.2.1 Cross-sectional schematic of the seven microfabrication steps used to make the silicon wedge substrates. (1) A ~1 micron SiO_2 layer is grown on a standard n-type <100> silicon wafer. (2) A thin layer of negative photoresist is spun on the wafer. (3) The photoresist is exposed using ultraviolet lithography; the exposed photoresist is removed to reveal the mask pattern. (4) The sample is immersed in HF to remove the SiO_2 except under the photoresist. (5) The sample is immersed in KOH, which anisotropically etches the silicon to form the wedge structure. (6) A SiO_2 layer is grown at low temperature to sharpen the wedge. (7) The SiO_2 layer is removed in HF yielding a wedge of silicon that is electron transparent at the peak.

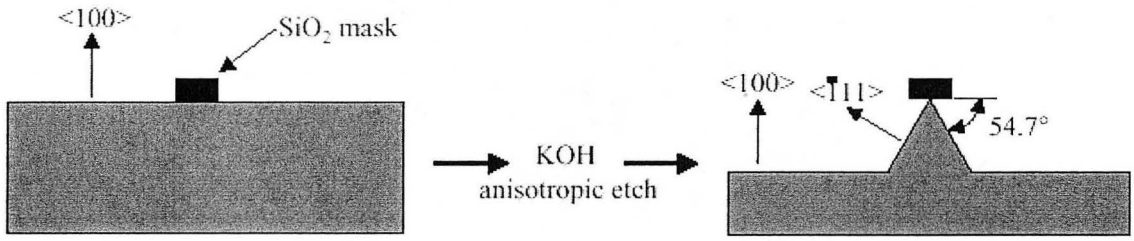

Figure 2.2.2 Shematic of the geometry associated with KOH anisotropic etch. KOH etches {111} planes of silicon slower than {100}, thus the result of etching a <100> oriented silicon wafer with a patterned line of photoresist is a wedge structure.

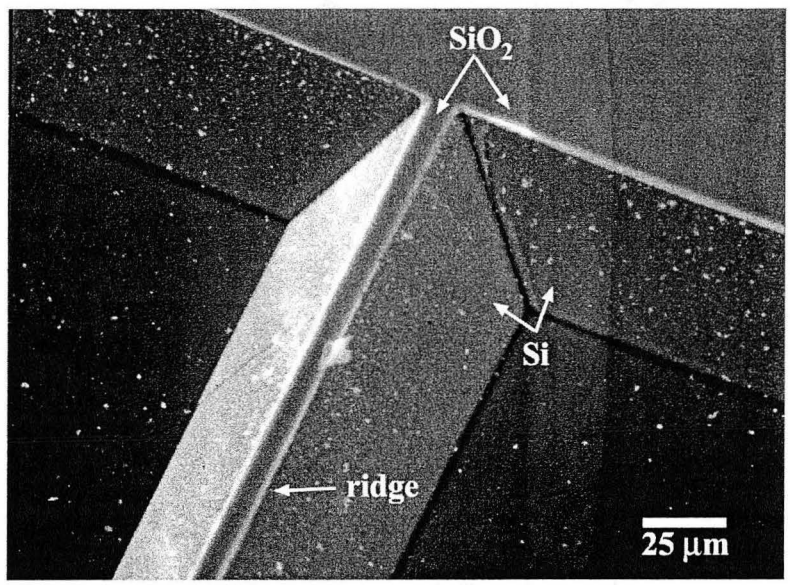

Figure 2.2.3 SEM image of silicon wedge structure after being etched in a KOH bath. The SiO_2 masking layer is still attached to the top of the structure. This corresponds to step 5 of the silicon wedge microfabrication process as described in Figure 2.2.1.

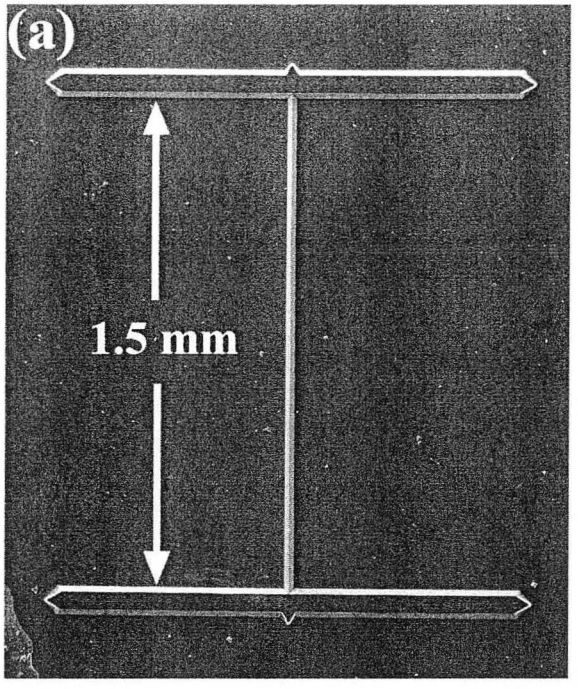

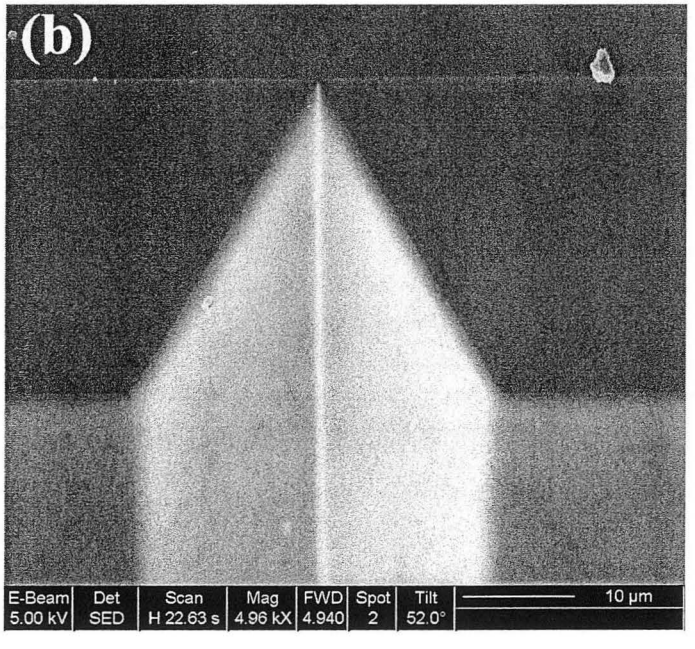

Figure 2.2.4 (a) SEM plan-view image of lithographically prepared silicon substrates. The middle bar of the structure is 1.5 mm long and the entire length is sharp enough to be electron transparent. **(b)** SEM image of the middle bar of the structure where it intersects with the side bar.

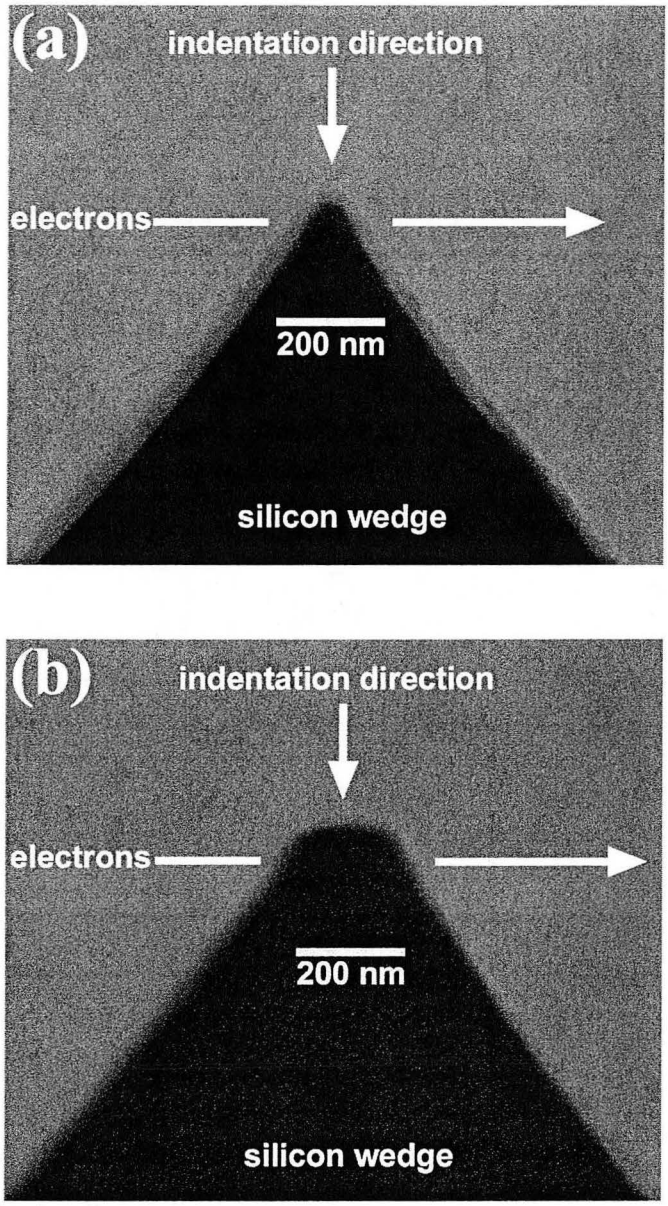

Figure 2.2.5 Scanning electron micrographs of the lithographically-prepared silicon wedge samples in cross-section. **(a)**, the blunt geometry, with a plateau of ~150 nm, and **(b)** the sharp geometry, with a plateau of ~20 nm. The cross sections were prepared with a focused ion beam after a layer of Pt was deposited for protection.

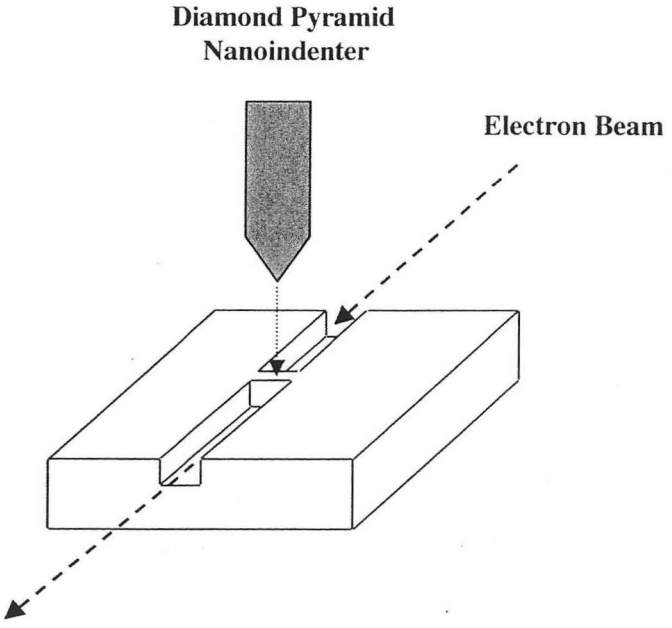

Figure 2.3.1 Schematic of the focused ion beam (FIB) sample geometry. A trench is milled out of the sample leaving behind a window thin enough to be electron transparent. The diamond indenter can approach the thin window in a direction normal to the electron beam, as shown.

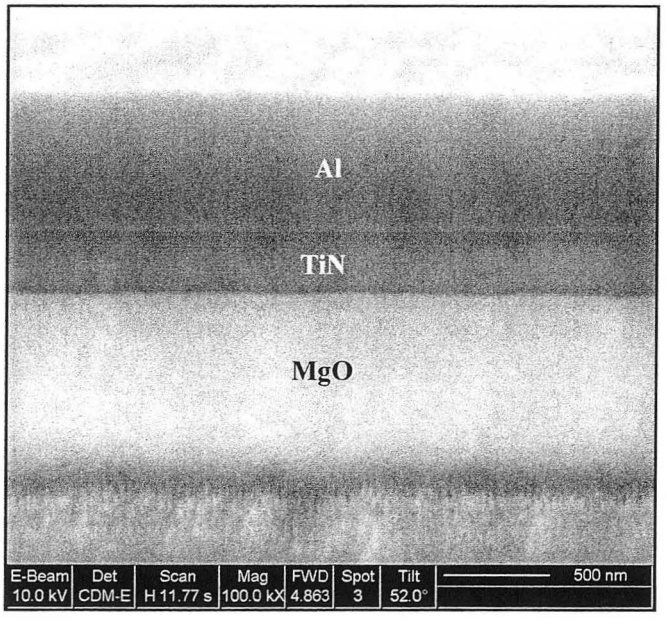

Figure 2.3.2 Cross-sectional SEM image of tri-layer structure used for samples prepared with the focused ion beam. Approximately 500 nm of Al was deposited on top of a 350 nm layer of TiN in order to protect the TiN from the incident ion beam.

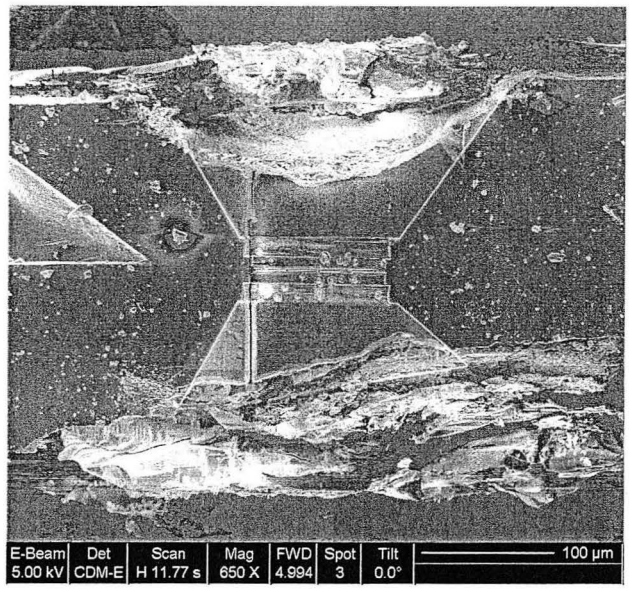

Figure 2.3.3 Plan-view SEM image of Al/TiN/MgO FIB-prepared sample. The horizontal line in the middle of the image corresponds to the electron-transparent windows.

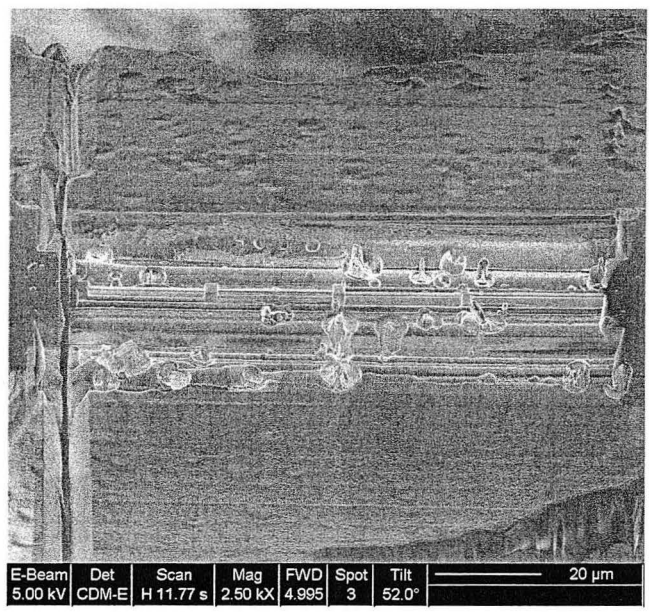

Figure 2.3.4 SEM image of FIB-prepared Al/TiN/MgO sample at a 52 degree tilt. Four electron transparent windows lie horizontally across the middle of the image.

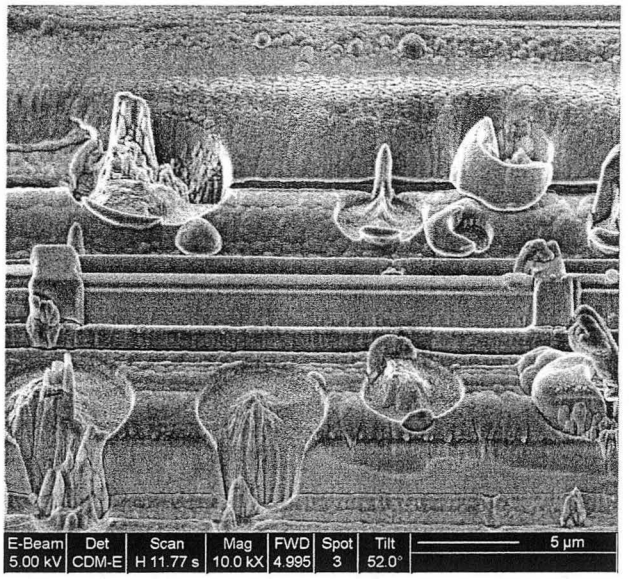

Figure 2.3.5 SEM image of FIB-prepared Al/TiN/MgO sample at a 52 degree tilt. One electron transparent window can be seen horizontally across the middle of the image. The circular craters are spots where material that had redeposited as pillars during the milling process were subsequently milled away.

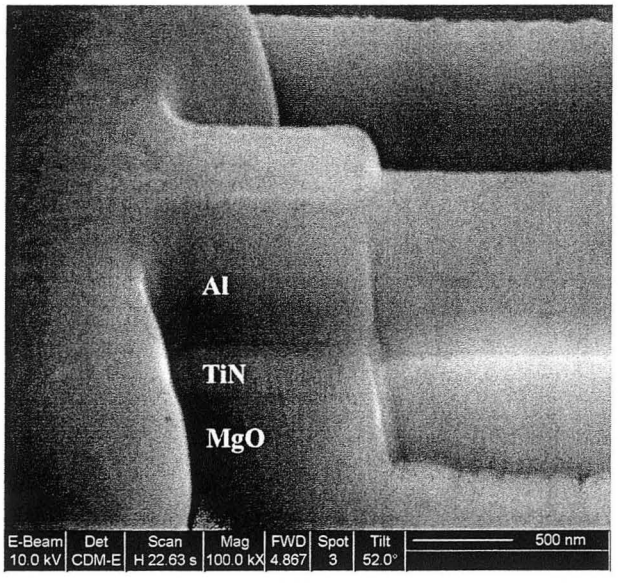

Figure 2.3.6 SEM image of FIB-prepared Al/TiN/MgO sample at a 52 degree tilt. The window is in the middle-right side of the image, and it meets the side wall in the middle of the image.

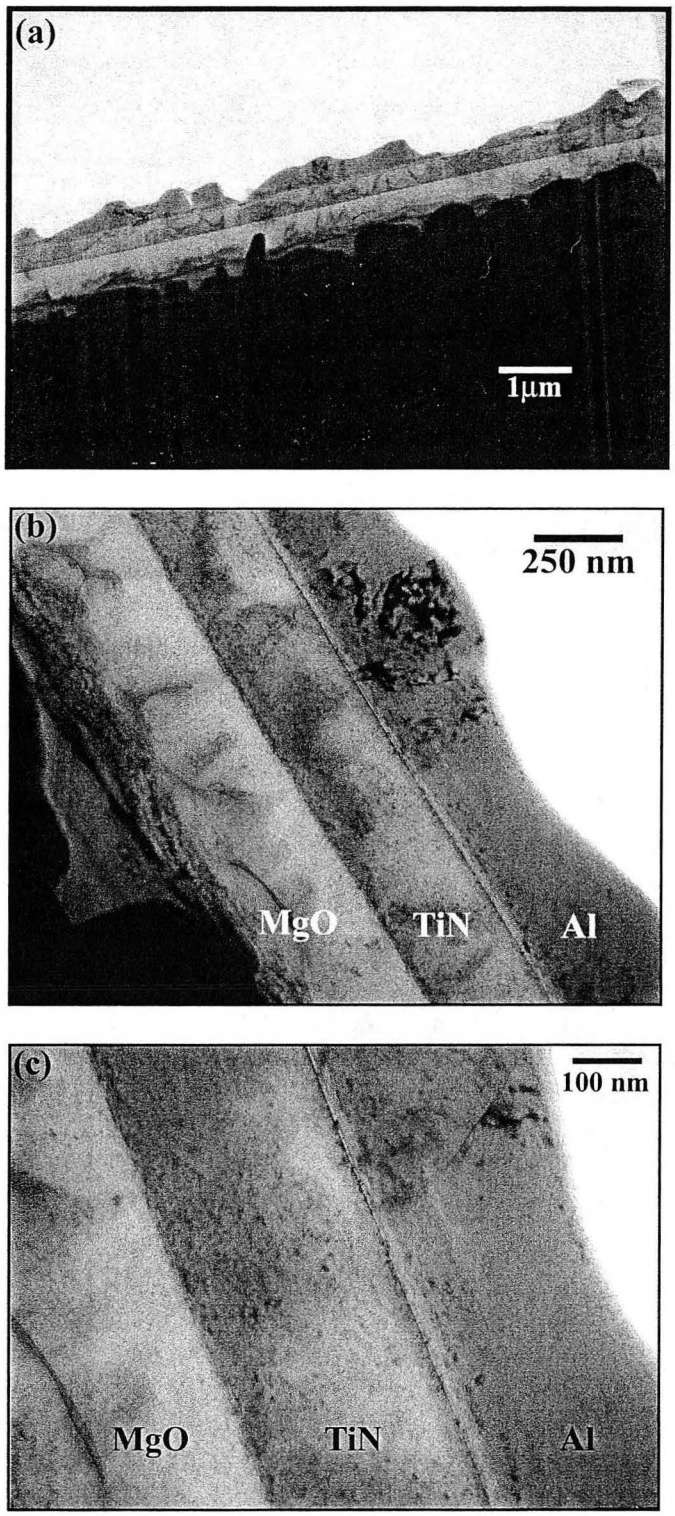

Figure 2.3.7 (a) (b) and (c) TEM images of a FIB-prepared Al/TiN/MgO sample before the Al protective layer was removed.

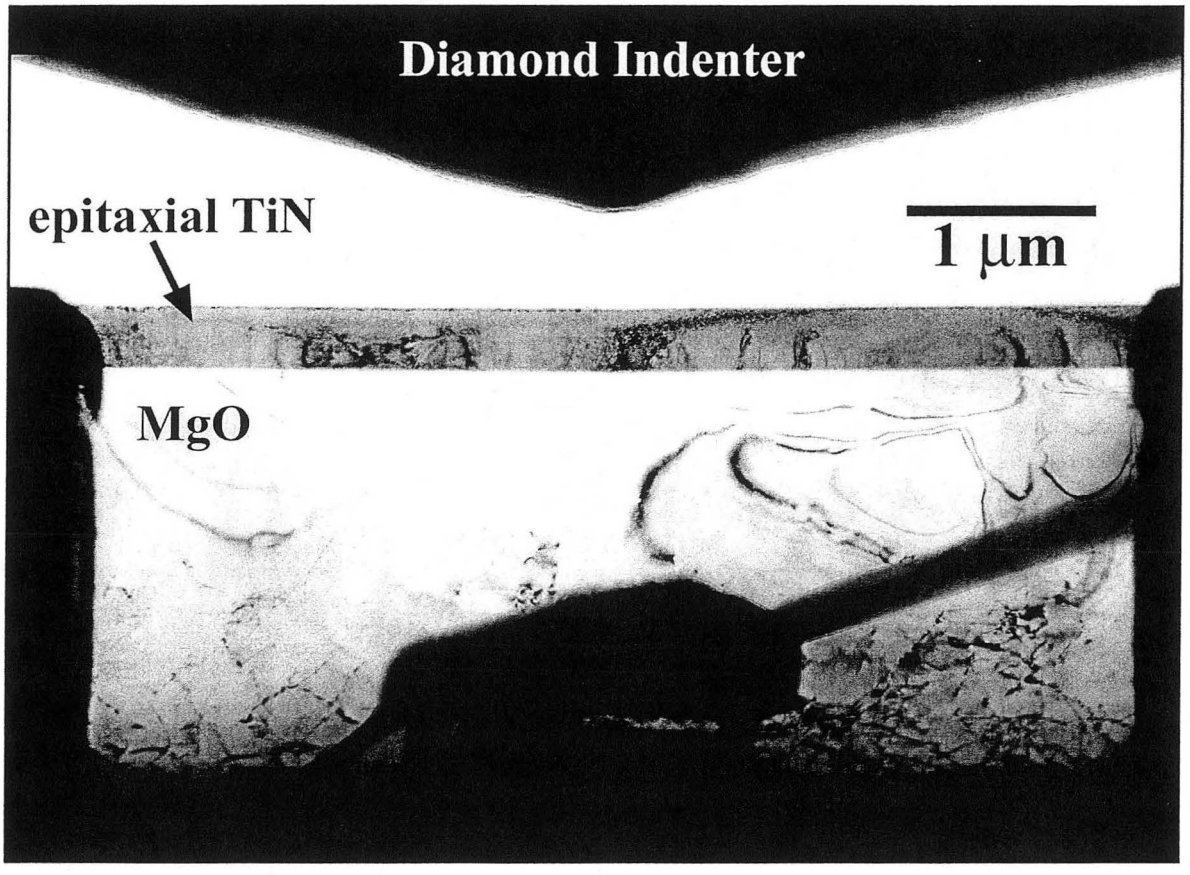

Figure 2.3.8 TEM image of an epitaxial TiN/MgO (001) sample prepared with a FIB. The protective Al layer has been removed. The Diamond indenter can be seen at the top of the image.

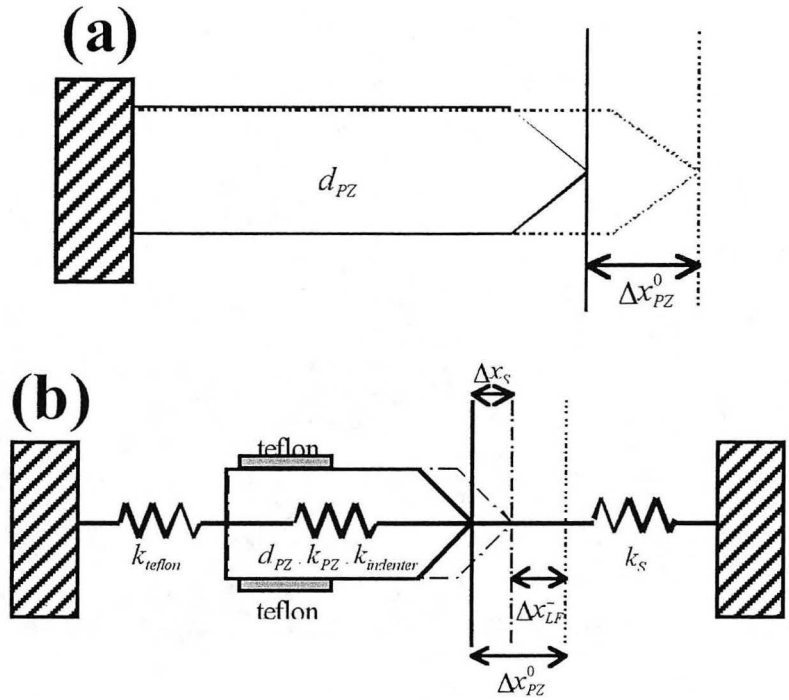

Figure 2.4.1. (a) Schematic of the displacement of the indenter assembly with no sample contact. The solid line indicates the initial position of the assembly: $V^{app}=0$, $F^{app}=0$; the dotted line shows the position of the assembly under the application of voltage: $V^{app}=V$, $F^{app}=0$. **(b)** Schematic description of the assembly in contact with a sample, where the various components act like springs in series. Again, the solid line is the initial position of the indenter/sample interface and the dotted line shows the position of the indenter assembly under the application of a voltage if no sample was present. The dash-dot line shows the position of the indenter/sample interface under an applied voltage and sample constraint: $V^{app}=V$, $F^{app}=F$.

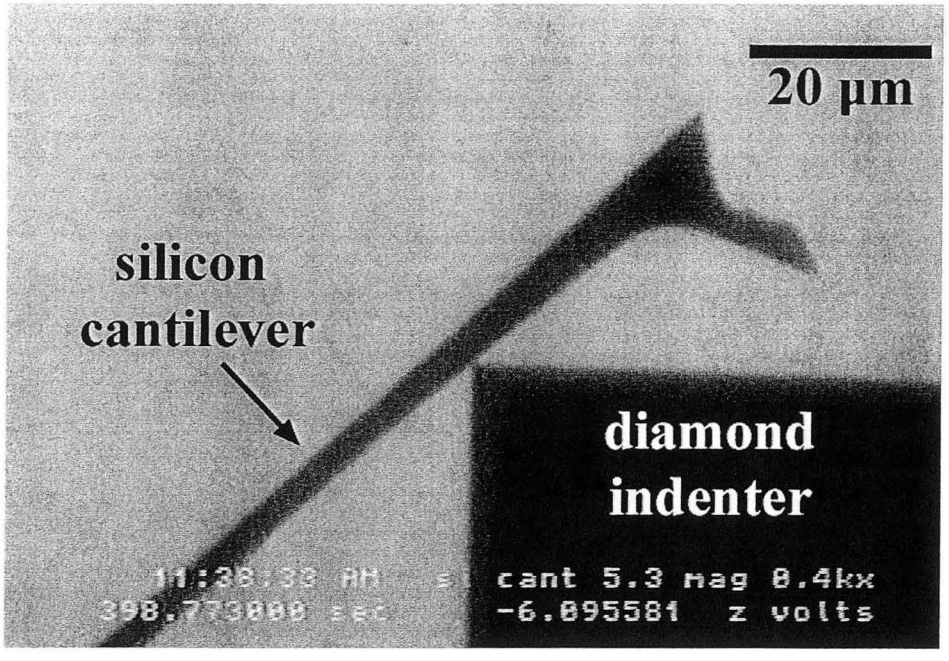

Figure 2.4.2 TEM image of the diamond indenter in contact with a single crystal silicon cantilever. The calibration constants for the load frame were determined from the unloading data of the silicon cantilever with the diamond positioned at two different places along the cantilever lever-arm.

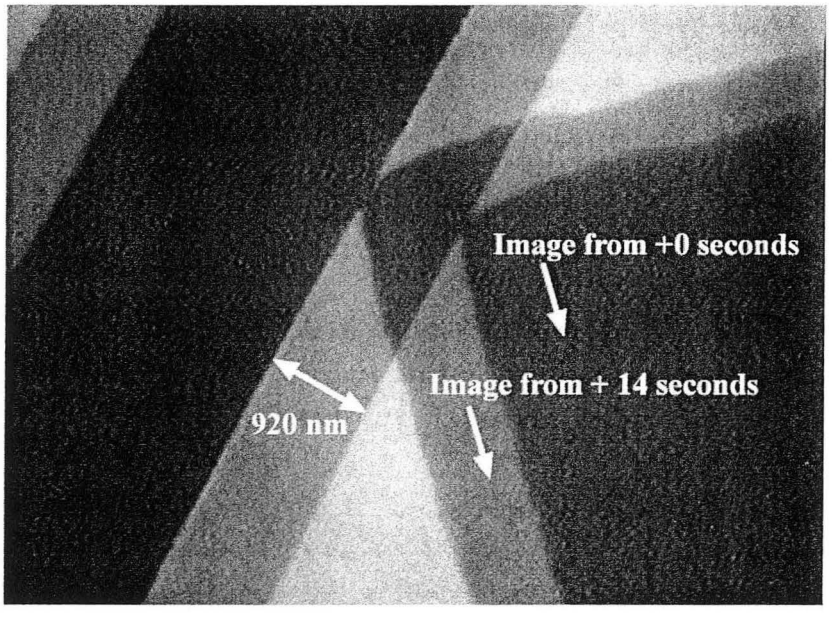

Figure 2.4.3 Superimposed *in situ* TEM images of the calibration experiment on the Si cantilever shows the displacement of the beam relative to the a reference position. The two superimposed images correspond to $\Delta x_{Si}=0$, and $\Delta x_{Si}=920$ nm.

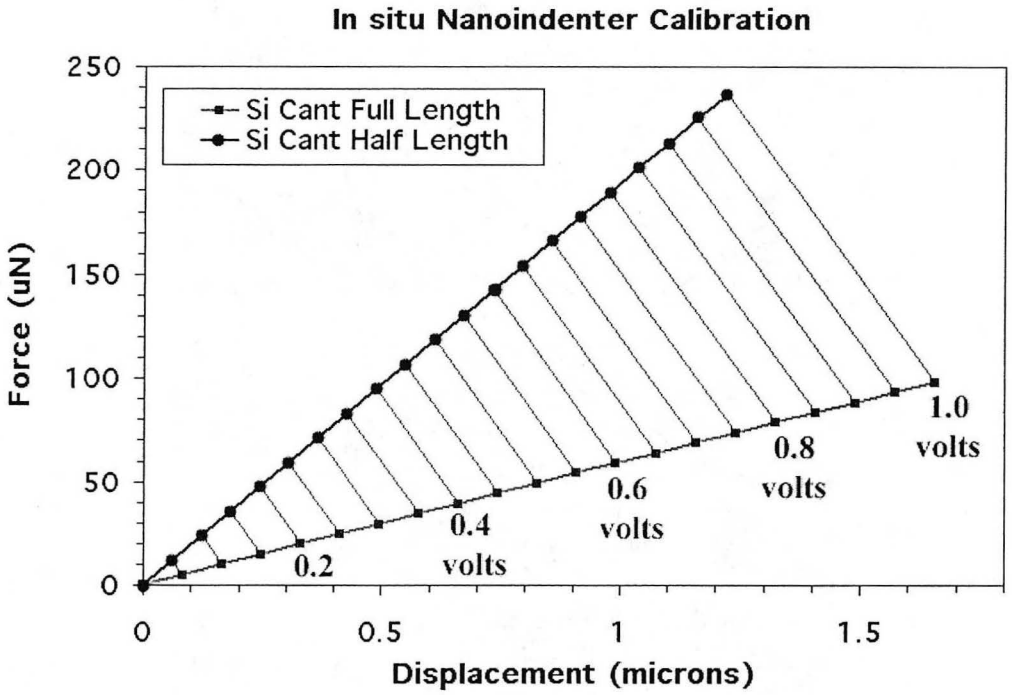

Figure 2.4.4 The results from the Si cantilever calibration experiments showing the basic relationship that for a given voltage, the force and displacement behavior of an indentation is coupled. The force applied to a sample can be determined from the voltage applied to the piezoceramic element and the displacement measured *in situ.*

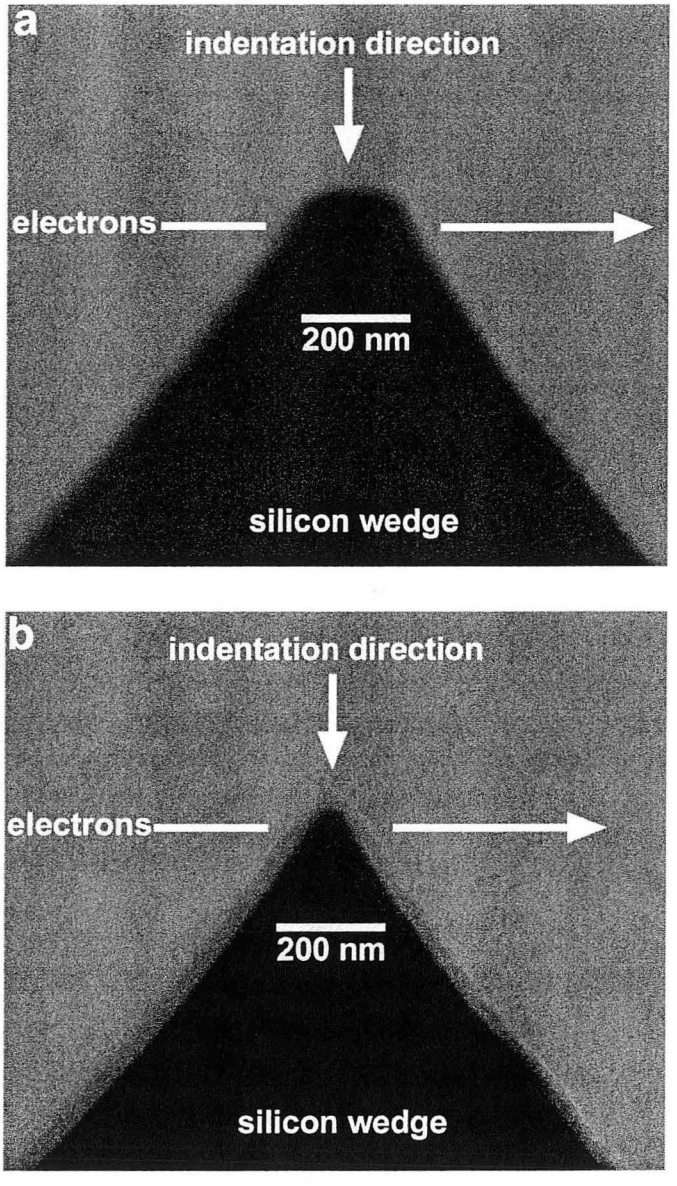

Figure 3.2.1 Scanning electron micrographs of the lithographically-prepared silicon wedge samples in cross-section. **(a)**, the blunt geometry, with a plateau of ~150 nm, and **(b)** the sharp geometry, with a plateau of ~20 nm. The cross sections were prepared with a focused ion beam after a layer of Pt was deposited for protection.

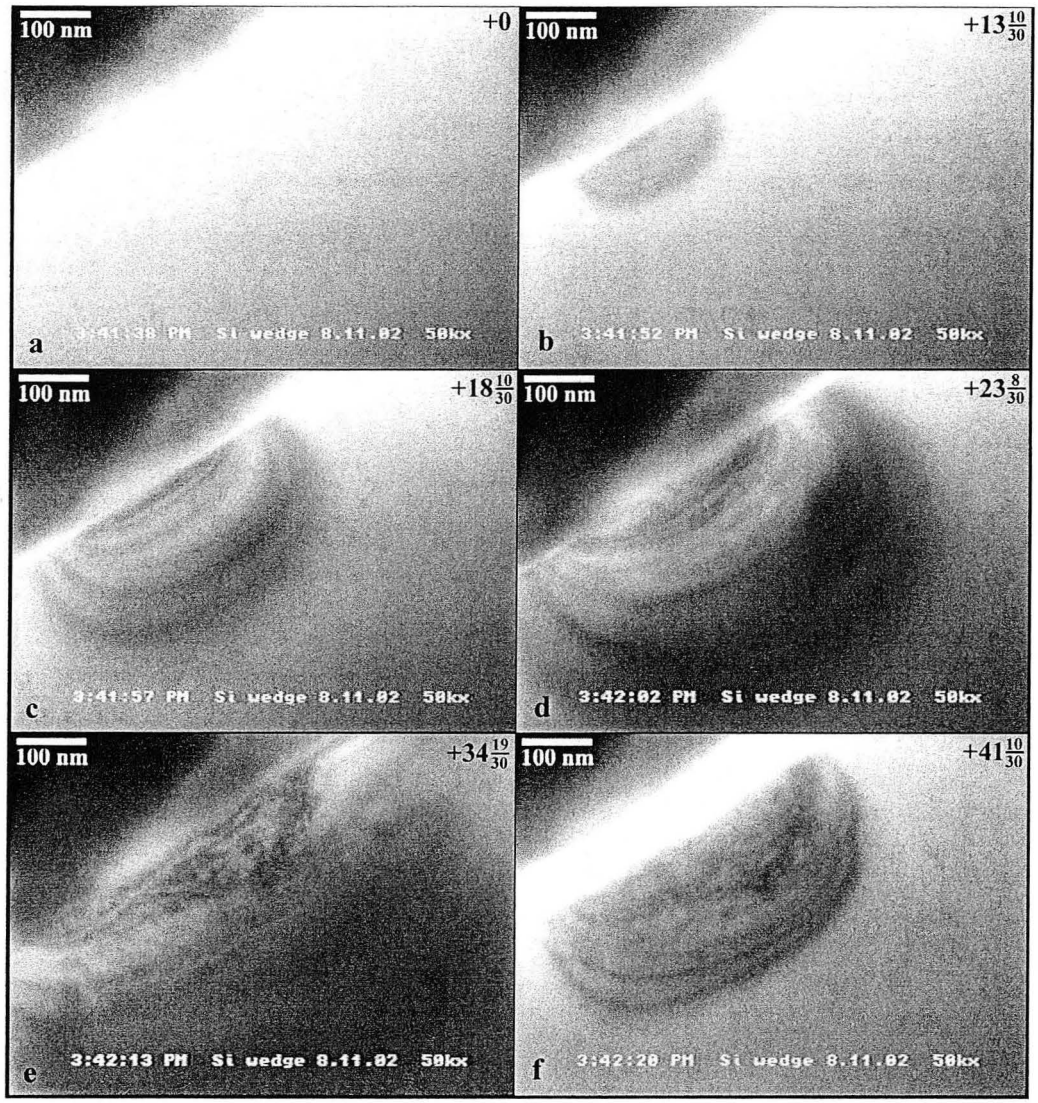

Figure 3.2.2 Time series taken from a video of an *in situ* nanoindentation into silicon <100>. The diamond indenter is in the top left corner of each frame, and the silicon sample is in the lower right. The time in seconds from the beginning of the indentation is listed in the top right corner of each frame. (a) At the start of the indentation the silicon sample is defect free. In (b) and (c) the initial portion of the indent shows elastic strain contours resulting from the pressure applied by the indenter. In (d) and (e) the dislocations can be seen to nucleate and react as the indentation proceeds. (f) After a peak depth of 54 nm the indenter is withdrawn and the residual deformed region can be seen to consist of dislocations and strain contours which are permanently frozen in the silicon wedge. Diffraction analysis (not shown here) shows the plastically deformed region to be diamond cubic silicon.

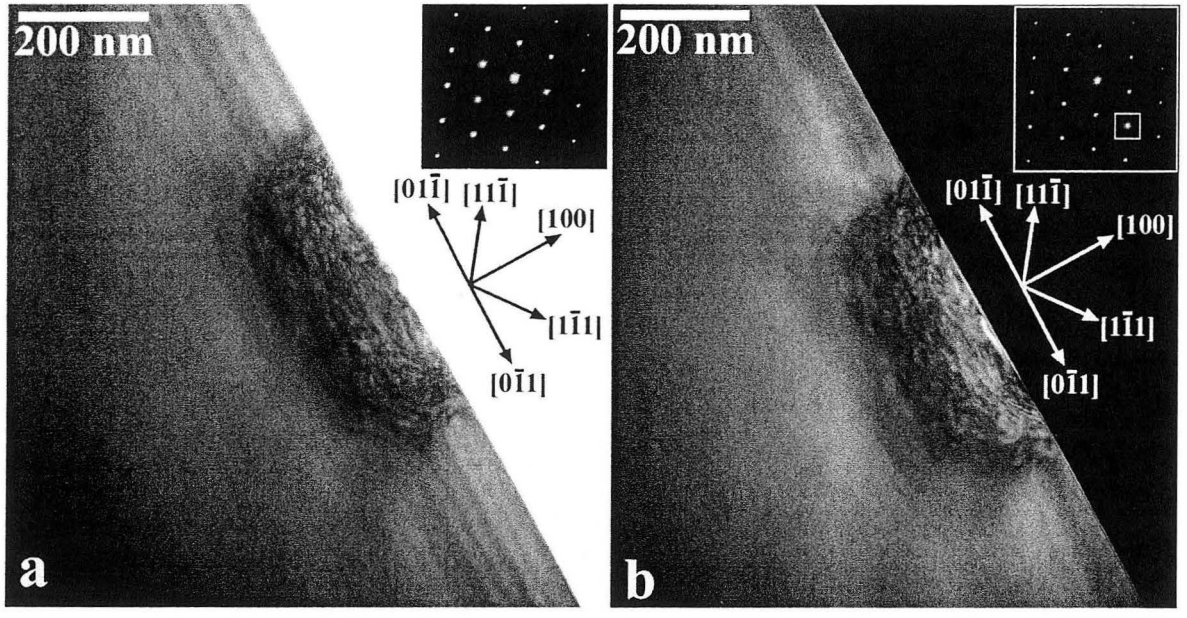

Figure 3.2.3 (a) TEM micrograph of the same indentation shown in Figure 3.2.2. The indentation is shown in the [011] zone axis condition with the corresponding diffraction pattern inset. The stripes along the length of the sample are thickness contours resulting from the wedge-shaped geometry of the specimen. The deformed region consists entirely of dislocations and no additional phase regions. **(b)** The same indentation in a g=(0-22) dark field condition. The (0-22) diffraction spot used for imaging is noted with a box in the corresponding diffraction pattern. Note the continuous surface across the indented region, indicating that the indentation left at least one side of the wedge intact.

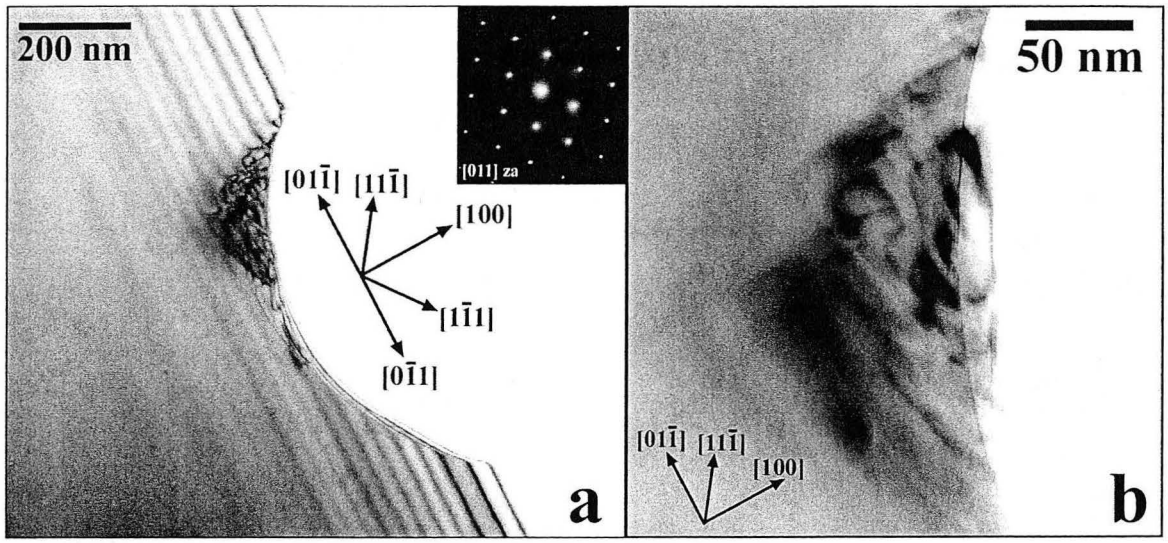

Figure 3.2.4 (a) Bright field TEM micrograph after an indentation of the sharp wedge geometry. The image was taken in the [011] zone axis condition with the corresponding diffraction pattern inset. The stripes along the length of the sample are thickness contours resulting from the wedge-shaped geometry of the specimen. **(b)** A higher magnification of the region showing residual dislocations adjacent to the fracture surface. The smooth fracture surface indicates non-crystallographic fracture. The image was taken in the g= [3-11] condition.

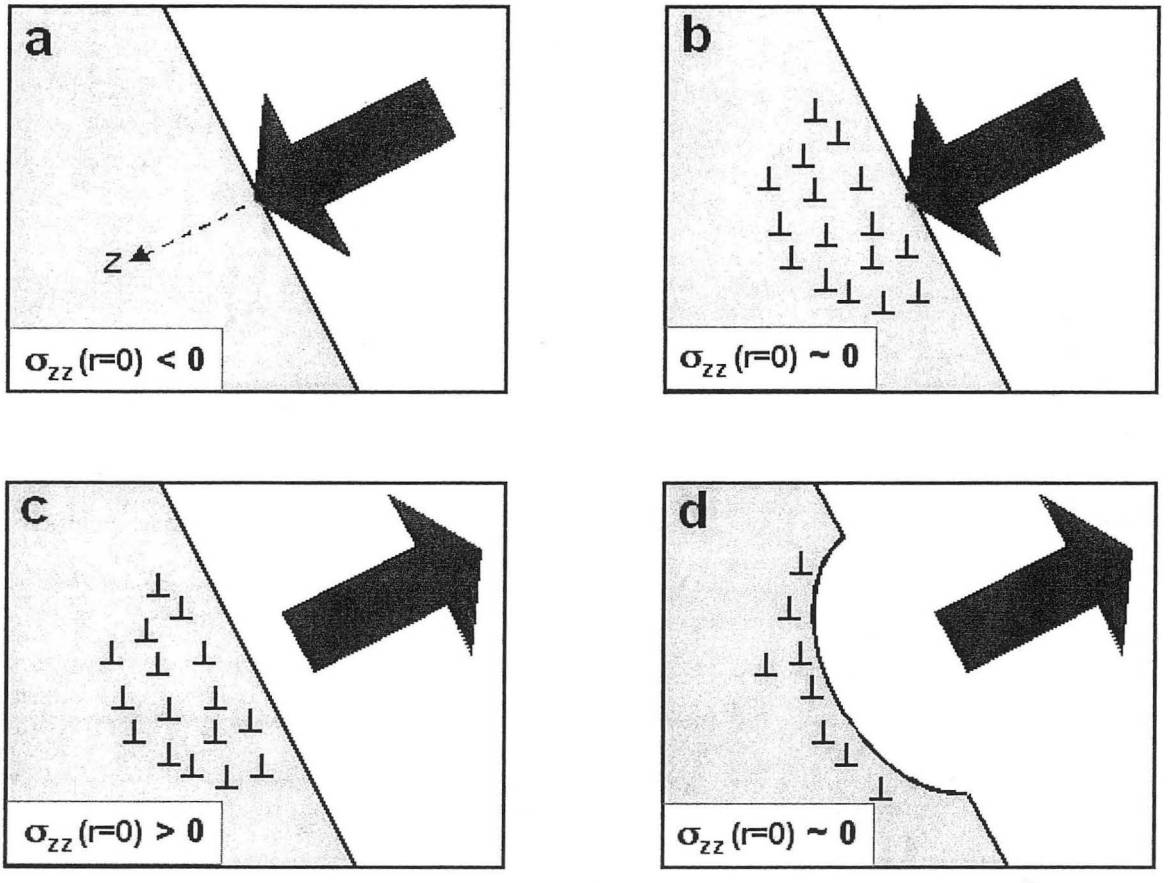

Figure 3.2.5 Schematic of the non-crystallographic fracture event shown in Figure 3.2.4. **(a)** As the indenter applies pressure to an initially defect-free volume of silicon, the stress state directly under the indenter is comprised of both compressive and shear components. **(b)** A portion of the stress is relieved by the nucleation of dislocations, which move plastically to decrease the stress under the indenter. **(c)** When the indenter is withdrawn, the plastically-deformed zone results in a tensile stress due to the expansion of the deformed volume when the pressure of the indenter is relieved. **(d)** The resulting tensile field can cause a fracture event as seen in Figure 3.2.4.

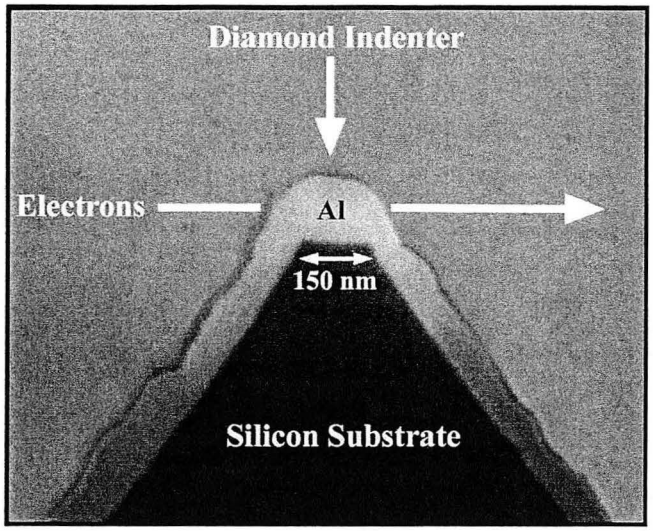

Figure 3.3.1 Cross-section of an *in situ* nanoindentation sample. An Al film ~250 nm thick is deposited onto a wedge-shaped perturbation on a Si substrate

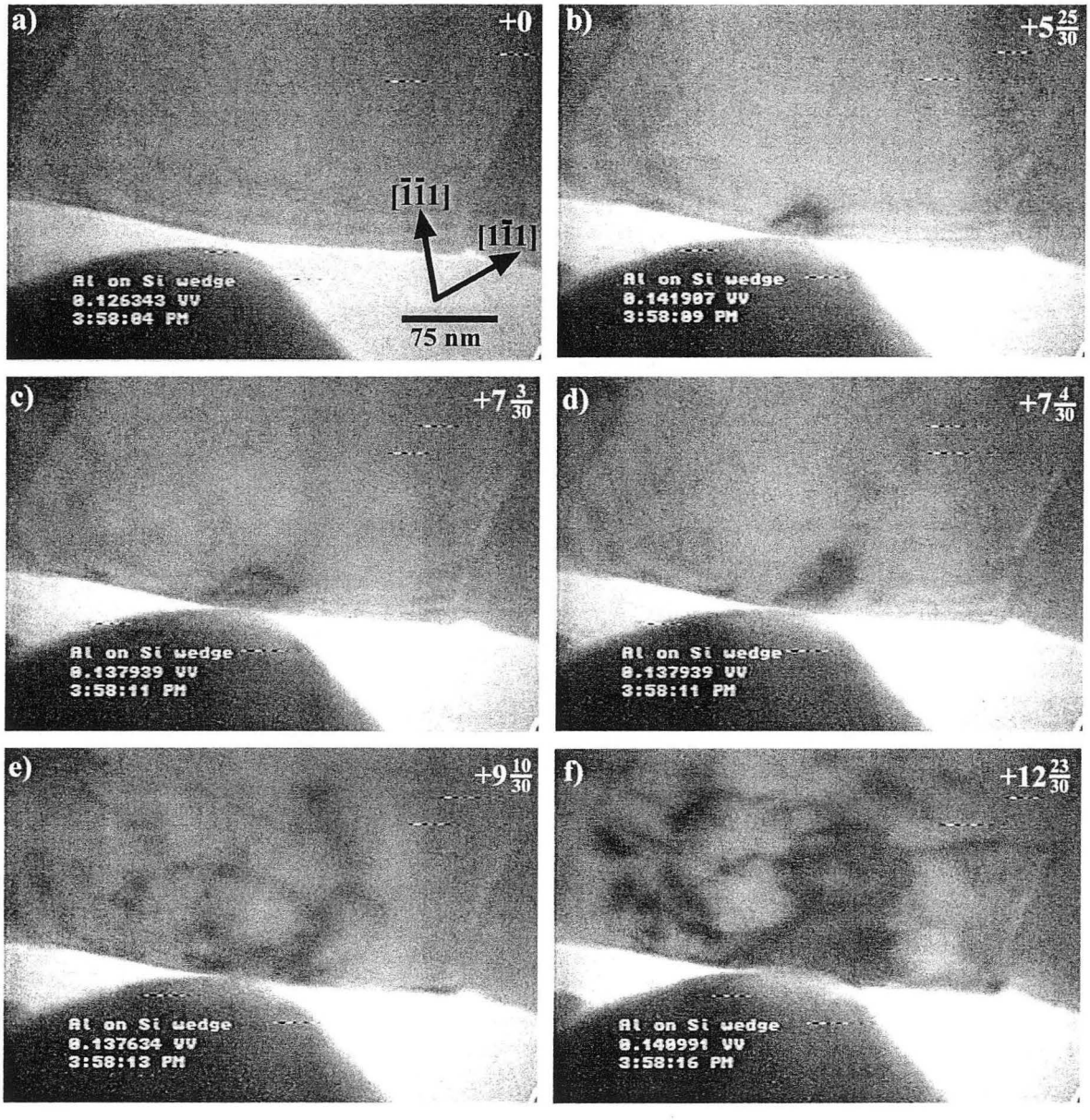

Figure 3.3.2-Time series of an Al grain showing the evolution of plastic deformation during an *in situ* nanoindentation in the [1-11] direction. The time elapsed from image **(a)** is given in seconds in the upper right corner of each frame. Images **(b)** and **(c)** correspond to elastic deformation only. In image **(d)** the nucleation of dislocations can be seen. **(e)** and **(f)** is characteristic of the resulting plastic deformation during deeper penetration and the pile-up of the dislocations at the grain boundaries and the substrate/film interface.

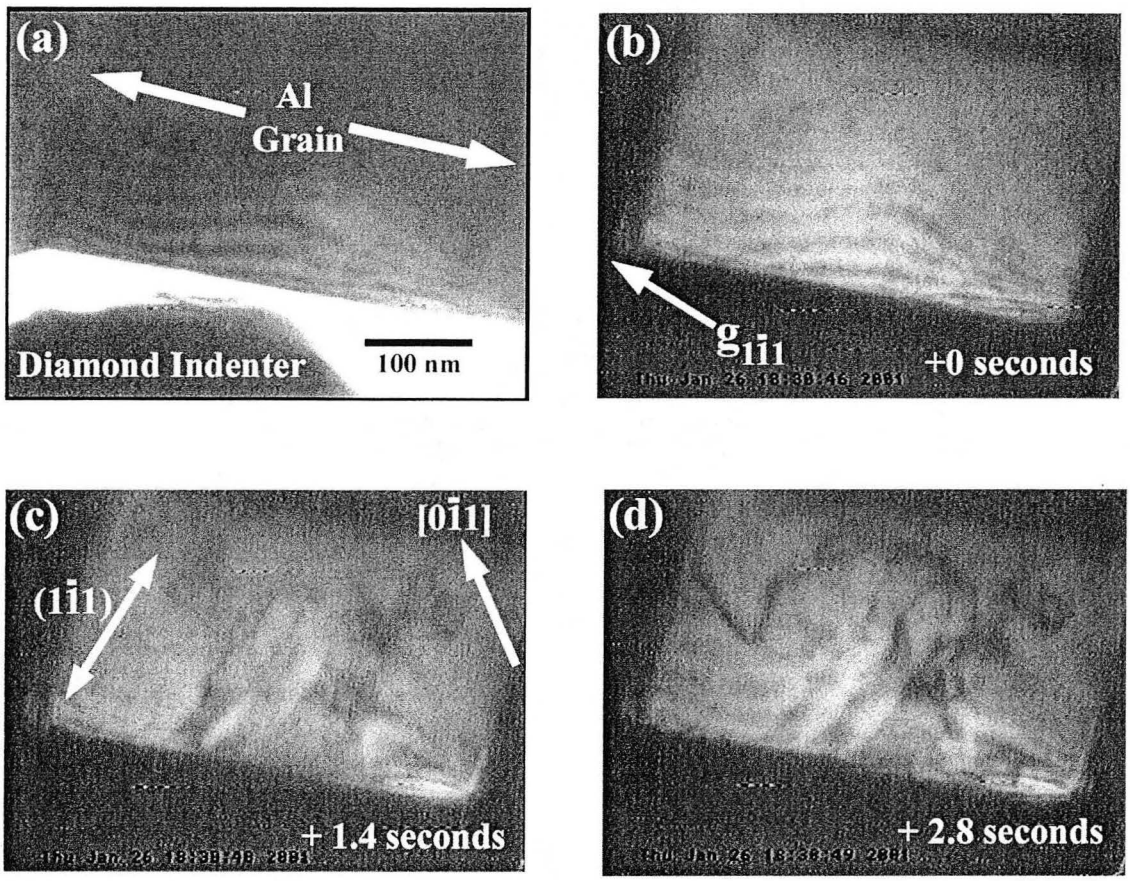

Figure 3.3.3 Time series of an Al grain showing the evolution of plastic deformation during an *in situ* nanoindentation: **(a)** Bright field and **(b)** dark field image before indentation. The dark field condition used was [1-11]. The stripes are thickness contours due to the wedge shape of the specimen. **(c)** Dark field micrograph at t = 1.4 seconds showing dislocations on {111} planes. **(d)** Dark field micrograph at t = 2.8 seconds showing multiple dislocations.

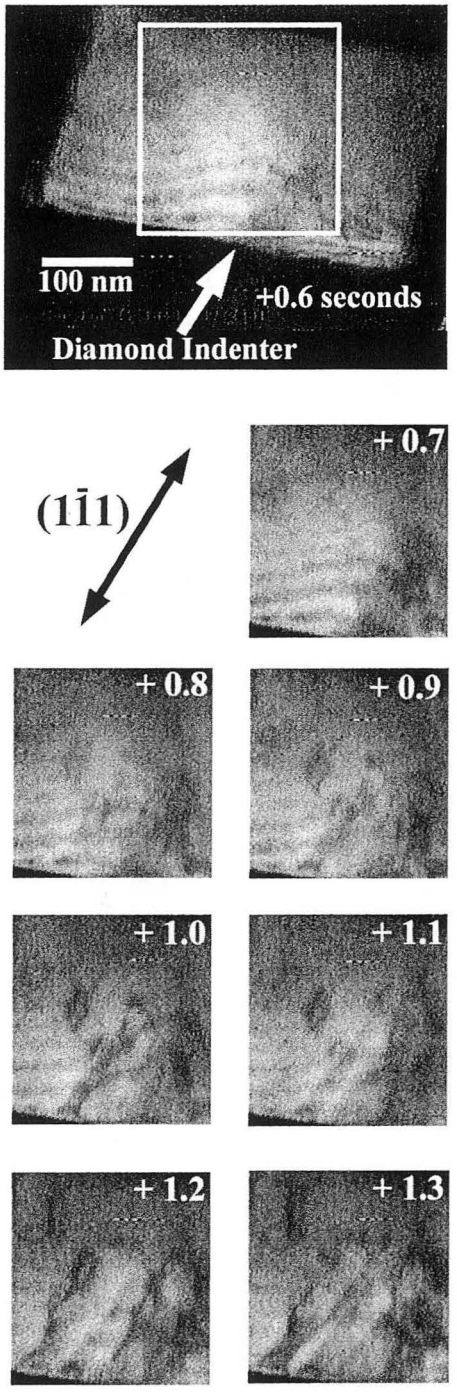

Figure 3.3.4 Series of dark field transmission electron micrographs showing the appearance and evolution of prismatic dislocation loops in a previously undeformed part of the Al grain during an *in situ* nanoindentation. The numbers in the micrographs are the time in seconds from the start of the indentation.

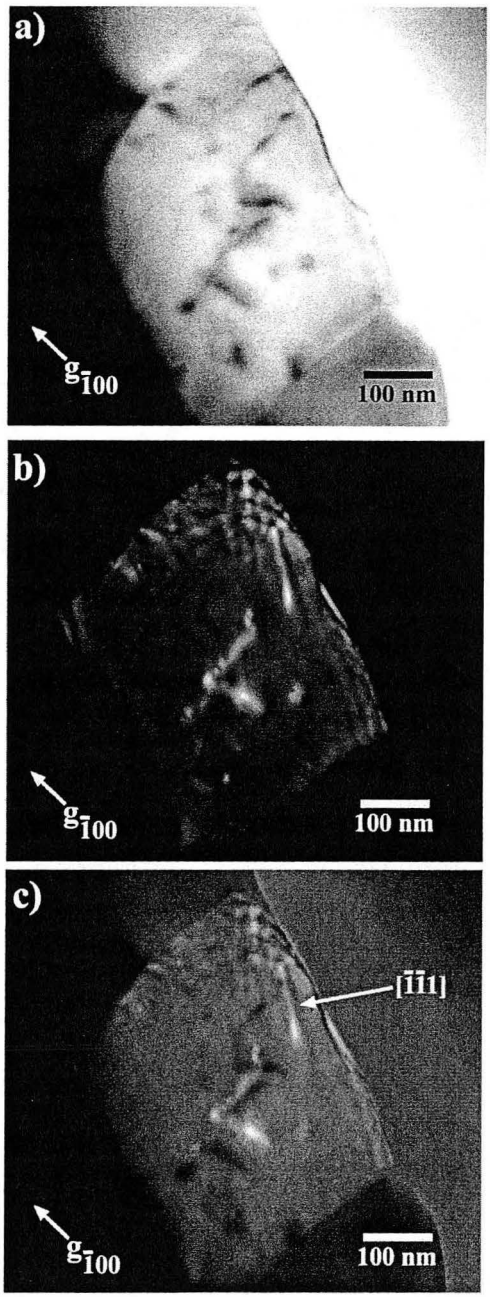

Figure 3.3.5 Post-indent images from the experiment shown in Fig. 3.3.2 using the [-100] diffraction condition. **(a)** Bright field image taken approximately 2-3 minutes after the indentation. **(b)** Dark field image taken approximately 4-6 minutes after the indentation. **(c)** The DF image overlaid on top of the BF image, demonstrating the rearrangement of the dislocations which occurred sometime between the time the BF and DF images were taken.

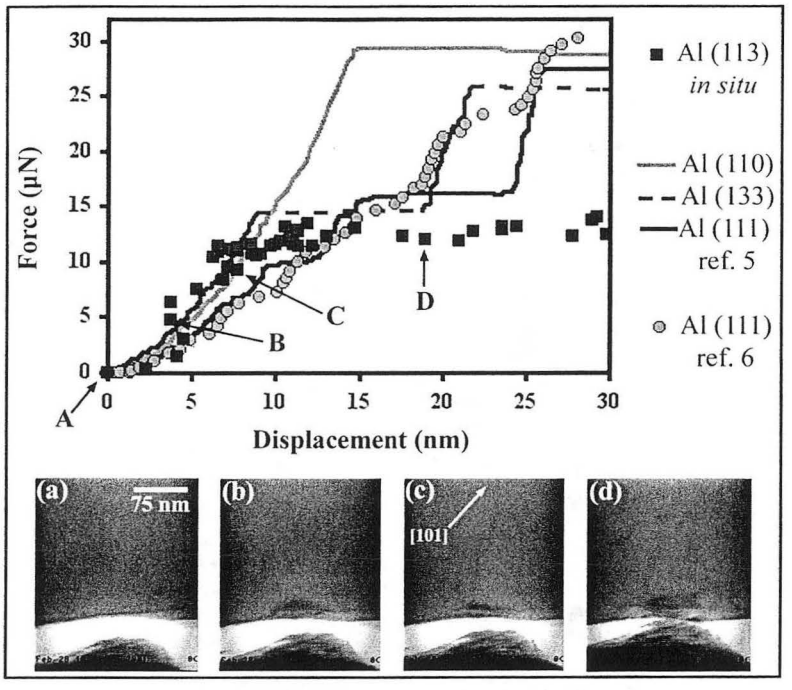

Figure 3.3.6 Force-displacement curve and representative micrographs from an Al grain indented *in situ* in the <113> direction. Nanoindentation data from Gouldstone, *et al.*[5] and Lilleodden[6] are also shown for comparison. Pictures **(a), (b), (c)** and **(d)** correspond to points A, B, C and D on the graph, respectively. Due to contrast effects, the very tip of the diamond indenter is not visible in the micrographs.

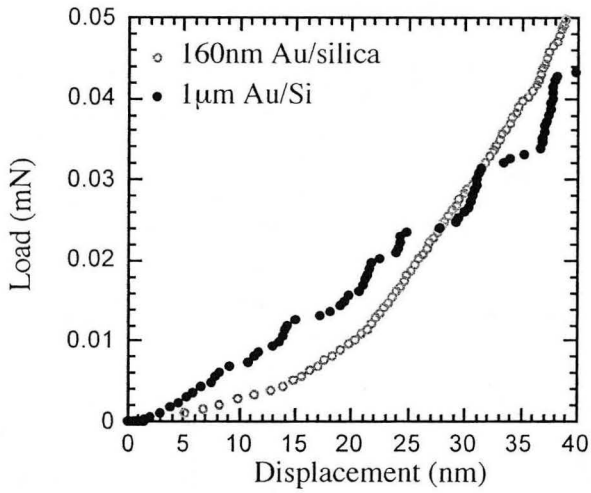

Figure 3.3.7. Results from instrumented indentation experiments into Au thin films of two different nominal grain sizes conducted by Lilleodden & Nix[11,12]. (data courtesy of Erica Lilleodden, Lawrence Berkeley National Laboratory, Berkeley, CA 94720)

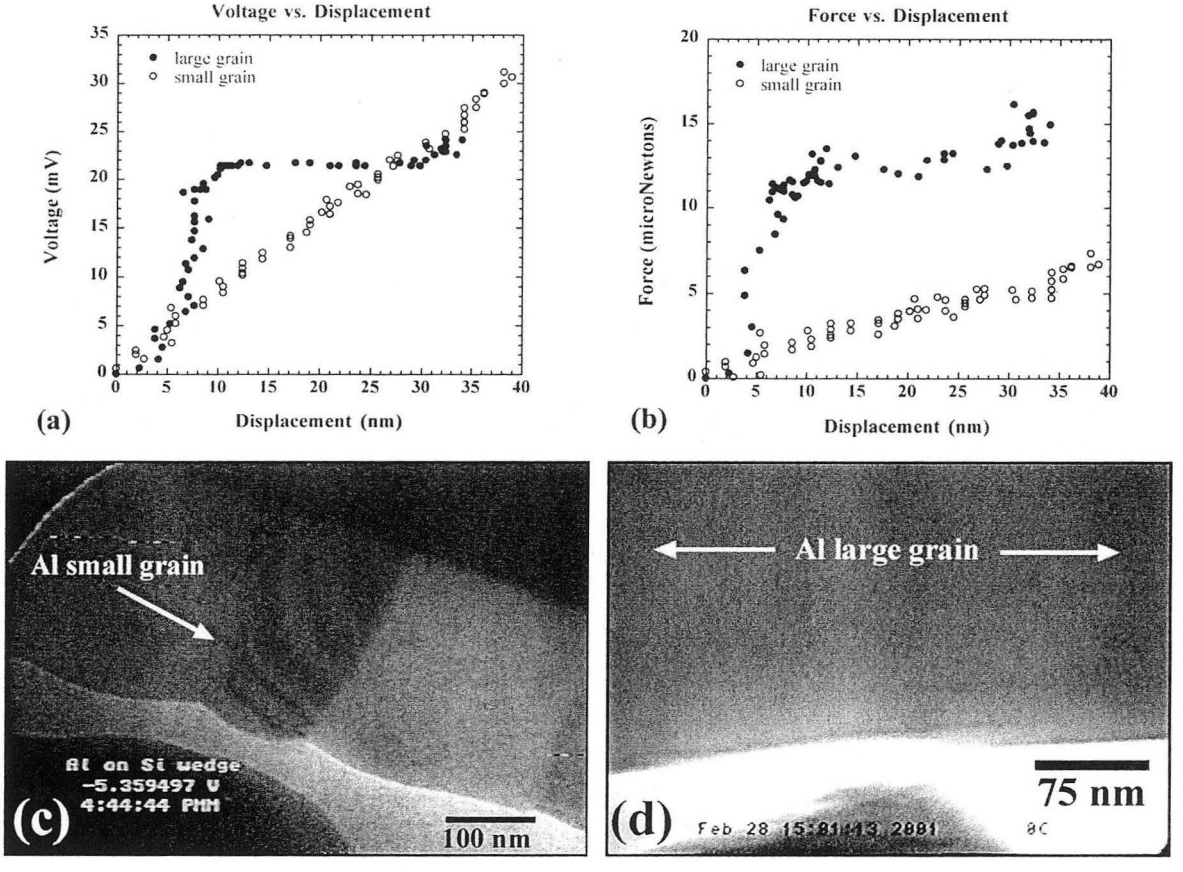

Figure 3.3.8 (a) The voltage-displacement response associated with indentations into two grains of Al with different sizes relative to the indenter. **(b)** The corresponding calibrated load-displacement response for the same two grains. **(c)** and **(d)** are TEM images of the small grain and large grain, respectively, with the diamond indenter approaching the grains before indentation. The grain termed "small grain" had an effective grain size of ~100 nm, about the same size as the indenter radius. The grain termed "large grain" had an effective grain size of ~670 nm, which is large relative to the size of the indenter

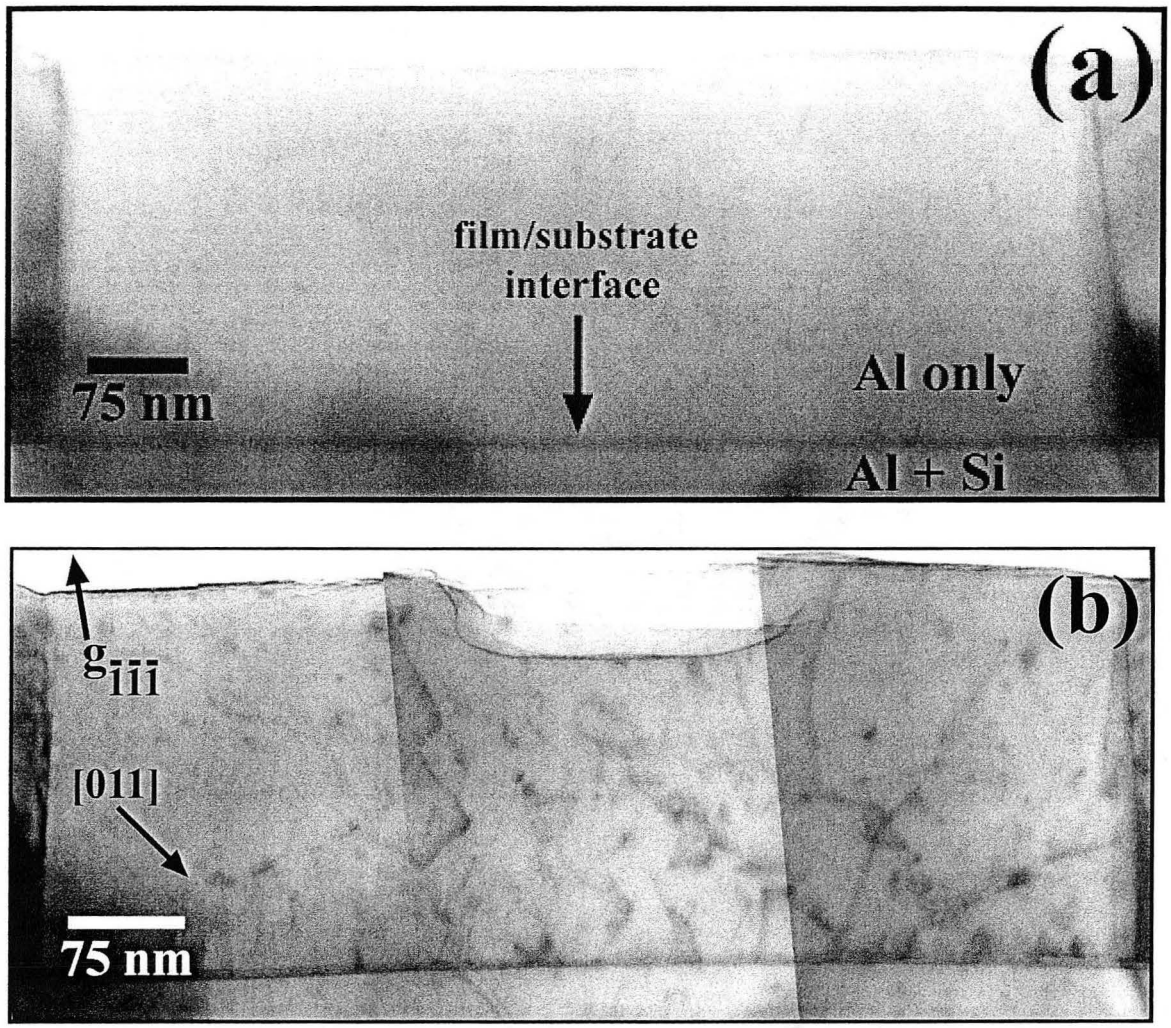

Figure 3.3.9 **(a)** shows the as-deposited condition of an Al grain deposited onto a Si wedge substrate. The interface of the Al grain and Si substrate can be seen at the bottom of the image. **(b)** Shows the same Al grain in the same diffraction condition after indentation (3 images are pasted together here in order to span the entire grain at high magnification). The indentation crater can be seen at the top of the image, as can the numerous dislocations introduced in order to accommodate the induced deformation. Quite noticeably, the dislocations pile up at the film/substrate interface.

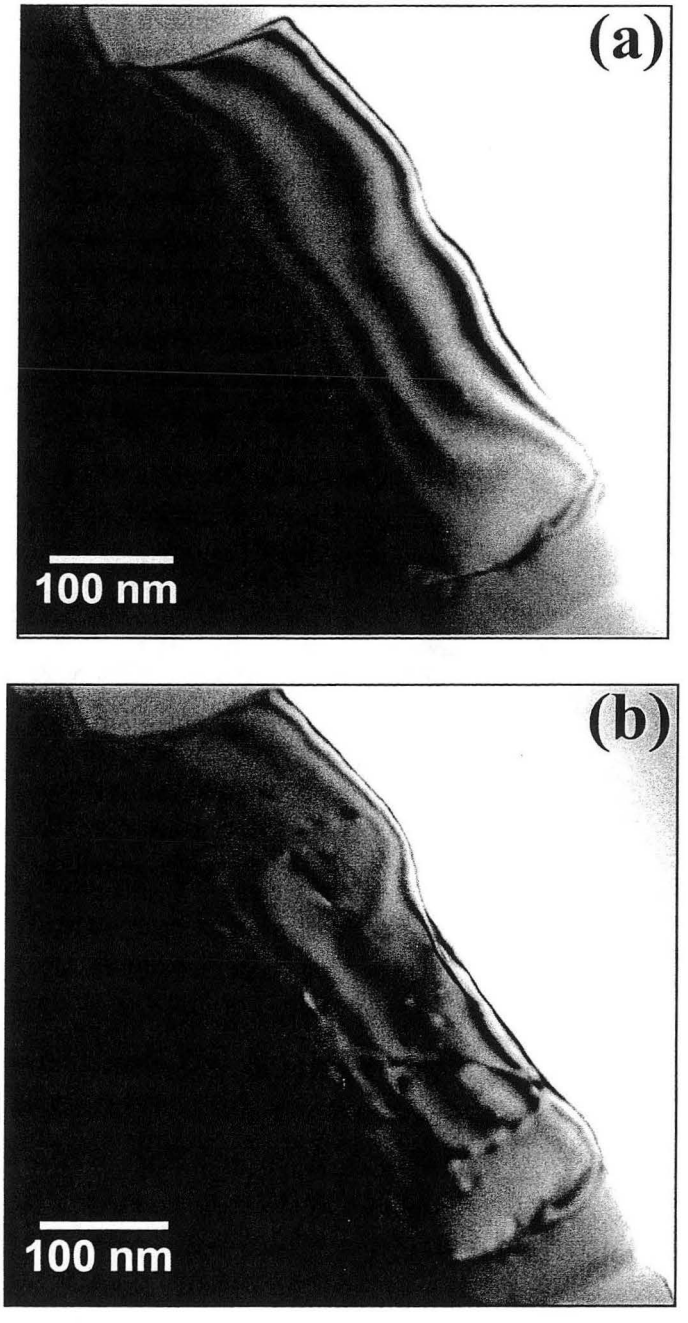

Figure 3.3.10 (a) Bright field TEM image showing the as-deposited condition of an Al grain deposited onto a Si wedge substrate **(b)** Shows the same Al grain in the same diffraction condition after indentation In this case, the dislocations do not extend all the way to the lateral grain boundaries.

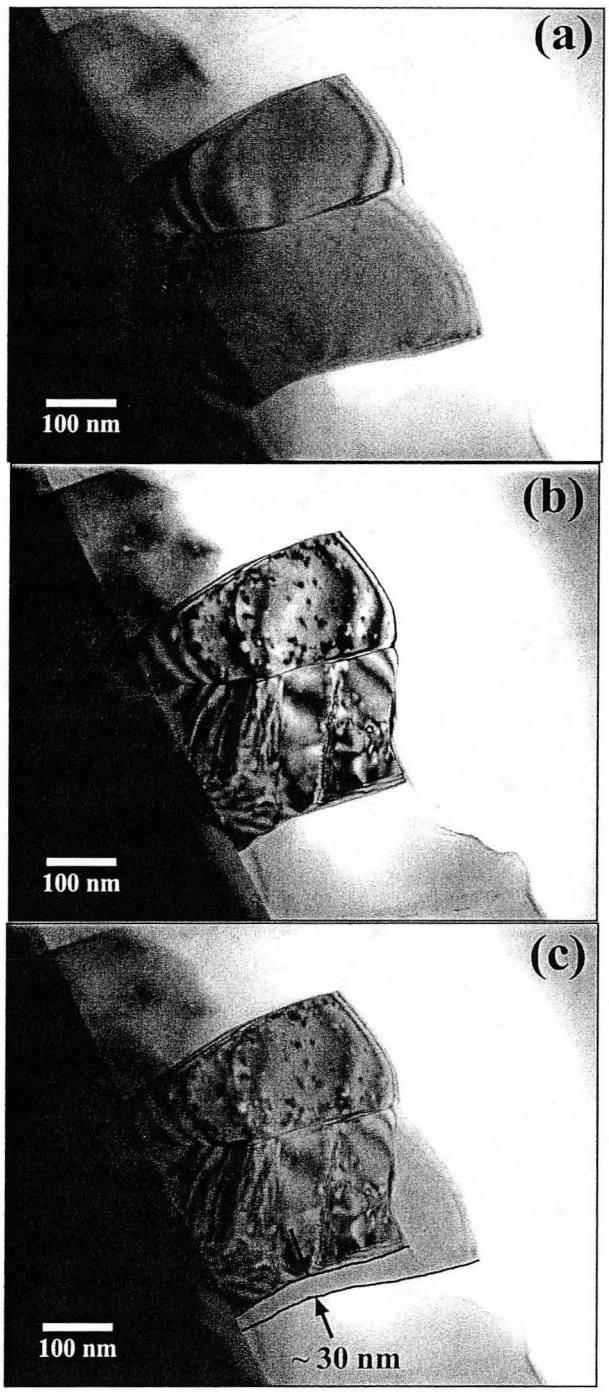

Figure 3.3.11 (a) is a TEM image of two Al grains taken before indentation. **(b)** is a TEM image of the same two grains after indentation in the same diffraction condition.**(c)** The same two images, 3.3.11(a) and (b), overlaid on top of each other, showing that the grain boundary had moved extensively during the indentation.

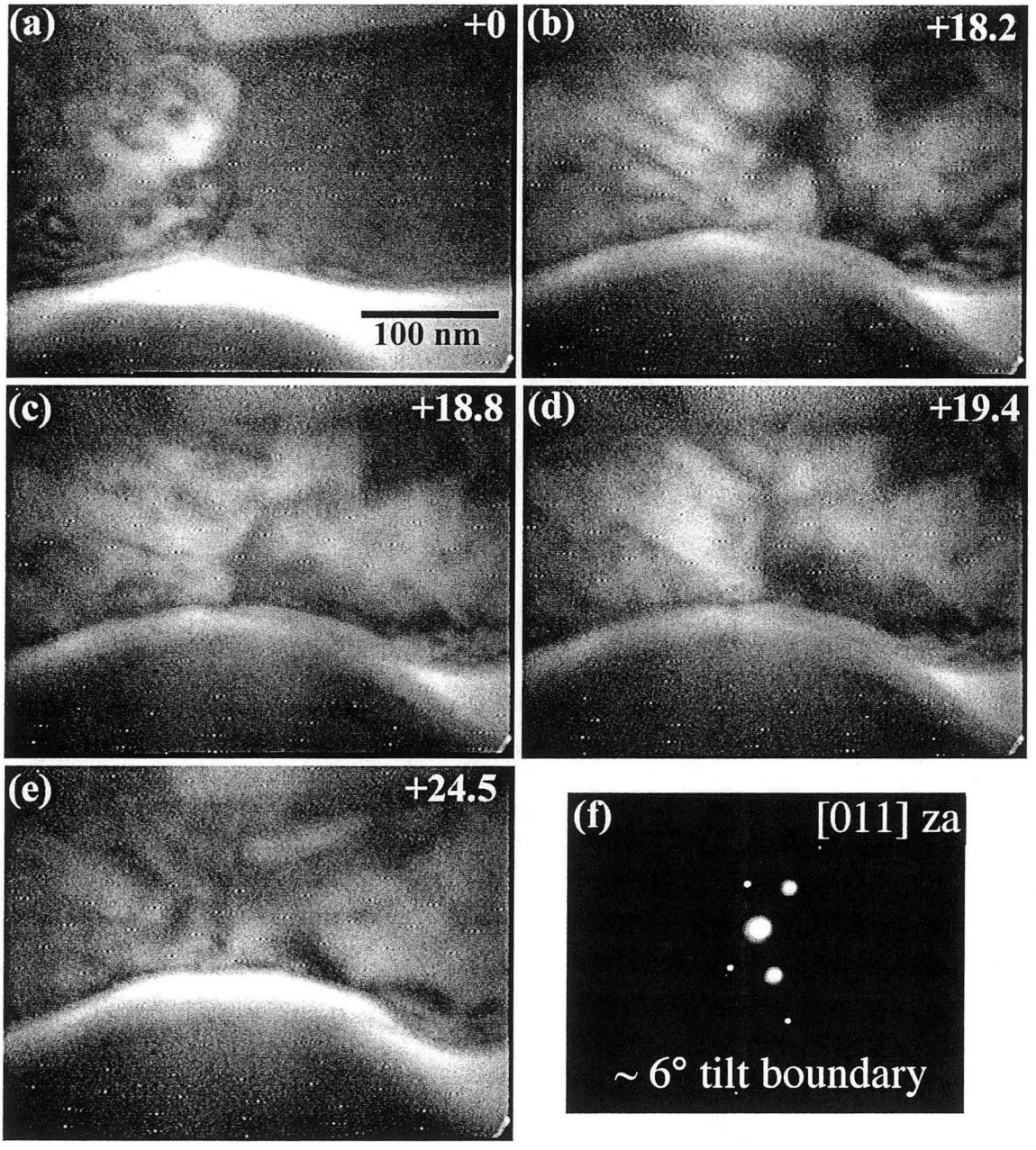

Figure 3.3.12 (a) The Al tilt boundary prior to indentation with the indenter approaching from the bottom of the image. **(b), (c)** and **(d)** are three images only 0.6 seconds apart, taken 18.2 seconds from the start of the indentation. The grain boundary can be seen to change positions dramatically even over this short time frame (1.8 seconds for the three images). Dislocations can also be seen extending from/to the grain boundaries in each grain. Image **(e)** shows is the final position of the grain boundary after the indenter has been removed, which is similar in location to the grain boundary's original position. **(f)** A diffraction pattern of both grains, showing two strongly-diffracting planes, one from each grain.

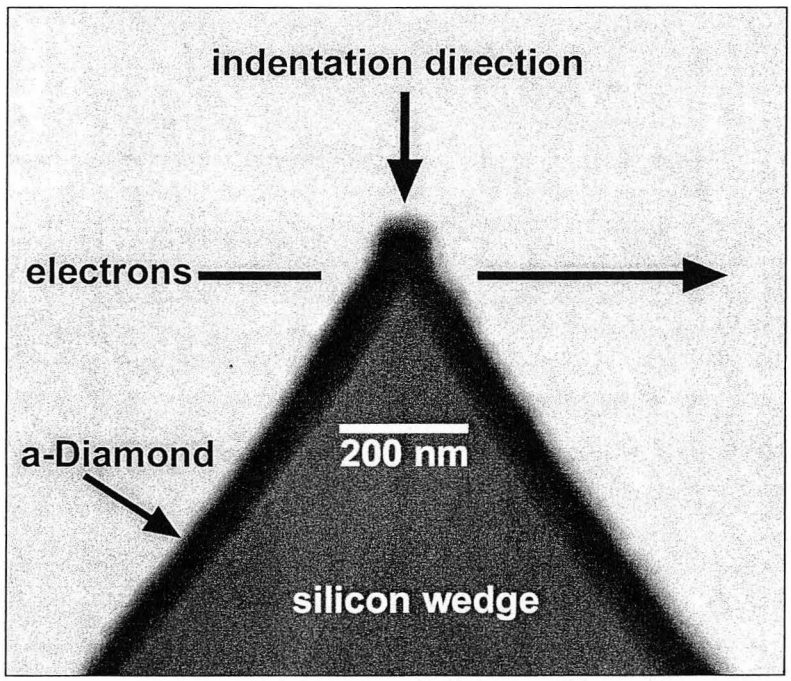

Figure 3.4.1 Scanning electron micrograph of a lithographically-prepared silicon wedge coated with amorphous diamond in cross-section. The sample was prepared with a focused ion beam after being protected with a layer of Pt.

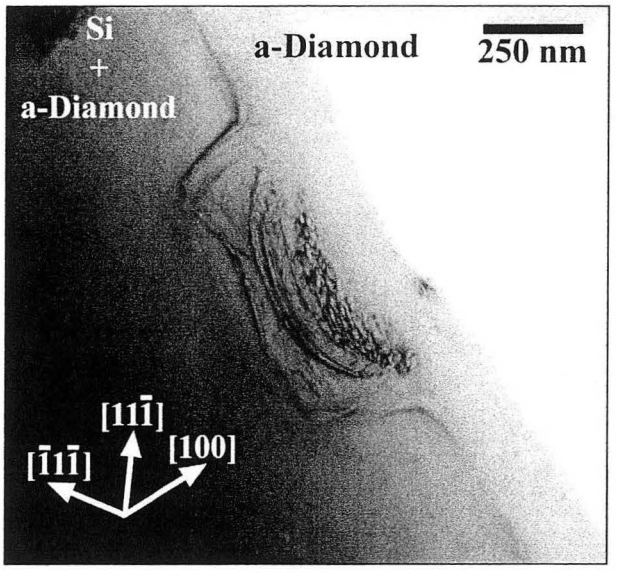

Figure 3.4.2 Bright field TEM micrograph of a post-indentation microstructure from an amorphous diamond on silicon substrate. As can be seen, the silicon sample deformed through dislocation nucleation and propagation, while the a-D thin film showed minimal decrease in thickness even at the point of indentation. The dark spot in the film is a piece of the crystalline diamond indenter that broke off during the indentation.

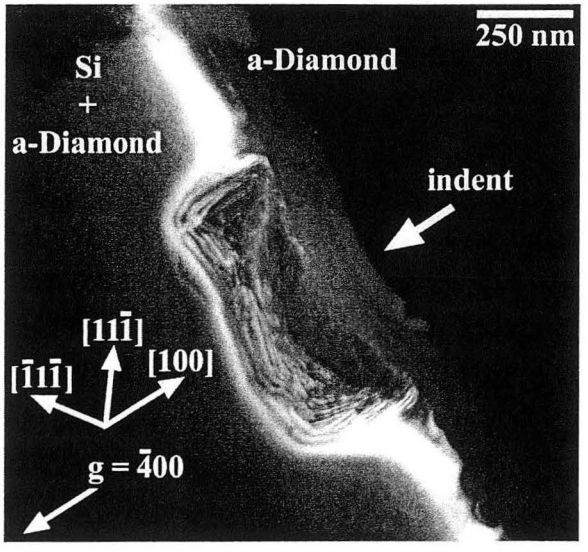

Figure 3.4.3 Dark field TEM micrograph corresponding to figure 3.4.2, taken in the g = (-400) diffraction condition. The strongly diffracting thickness contour shows the interface of the silicon and amorphous diamond. .

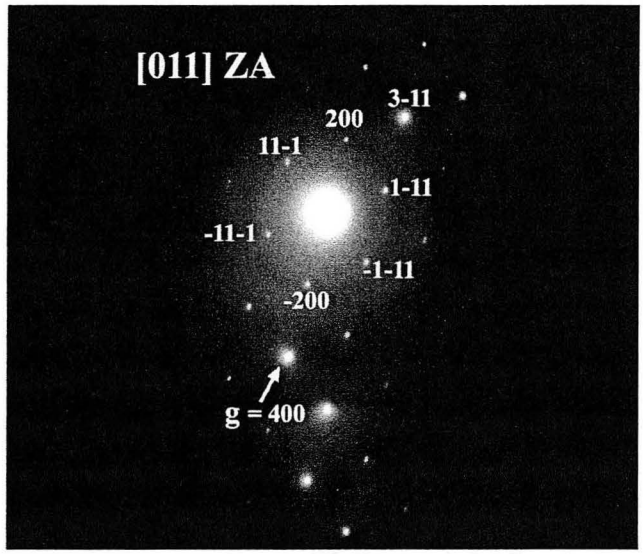

Figure 3.4.4 Selected area diffraction pattern taken directly after indentation into the amorphous diamond on silicon sample. The diffraciton pattern is taken in the [011] Zone axis condition, and is characteristically the same as the diffraction pattern taken prior to indentation. Both the single crystal silicon diffraction spots and the amorphous rings from the diamond film can be seen.

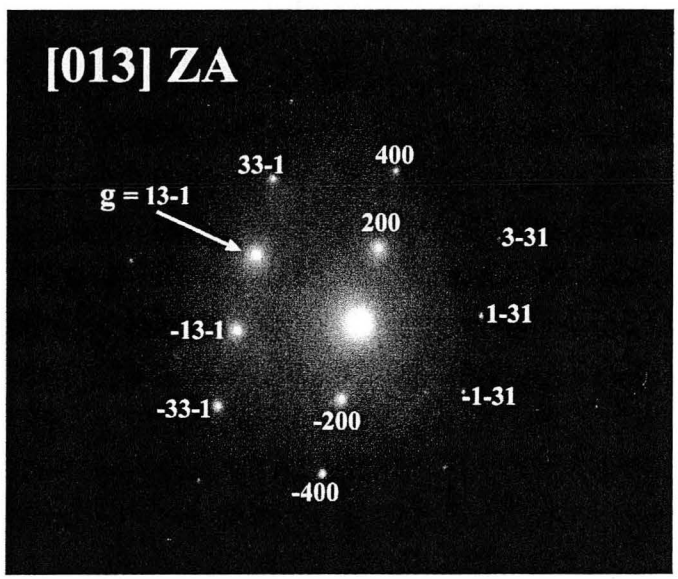

Figrue 3.4.5 Selected area diffraction pattern taken directly after indentation into the amorphous diamond on silicon sample. The diffraciton pattern is taken in the [013] Zone axis condition, and is characteristically the same as the diffraction pattern taken prior to indentation. Both the single crystal silicon diffraction spots and the amorphous rings from the diamond film can be seen.

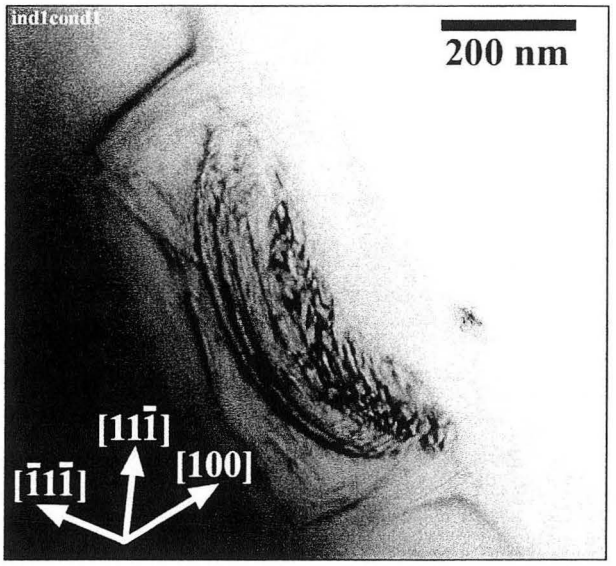

Figure 3.4.6 Bright field TEM micrograph of the amorphous diamond on silicon indent #1. The image was taken in the same g = (-400) diffracting condition as Figure 3.4.7, and the deformation appears highly similar.

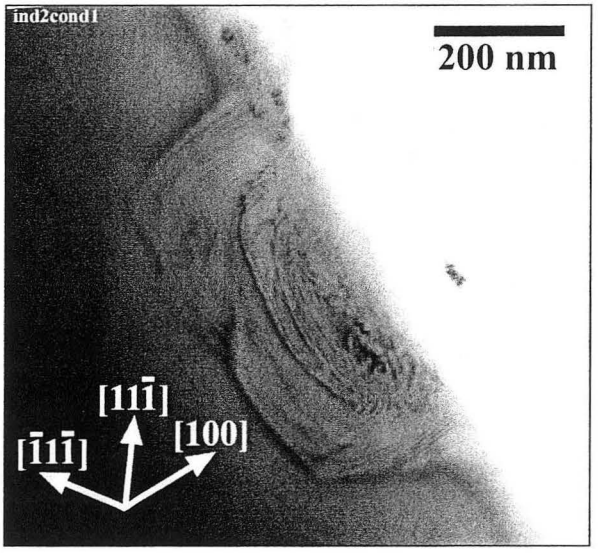

Figure 3.4.7 Bright field TEM micrograph of the amorphous diamond on silicon indent #2. The image was taken in the same g = (-400) diffracting condition as Figure 3.4.6, and the deformation appears highly similar.

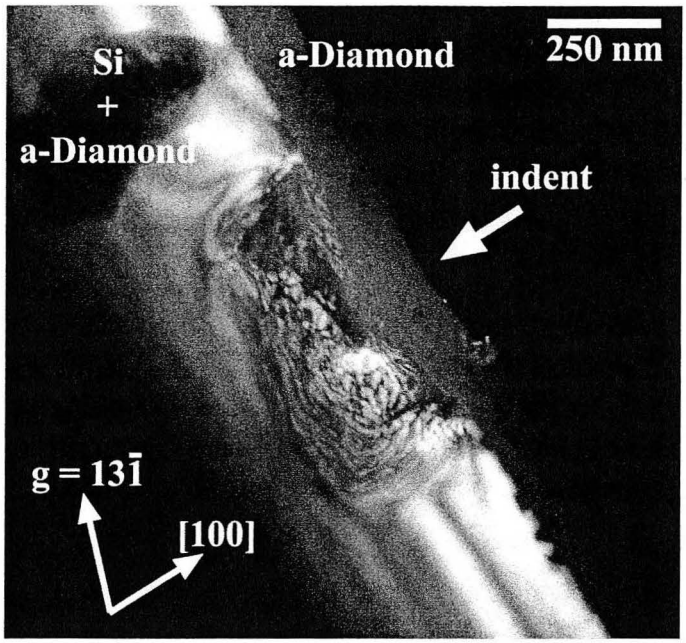

Figure 3.4.8 Dark field TEM micrograph of the amorphous diamond on silicon indent #1. The image was taken in the same g = (13-1) diffracting condition as Figure 3.4.9, and the deformation appears highly similar.

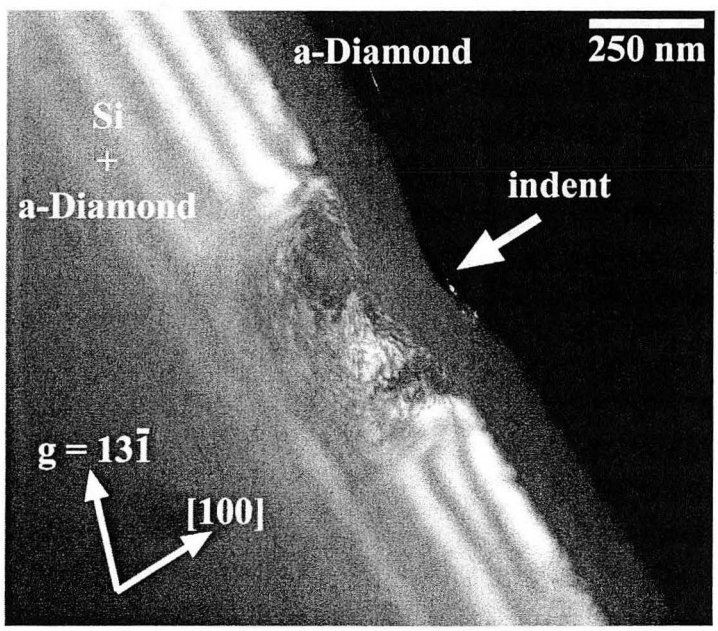

Figure 3.4.9 Dark field TEM micrograph of the amorphous diamond on silicon indent #1. The image was taken in the same g = (13-1) diffracting condition as Figure 3.4.8, and the deformation appears highly similar.

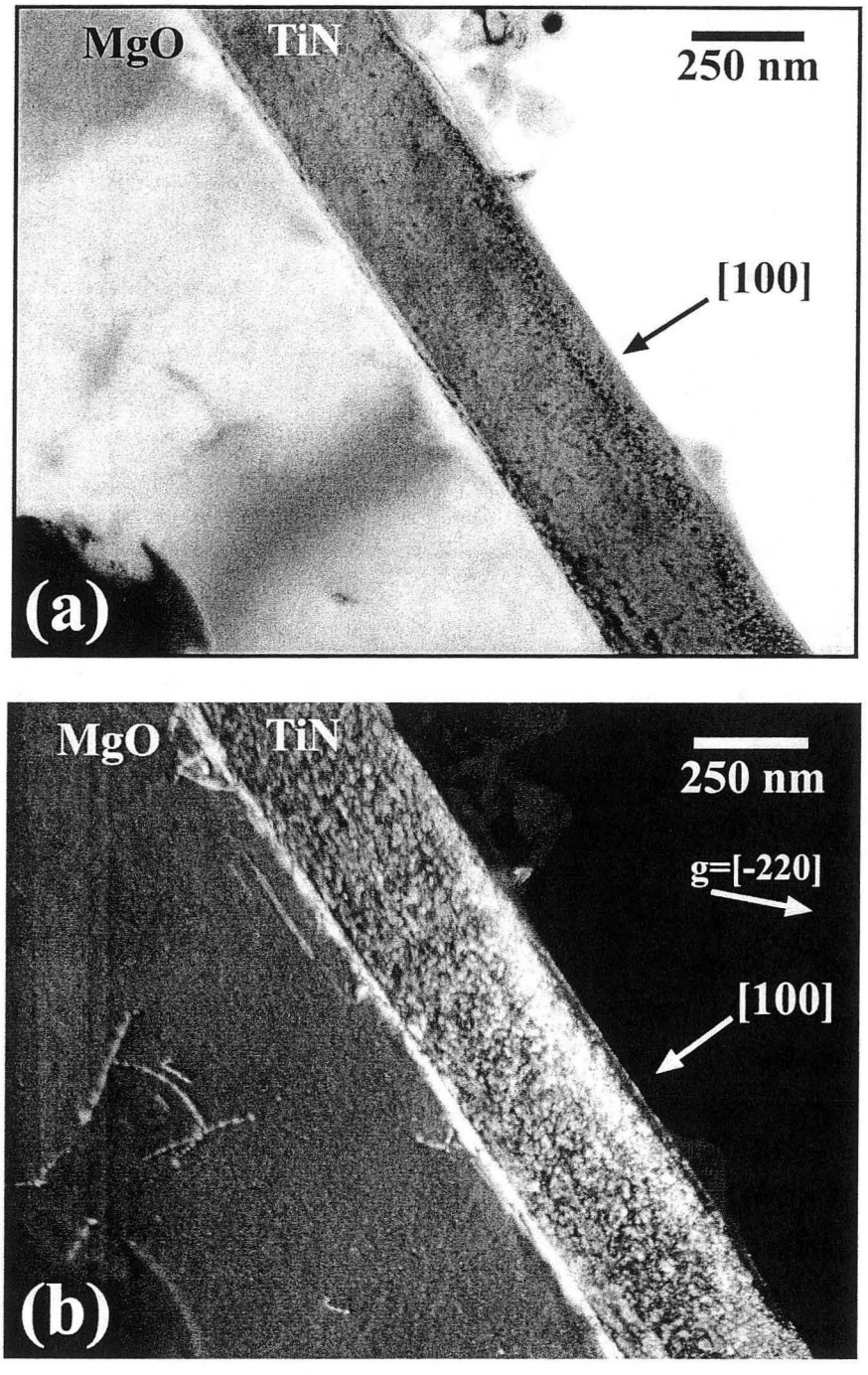

Figure 3.4.10 (a) Bright field and **(b)** dark field TEM mirographs of the epitaxial TiN/MgO (100) sample prior to indentation. Both images are taken in the g = (-220) condition. The arrows showing the [100] direction in both images also point to the location of the indentation shown in figure 3.4.11.

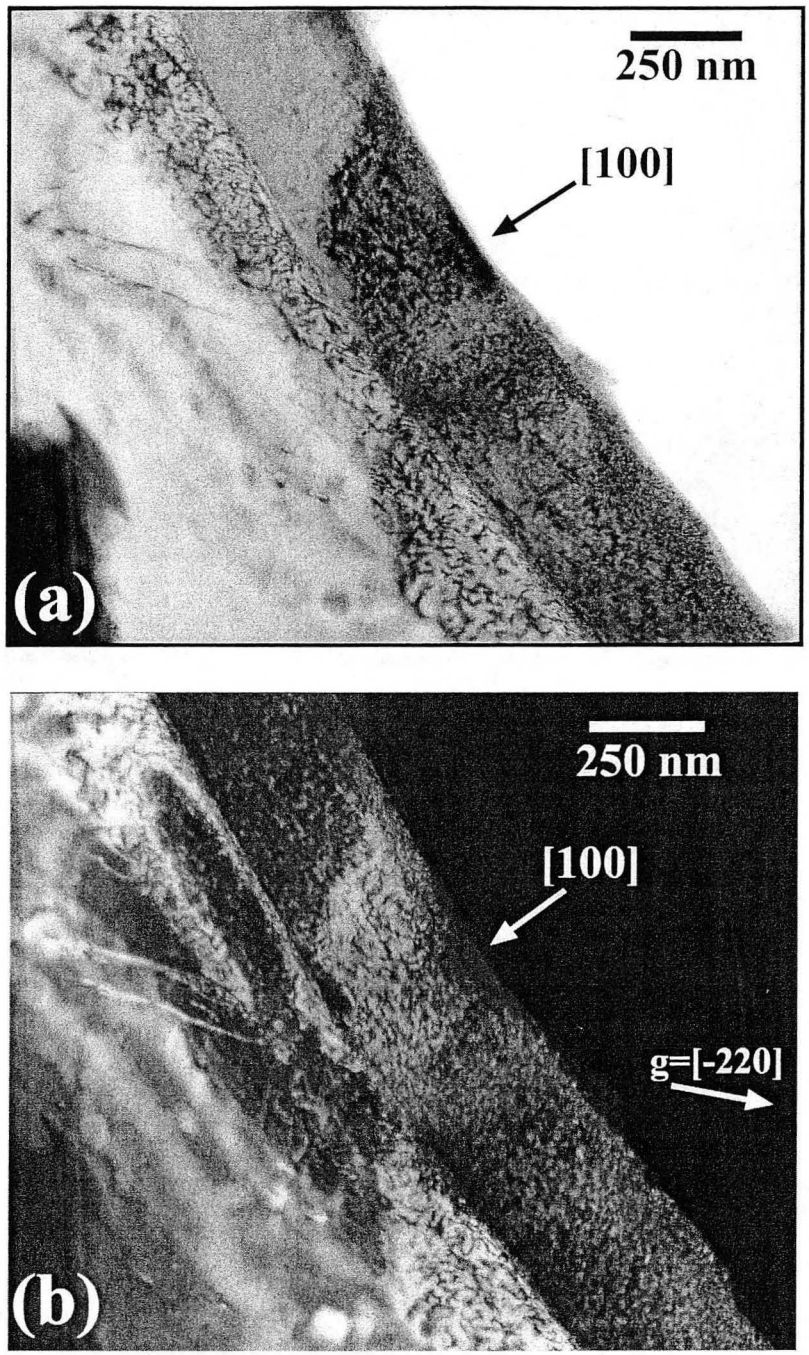

Figure 3.4.11 (a) Bright field and **(b)** dark field TEM mirographs of the epitaxial TiN/MgO (100) sample taken after indentation. Both images are taken in the same g = (-220) condition as figure 3.4.10. The arrows showing the [100] direction in both images also point to the location of the indentation. The diffuse nature of the dislocation plasticity can be seen in the MgO substrate, while the hemispherical configuration of dislocations around the indentation can be seen in the TiN film.

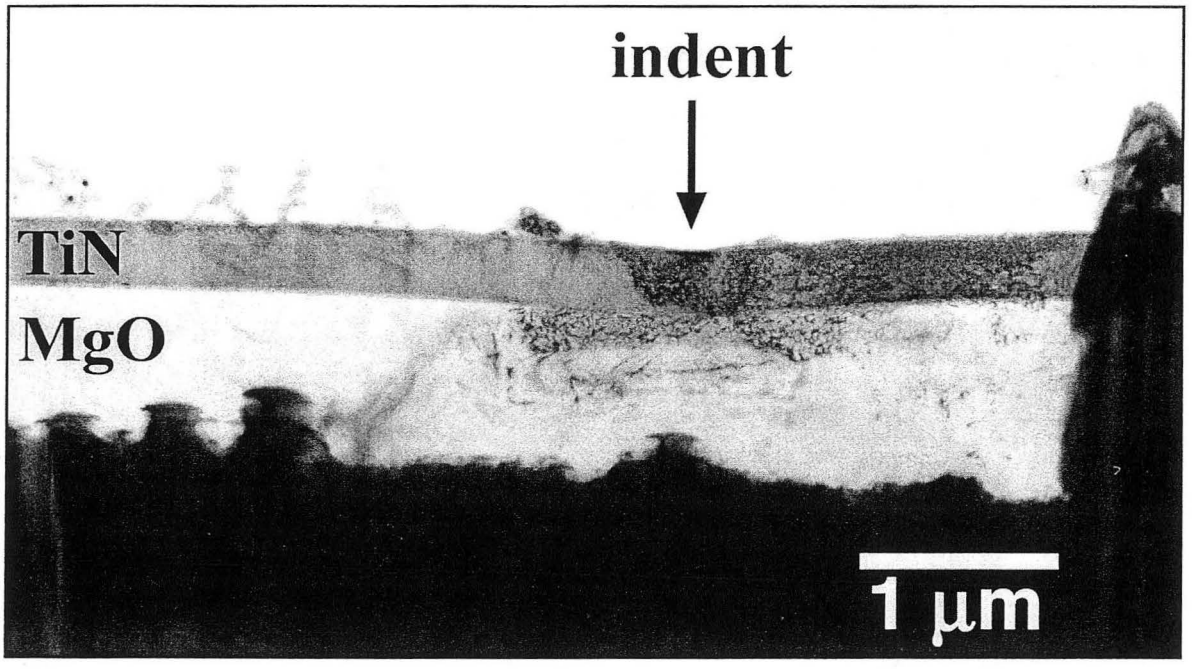

Figure 3.4.12 Lower magnification image of the same indentation shown in figure 3.4.11. The bending of the TiN film can be seen more clearly with reference to the film position farther away from the indentation. Notice the dislocations eminating from the indentation axis in the MgO.

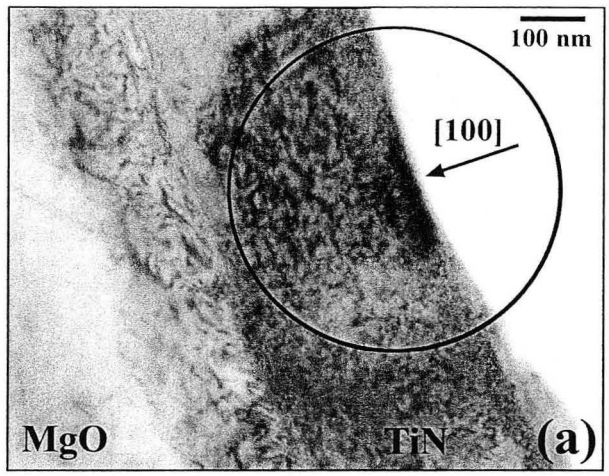

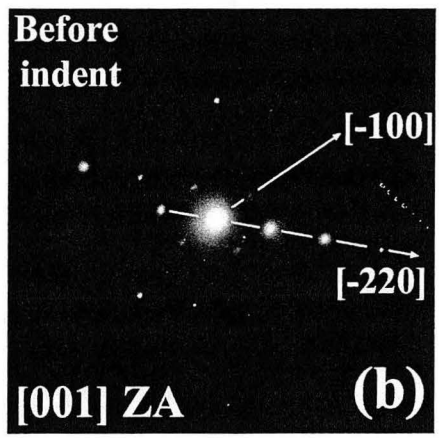

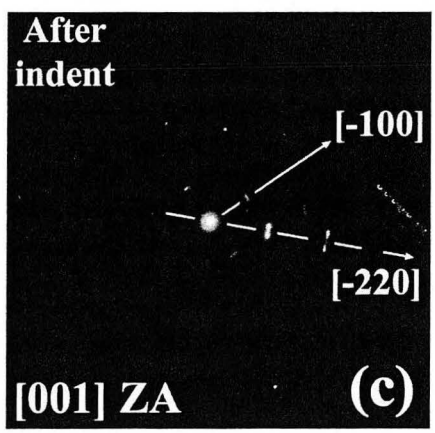

Figure 3.4.13 (a) The post-indent hemispherical plastic zone in the TiN film. **(b)** Selected area diffraction pattern of the TiN film before the indentation. **(c)** Selected area diffraction pattern from the plastic zone of the indentation. The circle drawn over the image in (a) corresponds to the region from which the diffraction information is taken. In (c) the splitting of the [-220] diffraction spots can be seen, indicating the bending of the TiN film 4° to each side.

Ernest Orlando Lawrence Berkeley National Laboratory
One Cyclotron Road | Berkeley, California 94720

Prepared for the U.S. Department of Energy under Contract No. DE-AC03-76SF00098